POLITECNICO DI TORINO

Department of Mechanical and Aerospace Engineering

Master's Degree in Automotive Engineering Class LM-33 (DM270)

Design and Validation of a Full Vehicle Model for a Formula SAE Race Car

Supervisors

Prof. Andrea TONOLI

Eng. Stefano FAVELLI

Candidate

Lorenzo Maria CRAVERO

JULY 2025

Abstract

The goal of this master's thesis is to develop a comprehensive simulation tool for a Formula Student vehicle, aimed at both modeling and validation, with the purpose of enhancing overall performance and accurately estimating powertrain behavior, cooling efficiency, and energy management. Thus, a secondary objective of the thesis is to create a modular simulation framework capable of linking all key subsystems, enabling cross-validation within a single platform. The final outcome includes lap-time estimation as well as electrical and thermal performance accurate simulation.

To facilitate this multi-domain integration, the vehicle model is developed using Simscape, a relatively recent MATLAB & Simulink library that allows coupling of mechanical, electrical, and thermal components. This environment provides the flexibility required to connect and test all relevant subsystems maintaining a coherent workflow. Furthermore, it allows for a wide range of simulations, from open-loop to closed-loop configurations, with the capability to include or exclude individual subsystems as needed, enabling the investigation of causal relationships behind various phenomena.

The process begins with the fundamentals of tire modeling and vehicle dynamics, which are the first to be validated in order to ensure a solid foundation. Once the virtual vehicle demonstrates sufficient correlation with real-world behavior, the focus shifts to the other subsystems. The thesis then explores electric powertrain modeling, including basic electrical machine principles, thermal generation, and heat exchange. Particular attention is given to electrical and thermal management systems, which are carefully modeled and validated.

Special focus is placed on the powertrain subsystem, representing the first iteration of a simulation architecture with significant potential for future development and refinement.

Finally, performance evaluation and subsystem validation are conducted through dedicated MATLAB scripts, which compare simulation outputs with real-world data from track testing and race events. The results are critically assessed to highlight consistency with experimental observations and to identify any discrepancies. In an endurance scenario, the simulation demonstrates an energy consumption error

of approximately 5%, and a deviation in motor temperature prediction of less than 10% compared to actual measurements. These results enable the development of lap-time strategies based on accurate energy usage and thermal behavior.

Table of Contents

List of Tables

List of Figures

Chapter 1

Background

1.1 Formula SAE

1.1.1 The competition

Formula SAE (FSAE) or Formula Student is a university engineering competition organized by SAE International (Society of Automotive Engineers). It challenges students to design, build, and test a formula-style race car, providing hands-on experience in both engineering and project management skills. The cars then compete on real circuits all around the world.

The competition mirrors real-world automotive engineering scenarios, requiring teams to function like professional racing or development groups. Beyond building a high-performance vehicle, participants must also demonstrate the car's design logic and business feasibility through rigorous evaluations by industry experts.

Formula Student originated in the United States in 1981 and expanded to Europe in the early 2000s. Among all the events, Formula Student Germany (FSG) is considered the most prestigious, serving as a benchmark for other competitions; in 2024, Formula Student Germany became a fully electric competition, and combustion vehicles were no longer accepted. Other key events in Europe include Formula SAE Italy, Formula Student Spain, Formula Student Austria, and Formula Student East, among others.

Today, over 400 university teams from more than 60 countries participate in Formula Student, competing in three main categories: Combustion, Electric, and Driverless Vehicles. According to competition regulations, all vehicles must be designed, developed and maintained entirely by students, without direct involvement of professional engineers, racers, or machinists. The rules usually allow significant freedom regarding performance, but they are quite stringent in terms of safety. They are becoming increasingly complex each year, challenging students and preparing them for motorsport regulations. Each event is subdivided into static and dynamic

Figure 1.1: Teams at Formula Student Austria 2024.

events. The maximum number of available points is 1000, 325 are assigned to static events and 675 to the dynamic events.

1.1.2 Static events

The static events are 3:

* **Engineering Design**
  This event assesses the technical aspects of a team's race car and knowledge of the team members, focusing on design choices, engineering reasoning, and practical application. Judges evaluate key areas such as aerodynamics, chassis, suspension, and powertrain. Teams must justify their decisions, compare alternatives, and demonstrate improvements based on testing and data. The event highlights problem-solving skills and technical communication. Up to 150 points can be assigned in this event.

* **Cost and Manufacturing**
  It is the most diverse event, evaluates a team's ability to design a race car while considering production feasibility and cost efficiency. Teams submit a detailed cost report, breaking down materials, labor, and manufacturing processes. Judges take into consideration cost-effectiveness, design for manufacturability, and budget decisions. Additionally, teams must defend their choices and handle a real-world cost challenge. Up to 100 points can be assigned in this event.

* **Business Plan Presentation**
  The Business Plan Presentation challenges teams to present a realistic business

strategy for their race car. They must show their concept to judges acting as potential investors, focusing on market potential, cost analysis, and revenue opportunities. The goal is to demonstrate a clear understanding of the financial and commercial aspects of their project. Judges evaluate the feasibility, innovation, and professionalism of the presentation, simulating real-world industry scenarios. Up to 75 points can be assigned in this event.

1.1.3 Dynamic events

The dynamic events are 4:

* **Acceleration**
  The Acceleration Event tests how quickly a car can cover a 75-meter straight track from a standing start. A strong result depends on effective power delivery through traction control, car weight and distribution, and tire grip, making this a key test of a car's longitudinal dynamics performance. The fastest car will obtain 75 points.

* **Skidpad**
  The Skidpad Event measures a car's cornering ability by having it navigate a figure-eight track as quickly as possible. The vehicle has to perform two 18.50 meters diameter circles, and the registered time will be the average between the left and right hand circles. The test evaluates lateral grip, suspension tuning, weight distribution, aerodynamics and torque vectoring. A well-balanced setup with optimal tire performance is crucial for a strong result. The fastest car will obtain 75 points.

* **Autocross**
  The Autocross Event tests a car's handling, acceleration, and braking on a tight, technical course filled with corners, slaloms, and straights. It is the equivalent of a qualify in the other motorsport categories. Teams aim to set the fastest lap time without hitting cones or going off track. The event highlights suspension setup, driver skill, and overall vehicle dynamics. The fastest car will obtain 100 points.

* **Endurance and Efficiency**
  The Endurance ans Efficiency Event is the longest and most challenging dynamic event, testing a car's reliability, efficiency, and overall performance over a 22-kilometer track. Cars must complete the distance without mechanical failures while maintaining competitive lap times. This event is particularly critical for electric race cars, where energy and temperature management also play a crucial role. Driver changes are required halfway through, adding an element of strategy and difficulty. Success depends on fuel or energy efficiency,

cooling, durability, and consistent handling under race conditions. With regard to the endurance event, 325 points are assigned to the fastest car, while in the efficiency event, 100 points go to the car that, within a certain gap to the leader, consumes the least amount of energy.

Figure 1.2: SC24 during FSG Endurance under the storm.

1.2 SC24

1.2.1 *Andromeda*

"Andromeda" or SC24 is the prototype that Squadra Corse PoliTO developed for the 2024 race season, it is the 11^{th} full-electric formula car made by the team.

The car is composed by a Carbon Fiber Reinforced Plastic (CFRP) and aluminium honeycomb monocoque and it is equipped with a fully adjustable double wishbone push-rod suspension system with inboard coil-over dampers and anti-roll bars (ARB). Very high downforce level is reached thanks to various CFRP aerodynamic devices with CdA = 1.45 and ClA = 4.75 approximately.

The electric powertrain is composed by a 574V, 7.72kWh battery pack, made out of 132 series and 2 parallels Li-Po cells, a standard AMK Formula Student

racing kit consisting of 4 IGBT inverters, each one supplying an interior permanent magnet electric motor in outboard configuration. Each motor has a maximum power of 35kW, a maximum torque of 21Nm, and a maximum rotational speed of 20000rpm, so the whole powertrain can produce 140kW, but the output power of the HV battery pack is limited to 80kW by the Formula Student rules [1]. Each motor is coupled with a double stage planetary gearbox with a final ratio of 14.69:1, and at the end of the chain, the vehicle is equipped with 4 Pirelli race slick tires.

The vehicle's onboard communications operate through 4 Controller Area Networks (CAN), which are managed by the Vehicle Control System using a dSpace MicroAutobox II Electronic Control Unit.

Figure 1.3: SC24 "low drag" configuration during FSAE Italy Acceleration.

1.2.2 The 2024 racing season

The 2024 season marks the return of *Squadra Corse* to competition after two years of absence. A completely new team led the car across Europe, taking part in three international events.

The first race wasn't a brilliant start. After nine years, the team returned to Formula Student Austria (FSA) at the *Red Bull Ring*, but SC24 was unable to

participate in the dynamic events due to a technical failure. Nonetheless, the team gained valuable experience during technical inspections and static events, experience that would prove useful just three weeks later at FSG.

The 2024 edition of FSG was the largest electric Formula Student competition ever held, with 84 teams from around the world. Despite a tough classification, it was a real success for *La Squadra*. After 13 years away from dynamic events at FSG, SC24 delivered an impressive performance: 18^{th} place in acceleration and 21^{st} in skidpad, the team's best results.

Unfortunately, the car was not able to complete the endurance event, the most ambitious goal, due to a technical issue that occurred during it. Still, SC24 ran 11 km under heavy rain conditions, during a session where no other team at FSG was forced to compete.

Finally, in a highly competitive edition of FSAE Italy, SC achieved solid results in all dynamic events. Once again racing in the rain, and learning from past mistakes, *Andromeda* was able to complete the endurance event, five years after the team's last successful attempt. It marked a meaningful comeback, bringing *Squadra Corse* back to where it truly belongs.

Chapter 2

Theoretical Framework

This chapter provides the foundational theory necessary to support the development of a complete vehicle simulation model. Given the multi-domain nature of the system, the framework integrates core concepts from tire dynamics, vehicle dynamics, heat transfer, and electric machine modeling. Each section offers the physical principles and mathematical formulations required to accurately model real-world behavior, providing the basis for building and validating the simulation model in the following chapters. A solid theoretical understanding of these topics ensures that the simulation architecture remains robust, reliable, and representative of the physical systems it aims to replicate.

2.1 Tires

Tires represent the only interface between the vehicle and the road, playing a crucial role in all aspects of vehicle dynamics. Their ability to generate and transmit forces directly influences acceleration, braking, and cornering performance. Unlike rigid components, tires are highly nonlinear systems: their behavior depends not only on the material properties and geometry but also on factors such as temperature, load, and slip conditions. Understanding tire characteristics is essential when building a reliable vehicle simulation model, because every force exchanged with the ground passes through the tires, even minor inaccuracies in tire modeling can lead to significant errors in correlation with the real-world vehicle.

2.1.1 Longitudinal Force

A tractive or braking force F_x must be generated in order to accelerate or decelerate a vehicle with respect to the ground. Since tires are the only point of contact between the vehicle and the road, this force must be transmitted through them.

When a driving torque is applied to the tire in the forward direction, it causes the contact patch to shift rearward. This motion compresses the tread elements at the front of the footprint, resulting in a localized deformation of the tire.

To better understand this behavior, it is useful to introduce the concept of the *rolling radius*, which, in the case of a rigid wheel, is defined by the direct relationship between vehicle speed and angular velocity:

$$V = \omega_0 R \tag{2.1}$$

However, this assumption does not hold true for real tires, which deform under load. In such cases, the center of instantaneous rotation does not coincide with the geometric center of the contact patch. For this reason, the *effective rolling radius* is introduced:

$$V = \omega R_e \tag{2.2}$$

Even under free rolling conditions, longitudinal shear stresses arise due to the variation in radius experienced by each tread element as it enters and exits the contact patch. These stresses are generated as the elements are loaded upon entering the front of the footprint and are released as they unload at the rear, where sliding tends to occur due to reduced vertical force.

In the presence of a tractive force, shear stresses act in the forward direction, causing the tread elements to bend forward relative to the carcass. To determine the overall longitudinal shear stress distribution, the contribution from free rolling must be superimposed on the additional stress due to traction, the result is shown in Figure 2.1(b), depicted as τ_x.

Conversely, during braking, the tread elements are displaced rearward relative to the axle. This compresses the elements behind the contact patch center while stretching those ahead of it. As in the tractive case, the net longitudinal shear stress is obtained by summing the free rolling component with the braking-induced contribution (τ_x in Figure 2.1(a)). Toward the rear of the contact patch, where vertical load decreases, partial sliding occurs between the tread and the road surface.

At this point, the concept of *slip ratio*, denoted as σ, can be introduced. It represents the relative difference between the angular velocity of a driven or braked wheel, ω, and that of a freely rolling wheel, ω_0:

$$\sigma = \frac{\omega - \omega_0}{\omega_0} = \frac{\omega}{\omega_0} - 1 \tag{2.3}$$

This expression allows for some intuitive interpretations. In the case of a freely rolling tire, $\omega R_e / V = 1$, which implies $\omega = \omega_0$, and thus $\sigma = 0$. For a fully locked

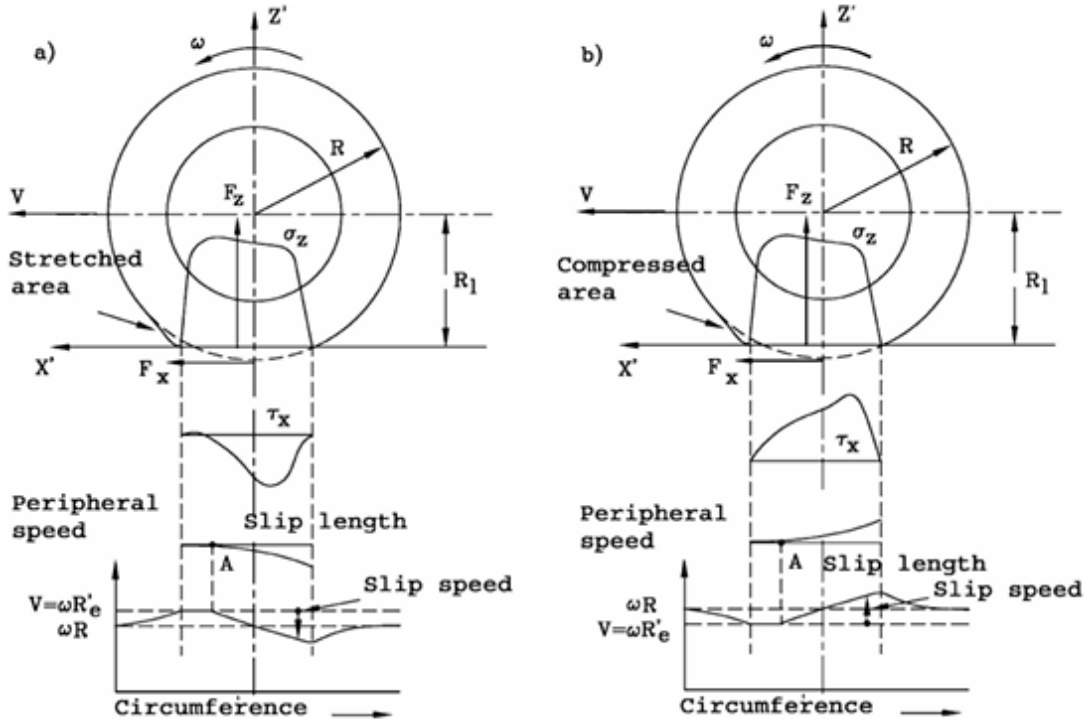

Figure 2.1: Contact pressure distribution for a braking (a) and driving (b) wheel. The rolling radius R'_e is different from that of pure rolling R_e.[2]

(braked) wheel, $\omega = 0$, resulting in $\sigma = -1$. Conversely, in the case of a fully slipping driven wheel (pure traction without grip), $\omega \to \infty$, which leads to $\sigma \to \infty$.

Both tractive and braking forces are strongly dependent on the slip ratio. As slip increases from zero, these forces initially rise steeply, reaching a peak typically within the slip ratio range of 0.15 to 0.2. Beyond this peak, the available force begins to decrease. This decline is particularly abrupt in traction scenarios due to the onset of wheel spin. The overall shape of the force-slip curve is influenced by various factors, including vertical load (F_z) tread and carcass stiffness, road surface conditions, and temperature. On dry surfaces, the traction force tends to drop off rapidly once the tire begins to spin, making post-peak behavior more unstable and difficult to control. In the end, F_x can be normalized with respect to vertical load, F_z, to obtain the friction coefficient μ_x ((2.4)), useful to determine the available grip.

$$\mu_x = \frac{F_x}{F_z} \tag{2.4}$$

2.1.2 Lateral Force

A vehicle turns thanks to lateral tire force generated at the horizontal plane between tire and road, perpendicular to the direction in which the tire is headed.

In the previous section, it was clear that a pneumatic tire can generate longitudinal forces only when deformations occur in the tread band and when a non-zero longitudinal slip is present. Similarly, the generation of lateral forces cannot be understood without considering the lateral deformation of the tire and the presence of a sideslip angle. The *sideslip angle* is defined as the angle between the direction of velocity vector and the heading plane of the wheel and can be described by the following equation:

$$tan(\alpha) = \frac{V_y}{V_x} \tag{2.5}$$

If the velocity of the wheel center does not lie in its mean plane, that is, if the wheel travels with a sideslip angle, the contact patch becomes significantly distorted (Figure 2.2). A tread element initially aligned with the mean plane approaches the ground following the direction of the velocity vector V. After contacting the ground at point A, it continues along this path until point B, where internal elastic forces exceed frictional resistance, causing the tread to slide laterally toward the mean plane.

This results in a contact patch divided into two regions: a leading zone (A to B) with no sliding, and a trailing zone (B to C) where the tread slips. As the sideslip angle increases, the sliding region expands and can eventually dominate the entire contact area. The lateral deformation, vertical stress σ_z, shear stress τ_y, and lateral velocity distributions are shown qualitatively in Figure 2.3.

The resulting lateral force F_y does not act at the center of the contact patch but is shifted rearward by a distance t, defined as the *pneumatic trail*. The *aligning moment*, M_z, is given by (2.6).

$$M_z = F_y t \tag{2.6}$$

This moment tends to realign the wheel with the velocity direction.

Initially, the lateral force F_y increases almost linearly with the sideslip angle α; however, as sliding begins, the rate of increase slows down, eventually stabilizing or slightly decreasing under full sliding conditions. The relationship between F_y and α is governed by the *cornering stiffness*, C, as expressed in Eq. (2.7). This parameter is fundamental for analyzing the lateral behavior of a tire and is influenced by a wide range of factors, including vertical load, tire alignment angles, temperature, and other operating conditions.

$$F_y = -C\alpha \tag{2.7}$$

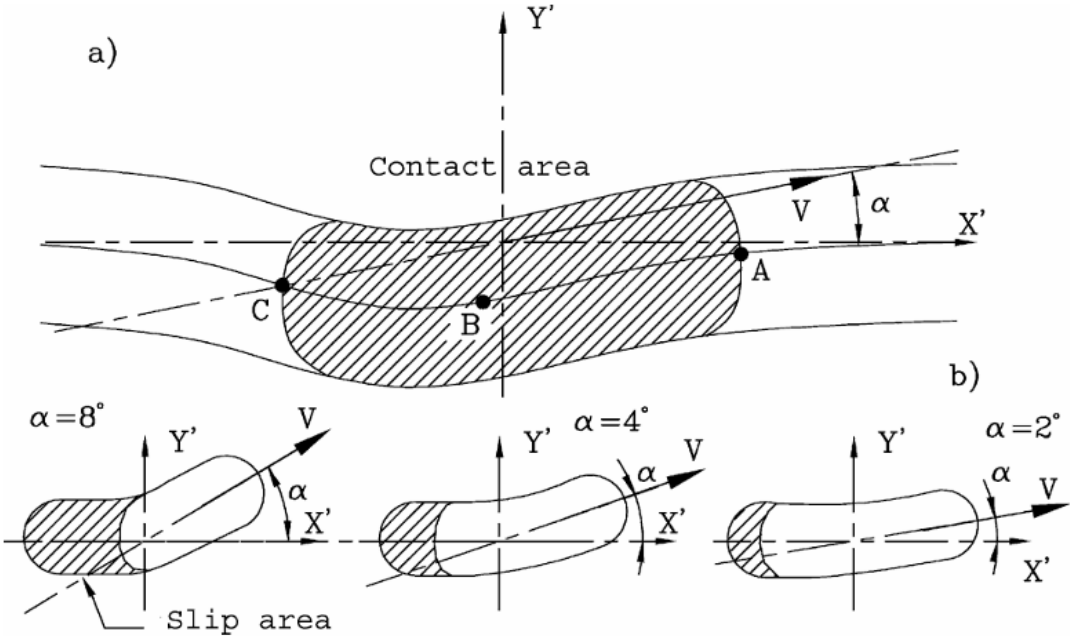

Figure 2.2: Wheel-road contact under sideslip. (a) Trajectory of a tread point on the equatorial plane; (b) contact and slip zones for increasing sideslip angles.[2]

This linear approximation holds for small values of α and is particularly useful in the study of vehicle dynamics, where sideslip angles typically remain small under normal driving conditions.

As in the longitudinal case, the lateral force can be normalized with respect to the vertical load by introducing the *lateral friction coefficient*, μ_y:

$$\mu_y = \frac{F_y}{F_z} \tag{2.8}$$

2.1.3 Elliptical Approximation

The considerations represented previously are valid only when longitudinal and lateral forces are generated independently. However, when a tire is required to produce forces in both directions simultaneously, a trade-off arises: the generation of force in one direction reduces the capacity in the other.

Specifically, applying a driving or braking force to a tire that is already operating at a given sideslip angle leads to a reduction in the available cornering force. Conversely, the longitudinal force capability also decreases when the tire is simultaneously subjected to a lateral load.

Figure 2.4(a) shows a set of experimental curves $F_y(F_x)$ at constant sideslip

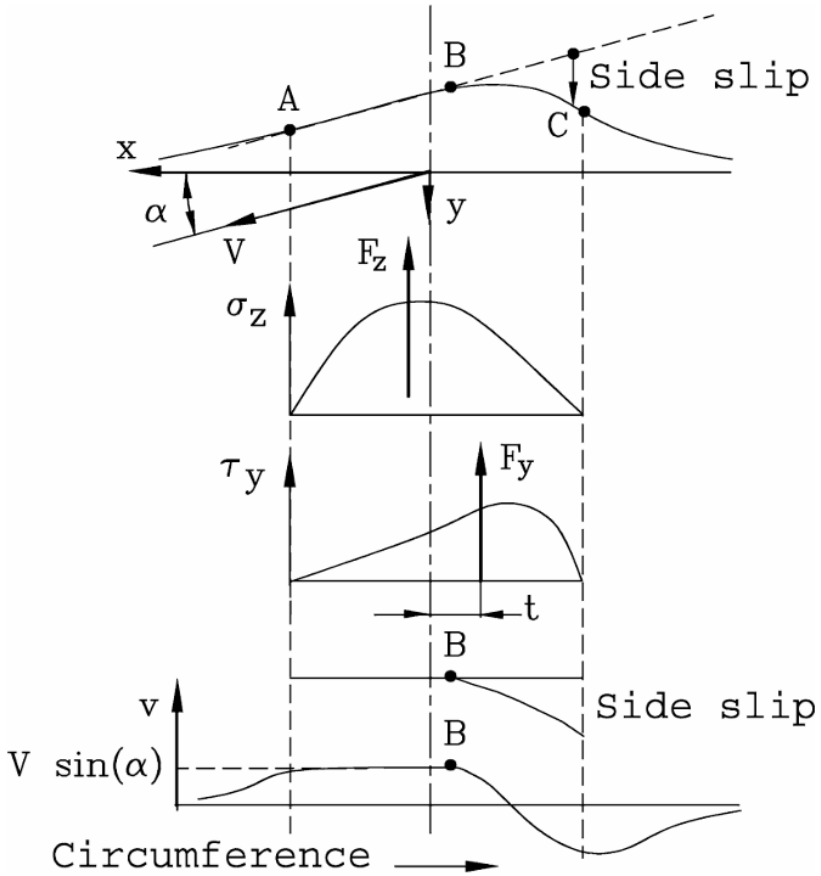

Figure 2.3: Lateral deformation, distribution of pressures σ_z e τ_y, slip and lateral speed in a cornering tire.[2]

angle α. If F denotes the resultant interaction force between the tire and the road surface, with F_x and F_y representing its projections along the longitudinal and lateral directions respectively, the overall friction coefficient can be defined as:

$$\mu = \frac{F}{F_z} = \sqrt{\mu_x^2 + \mu_y^2} \tag{2.9}$$

In simplified models, this envelope is often idealized as a circle commonly referred to as the *friction circle* where the maximum force is considered independent of its orientation.

In reality, however, the maximum longitudinal coefficient μ_x typically exceeds the lateral coefficient μ_y, and asymmetries may arise between traction and braking conditions. The shape of the force envelope, as well as the entire F_y–F_x relationship, is highly dependent on several factors, including load, tire temperature, and road surface properties. A practical way to approximate the measured force limits

is through the *elliptical approximation* as expressed by Equation (2.10), where F_{y0} and F_{x0} denote, respectively, the pure lateral force at a given α and the peak longitudinal force at zero sideslip. The resulting boundary, called the *friction ellipse*, (Figure 2.4(b)) provides a more realistic representation of the tire's combined force capabilities.

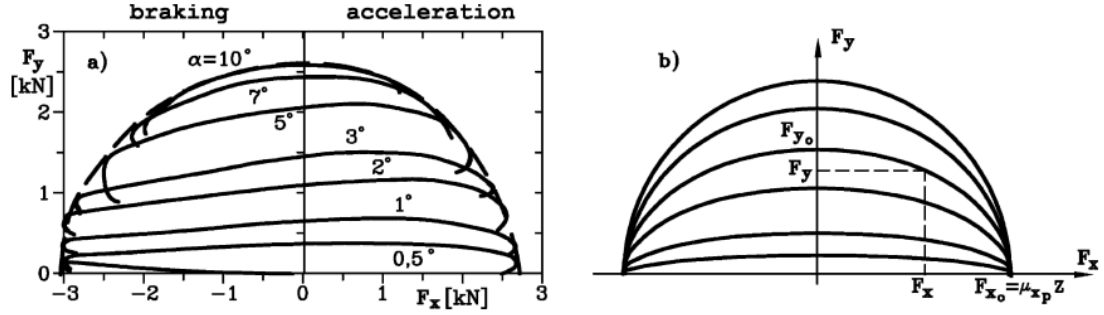

Figure 2.4: (a) Experimental diagrams; (b) friction ellipse.[2]

$$\left(\frac{F_y}{F_{y0}}\right)^2 + \left(\frac{F_x}{F_{x0}}\right)^2 = 1 \tag{2.10}$$

2.1.4 The Pacejka Magic Formula

The *Magic Formula* proposed by Pacejka has become a widely adopted standard in modern tire modeling. This empirical formulation allows the representation of the longitudinal and lateral forces, as well as the self-aligning torque, as functions of the normal load, slip ratio, sideslip angle, and camber angle γ.

The popularity of this model is largely due to its increasing use by tire manufacturers to describe tire performance through a set of calibrated coefficients. If this practice becomes widely adopted, the Magic Formula may serve not only as a reliable and accurate model for tire dynamics, but also as one for which necessary parameter data are readily available.

An example of Magic Formula usage is reported. The longitudinal force F_x as a function of slip ratio σ can be described by the following equation:

$$F_x = D \sin\left(C \arctan\left\{B(1-E)(\sigma + S_h) + E \arctan\left[B(\sigma + S_h)\right]\right\}\right) + S_v \tag{2.11}$$

Here, the parameters B, C, D, E, S_h, and S_v are empirically determined through curve-fitting techniques applied to experimental tire data. They typically depend on variables such as vertical load and camber angle, but do not correspond directly to specific physical properties. The coefficient D indicates the peak force F_x (adjusted

for the offset S_v), while the product BCD defines the initial slope of the force–slip curve.

The derivation of these coefficients is performed by fitting the model to experimental measurements, often using nonlinear least squares or genetic algorithms, to minimize the discrepancy between observed and predicted tire forces. This process ensures that the resulting model closely captures the actual tire behavior under various operating conditions. If symmetric behavior of F_x is assumed for both positive and negative slip values, the same formulation can be used to describe both traction and braking regimes.

In conclusion, the Magic Formula represents a widely used approach for modeling tire behavior with good accuracy. Thanks to its ability to fit experimental data and the availability of standardized coefficients from manufacturers, it offers a reliable foundation for tire force prediction in vehicle dynamics studies.

2.2 Vehicle Dynamics

In order to investigate some vehicle dynamics performance indicators in the validation phase, a brief theory review is reported in this section.

Accurately representing vehicle dynamics is essential in the design and control of automotive systems, especially for performance evaluation, control strategy development, and integration with powertrain models. Among the various modeling approaches, the single-track vehicle model (or bicycle model) offers a simplified yet effective framework for describing planar vehicle motion, capturing key aspects of lateral and longitudinal dynamics with reduced computational complexity.

To assess a vehicle's dynamic capabilities, the G-G diagram is commonly used as a graphical representation of the combined acceleration limits. It allows for a clear visualization of the traction, braking, and cornering limits of the vehicle under varying conditions.

This chapter presents the fundamental principles behind the single-track vehicle model and the construction and interpretation of the G-G diagram, which together provide a solid foundation for understanding vehicle behavior in dynamic scenarios.

2.2.1 Single-Track Vehicle Model

To approach vehicle handling, a simplified mathematical model is used, in which the vehicle motions are described under the assumption of steady-state cornering maneuver and low speed maneuver.

The single-track model or bicycle model is considered. It is characterized by single tire per axle, along with some other assumptions that are introduced below:

- no lateral load transfer is present

- no longitudinal load transfer is present
- no rolling or pitching motions are considerate
- tires work in linear range, so there is no cornering stiffness saturation
- vehicle speed is constant
- no chassis or suspension compliance is present

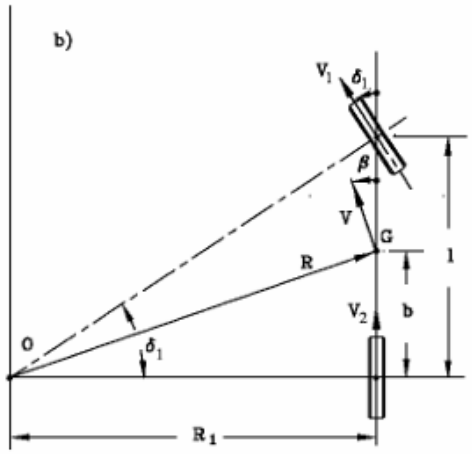

Figure 2.5: Bicycle Model.[2]

Referring to Figure 2.5, and considering small angles and R sufficiently large, it is possible to write the following equations:

$$\tan \delta_f = \frac{l}{R} \tag{2.12}$$

$$R = \sqrt{b^2 + R_1^2} = \sqrt{b^2 + (l \cdot \cot \delta_f)^2} \simeq l \cdot \cot \delta_f \simeq \frac{l}{\delta_f} \tag{2.13}$$

Equation (2.13) can be rearranged to obtain the *curvature gain*:

$$\frac{1}{R\delta_f} = \frac{1}{l} \tag{2.14}$$

The curvature gain during high-speed and complex maneuvers will no more be correlated to 1/l, but its analysis allows for some interesting considerations regarding understeer and oversteer.

In particular, also *understeer angle* is an important measure and it can be computed in the following way:

$$m \cdot a_y = m \cdot \frac{V^2}{R} \Rightarrow R = \frac{V^2}{a_y} \tag{2.15}$$

And combining (2.15) with (2.14):

$$\delta_f = \frac{l \cdot a_y}{V^2} \tag{2.16}$$

And finally understeer angle is defined in (2.17):

$$\delta_u = \delta - \delta_f \tag{2.17}$$

where, δ_f is the kinematic steering angle, δ is the actual steering angle computed knowing steering wheel angle and steering kinematics, and V is speed $[m/s]$.

The understeer angle can be averaged during a lap to obtain a measure of the car behavior, but it is important to remember that is obtained by a single-track vehicle model, which can give only quantitative results. This means that a negative value is not directly linked to oversteering car and vice versa for a positive value, but usually only a dramatic oversteering car will reach negative values if averaged over a lap. In the end, it is a key parameter for comparing two cars or setups, but it should not be considered an absolute value.

2.2.2 G-G Diagram

The G-G diagram concept comes from the tire friction circle, introduced in Section 2.1, which assumes that the maximum horizontal force that a tire can exploit is independent from the direction of application. The idea is to collapse the four tires friction circles into a unique equivalent representing the *vehicle friction circle* (Figure 2.6).

In reality, a vehicle is rarely able to fully exploit the theoretical limits defined by the friction circle. Several factors contribute to this discrepancy. Traction is often limited by the power available from the powertrain, preventing the tires from reaching the maximum combined force. During maneuvers, both lateral and longitudinal load transfers cause significant variations in normal force distribution among the wheels, altering the actual grip available at each tire due to load sensitivity. In a race car, aerodynamics plays a crucial role, as it significantly affects tire grip and, consequently, the size and shape of the G-G diagram. Both downforce and aerodynamic drag increase with the square of the vehicle speed. As a result, greater downforce improves grip during cornering and braking, enhancing vehicle performance in these phases. On the other hand, increased drag negatively impacts acceleration, limiting the car's straight-line capabilities.

Moreover, suspension geometry, mechanical compliance, and component flexibility can lead to unexpected changes in camber and wheel orientation under

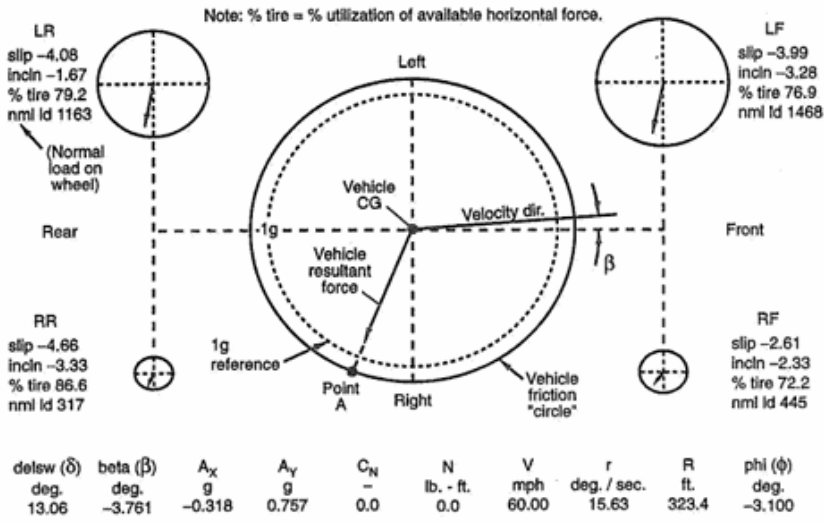

Figure 2.6: Tire friction circles combined to form the vehicle friction circle.[3]

dynamic conditions, further reducing effective tire performance. Additionally, it is uncommon for all four wheels to reach their traction limits simultaneously. For example, understeer occurs when the front tires lose grip while the rear still retains it, resulting in only partial use of the friction potential. Finally, suboptimal brake balance can prevent the simultaneous saturation of front and rear tire forces, limiting the vehicle's ability to operate at the edge of the friction envelope.

In the end, to obtain a G-G diagram, the last step is to normalize the resultant forces by dividing them by the vehicle mass, thus obtaining the longitudinal and lateral accelerations. In real-world applications, what is actually recorded and plotted are these accelerations directly. The objective of this diagram is to represent vehicle performance throughout a specific maneuver or to assess driver and vehicle behavior by analyzing the portion of the graph that is utilized during various maneuvers or throughout an entire lap.

In Figure 2.7, a GGV (G-G-Velocity) plot is presented. This type of graph includes a third axis to indicate the vehicle speed at which a given acceleration is achieved. Ideally, for a vehicle with a negative aerodynamic lift coefficient, higher accelerations are expected at higher speeds due to the increased available grip generated by aerodynamic downforce.

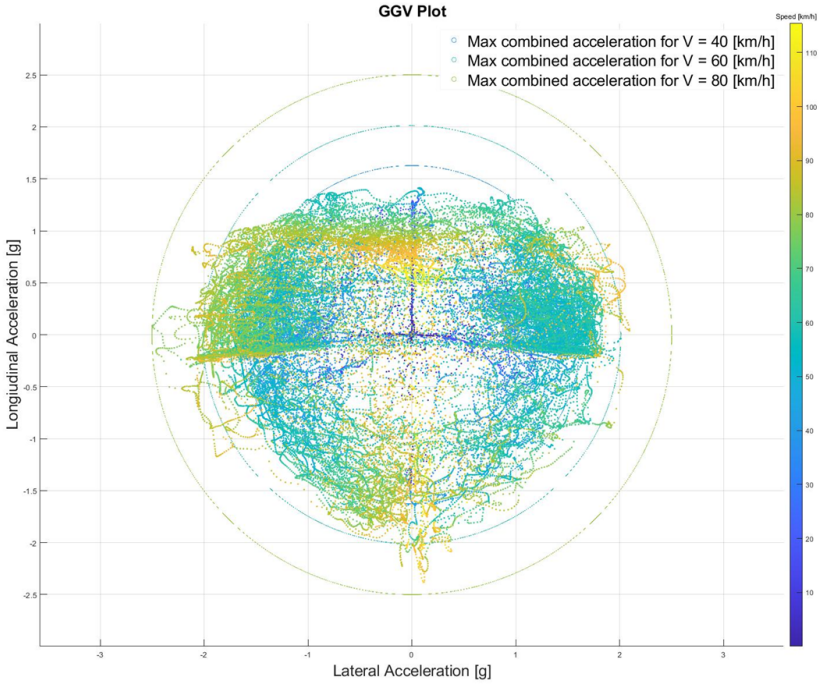

Figure 2.7: GGV plot.

2.3 Heat Exchange

In the thermal modeling of cooling circuits, an accurate understanding of heat transfer mechanisms is essential for predicting temperature distributions and validating the thermal behavior of critical components. Among the various forms of heat exchange, conduction and convection represent the dominant modes through which thermal energy is transported within and away from components.

Conduction governs heat flow through solid media, where thermal gradients drive energy transfer from hotter to cooler regions. Conversely, convection is responsible for heat exchange between surfaces, and surrounding cooling fluids, playing a crucial role in vehicle's overall thermal management strategy.

This section provides a theoretical overview of conduction and convection heat transfer. The objective is to establish a solid foundation for the modeling approaches adopted in later sections of this thesis, where thermal performance validation is carried out on specific components of cooling circuits and electrical machines.

2.3.1 Conductive

When a temperature difference is present in a solid or stationary fluid, heat transfer occurs by conduction. This phenomenon originates from microscopic interactions:

particles with higher energy transfer thermal energy to adjacent, less energetic particles due to intermolecular collisions.

The rate of heat conduction can be quantified using a constitutive law known as *Fourier's law*. In the case of steady-state, one-dimensional conduction through a plane wall of thickness L, with temperature distribution $T(x)$, Fourier's law is expressed as:

$$q''_x = -k \cdot \frac{dT}{dx} \tag{2.18}$$

where:

- q''_x is the heat flux in the x-direction, expressed in $\mathrm{W/m^2}$,
- k is the thermal conductivity of the material, in $\mathrm{W/(m \cdot K)}$,
- $\frac{dT}{dx}$ is the temperature gradient along the x-axis.

The negative sign in Equation (2.18) reflects that heat flows from regions of higher temperature to regions of lower temperature.

In steady-state conditions where the temperature distribution is linear, the temperature gradient simplifies to:

$$\frac{dT}{dx} = \frac{T_2 - T_1}{L} \tag{2.19}$$

Substituting this into Equation (2.18) yields:

$$q''_x = -k \cdot \frac{T_2 - T_1}{L} \tag{2.20}$$

In which T_1 and T_2 are respectively the higher and lower temperature surface. These expressions form the foundation for modeling conductive heat transfer in thermally loaded systems, including electrical machines and power electronics.

One-Dimensional Radial Systems

Understanding heat transfer in radial geometries is particularly important when analyzing cylindrical systems such as electric machines. These configurations often exhibit temperature variation primarily along the radial direction, allowing a one-dimensional approximation for thermal analysis.

A typical scenario is that of a hollow cylinder with its inner and outer surfaces subjected to different fluid temperatures. Assuming a steady-state regime with no internal heat generation, the temperature distribution along the radial direction r can be described as:

$$T(r) = \frac{T_{s,1} - T_{s,2}}{\ln(r_1/r_2)} \ln\left(\frac{r}{r_2}\right) + T_{s,2} \tag{2.21}$$

With equation terms referring to Figure 2.8

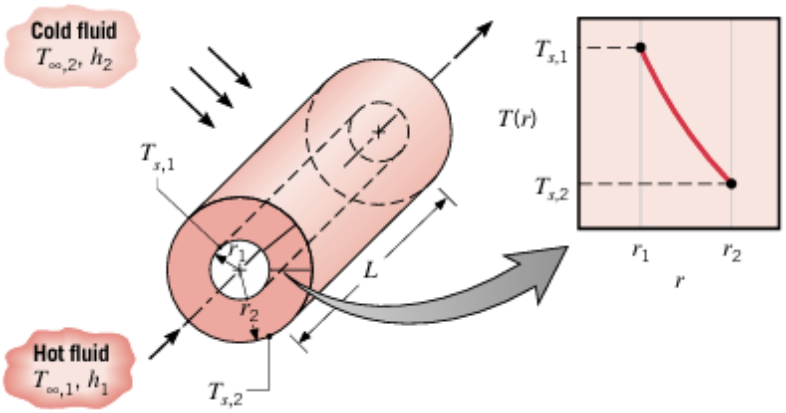

Figure 2.8: Hollow cylinder with convection surface conditions and logarithmic temperature distribution.[4]

This expression is obtained by solving the heat conduction equation in cylindrical coordinates under steady-state conditions. To calculate the associated heat flux, Fourier's law must be adapted for cylindrical geometry, yielding:

$$q_r = -kA\frac{dT}{dr} = -k(2\pi rL)\frac{dT}{dr} \tag{2.22}$$

Here, the term $A = 2\pi rL$ represents the lateral area perpendicular to the radial direction at position r, where L is the axial length of the cylinder.

By applying the general solution for the temperature profile (2.21) into Fourier's law (2.22), the radial heat transfer rate, which remains constant at any radius in the absence of internal sources, can be derived as:

$$q_r = \frac{2\pi Lk(T_{s,1} - T_{s,2})}{\ln(r_2/r_1)} \tag{2.23}$$

This form highlights the logarithmic dependence of heat transfer on the geometry. It is also possible to represent this behavior using a thermal resistance model, where the conductive resistance across the cylindrical shell is expressed as:

$$R_{t,\text{cond}} = \frac{\ln(r_2/r_1)}{2\pi Lk} \tag{2.24}$$

This formulation is useful in lumped thermal network models and provides a compact means to incorporate radial conduction effects into broader system-level thermal simulations.

2.3.2 Convective

Convection describes the mechanism of heat transfer between a surface and an adjacent fluid when a temperature difference exists between the two. This process combines two fundamental modes of energy transport. First, there is heat conduction due to the random thermal motion of molecules. Second, energy is carried by the bulk movement of fluid elements, which is a result of large-scale motion within the fluid.

In the presence of a temperature gradient, this organized fluid motion enhances the rate of thermal energy transport. Since the molecular motion persists within moving fluid parcels, the net heat transfer reflects a combination of both random microscopic activity and macroscopic flow. The overall effect is referred to as convection, while the transport linked specifically to the bulk motion of the fluid is known as *advection*.

Convection processes are typically categorized based on how the fluid motion is generated. In *forced convection*, the fluid is driven by an external device such as a fan, blower, or pump. In contrast, *natural* or *free convection* occurs when fluid motion results from buoyancy effects caused by spatial temperature-induced density variations. Furthermore, convection scenarios are often divided into internal flow, occurring within ducts or pipes, and external flow, where the fluid moves over solid boundaries.

Regardless of the classification, the rate of heat transfer between the surface and fluid is often quantified using *Newton's law of cooling*, which is expressed as:

$$q'' = h(T_s - T_\infty) \tag{2.25}$$

In this equation:

- q'' is the rate of convective *heat flux* [W],
- h is the convective *heat transfer coefficient* [W/m^{2}K],
- T_s is the surface temperature [K],
- T_∞ is the temperature of the fluid far from the surface [K].

When applying Eq. (2.25), the direction of heat transfer determines the sign of the convection heat flux. Specifically, the heat flux is considered positive when thermal energy flows away from the surface, that is, when $T_s > T_\infty$. Conversely, if

the fluid is warmer than the surface ($T_\infty > T_s$), the heat flux becomes negative, indicating that heat is being transferred to the surface.

The convection coefficient, h, is determined by the characteristics of the boundary layer that forms near the surface. Its value is affected by several factors, including the geometry of the surface, the type of fluid flow (laminar or turbulent), and various fluid properties such as thermal conductivity, viscosity, and specific heat.

Convective Heat Transfer Coefficient Estimation

In the study of convective heat transfer, the primary objective is to determine the convection coefficient, h, under various flow conditions and geometries, using different working fluids. Given the large number of variables involved in any convective scenario, the goal is to express the heat transfer characteristics using universal relationships formulated in terms of dimensionless groups with physical significance.

One such key dimensionless group is the *Nusselt number*, Nu, which characterizes the dimensionless temperature gradient at the surface and serves as an indicator of the convective heat transfer rate. It is defined as:

$$\mathrm{Nu} = \frac{hL}{k} \tag{2.26}$$

where h is the convection heat transfer coefficient [$\mathrm{W/(m^2\,K)}$], L is the characteristic length of interest [m], and k is the thermal conductivity of the fluid [$\mathrm{W/(m\,K)}$].

Based on both analytical solutions and experimental data, it has been established that, for forced convection, the local and average convection heat transfer coefficients can be expressed using empirical correlations of the general form:

$$\mathrm{Nu}_x = f(x^*, \mathrm{Re}_x, \mathrm{Pr}) \qquad \overline{\mathrm{Nu}_x} = f(\mathrm{Re}_x, \mathrm{Pr}) \tag{2.27}$$

Here, the subscript x has been introduced to indicate that the parameters are evaluated at a specific location along the surface, identified by the dimensionless coordinate x^*. The overbar notation, as in $\overline{\mathrm{Nu}}$, denotes an average value over the surface extending from $x^* = 0$ to the location of interest.

In these expressions, the Reynolds number, Re_L, quantifies the ratio of inertial to viscous forces and is used to characterize boundary layer development:

$$\mathrm{Re}_L = \frac{VL}{\nu} \tag{2.28}$$

where V is the reference fluid velocity, L is the characteristic length of the surface, and ν is the kinematic viscosity of the fluid.

The Prandtl number, Pr, is a dimensionless property of the fluid that indicates the relative thickness of the velocity and thermal boundary layers. It is defined as:

$$\mathrm{Pr} = \frac{\nu}{\alpha} \tag{2.29}$$

where α is the thermal diffusivity of the fluid.

As an example, the general correlation form for forced convection over flat plates or other immersed geometries is therefore:

$$\overline{\mathrm{Nu_x}} = C \cdot {\mathrm{Re_x}}^m \cdot \mathrm{Pr}^n \tag{2.30}$$

The constants C, m, and n are independent of the fluid but depend on the surface geometry and the flow regime (laminar or turbulent). A similar expression is applicable for forced convection in internal flows, although the boundary layer development differs from that of external flow.

Instead, in the case of free (natural) convection, fluid motion is driven by buoyancy forces resulting from a temperature difference between the surface (T_s) and the surrounding fluid (T_∞). The flow behavior in such scenarios is characterized by the *Grashof number*, defined as:

$$\mathrm{Gr}_L = \frac{g\beta(T_s - T_\infty)L^3}{\nu^2} \tag{2.31}$$

where g is the gravitational acceleration and β is the thermal expansion coefficient of the fluid.

The local and average Nusselt numbers for free convection are given by correlations of the form:

$$\mathrm{Nu}_x = f(x^*, \mathrm{Gr}_x, \mathrm{Pr}) \qquad \overline{\mathrm{Nu}}_x = f(\mathrm{Gr}_x, \mathrm{Pr}) \tag{2.32}$$

These equations are structurally similar to those used for forced convection (Eq. 2.27), with the Grashof number replacing the Reynolds number to reflect the nature of the driving force in free convection. Since the product $\mathrm{Gr} \cdot \mathrm{Pr}$ appears frequently in natural convection analysis, it is often grouped into a single dimensionless parameter known as the Rayleigh number:

$$\mathrm{Ra}_L = \mathrm{Gr}_L \cdot \mathrm{Pr} = \frac{g\beta(T_s - T_\infty)L^3}{\nu\alpha} \tag{2.33}$$

It possesses the same physical interpretation as the Grashof number, representing the ratio of buoyancy to viscous forces within the flow field.

2.4 Electrical Machines

A solid understanding of electrical machine fundamentals is essential for a proper approach to both electrical and thermal validation. The following section provides a review of IPM (Internal Permanent Magnet) motors, mechanisms of heat generation, and relevant thermal modeling strategies.

2.4.1 IPM Motor

AMK motors are internal permanent magnets motors and so, a brief discussion about them is conducted. The Interior Permanent Magnet motor is a specific type of Permanent Magnet Synchronous Machine (PMSM), widely used in electric vehicle powertrains and high-performance industrial applications. Unlike the Surface Permanent Magnet (SPM) motor, where the magnets are mounted on the outer surface of the rotor, the IPM motor features permanent magnets embedded within the rotor core. This structural distinction leads to several key performance and control advantages, making IPMs particularly attractive in automotive systems such as traction drives.

Rotor Structure and Magnetic Saliency

In an IPM motor, the magnets are housed in cavities cut into the iron rotor, typically arranged in a V-shape or similar configurations to optimize the magnetic path. This internal placement not only protects the magnets from mechanical stress and demagnetization at high speeds, but also introduces saliency in the rotor design. Saliency means the rotor exhibits different inductance values along the d-axis and q-axis (magnetic axes), which is not the case in SPM motors.

This saliency allows the motor to generate torque through both permanent magnet flux and reluctance torque, a phenomenon known as hybrid torque production. As a result, IPM motors can deliver higher torque density and improved efficiency, especially under variable load conditions and at high speeds.

Control Strategies

Due to their salient rotor design, IPM motors require more sophisticated control algorithms compared to SPM or induction motors. The most common approach is Field-Oriented Control (FOC), which decouples torque and flux control for precise and dynamic performance. Additionally, Maximum Torque per Ampere (MTPA) control strategies are used to optimize current usage and minimize losses during low and medium-speed operation, while field-weakening techniques are employed at high speeds to prevent overvoltage in the inverter.

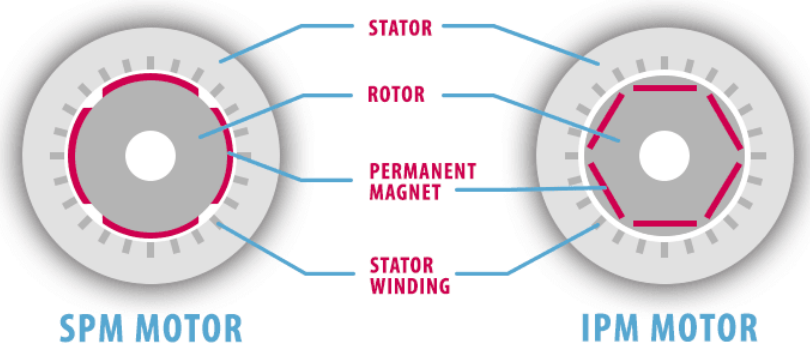

Figure 2.9: SPM and IPM comparison.[5]

2.4.2 Heat Generation

In an electric machine, power is dissipated in three ways:

- **Joule losses in conductors**: copper losses, they are the most relevant in an electric machine. They are related with the square of the current.
- **Hysteresis and eddy current losses in magnetic materials**: iron losses. They are caused by alternating magnetic fields, hysteresis losses result from the lag of magnetization, while eddy currents generate heat due to circulating currents in the core.
- **Friction and ventilation losses**: mechanical losses. Friction occurs in bearings and moving parts, while ventilation losses arise from air resistance caused by internal or external cooling fans.

Dissipated power degrades into heat warming-up the motor. Excessive heating in an electric machine can compromise the integrity of the insulating materials, leading to a gradual loss of their dielectric properties. This degradation not only affects the machine's performance but can ultimately result in functional failure. Since the longevity of insulation directly influences the overall lifespan of the machine, effective thermal management is crucial. Elevated temperatures also reduce the durability of mechanical components, such as lubricated bearings, and can alter the physical properties of structural materials. These thermal effects collectively impact both the efficiency and reliability of the machine over time.

2.4.3 Stator Winding

One key parameter in stator winding design is the slot fill ratio, which indicates how much of the slot's volume is occupied by copper wire. A higher fill ratio is

generally preferred to reduce resistance losses and increase power density.

End turns refer to the part of the winding that extends beyond the stator core. While necessary to complete the winding circuit, they do not contribute to torque production and add resistance and material cost. Minimizing end turn length improves efficiency, especially in short-stack motors.

Possible winding techniques are the following:

- **Hand Cable Winding (Random)**: hand-wound coils are often used in prototypes or small series. This method allows flexibility and can sometimes achieve higher slot fill than machine-wound options. However, it depends heavily on operator skill and may introduce variability. Hand wiring can be implemented in several configurations. It is important to specify whether the coils are manually wound and then inserted by hand, the coils are directly wound around the stator teeth by hand, or the coils are wound using a machine but subsequently inserted manually. The typical slot fill ratio is around 35–45%

- **Distributed Winding**: in distributed winding, coils are spread over several slots, creating a smoother magnetic field and electro magnetic field (EMF) waveform. This method is commonly used in permanent magnets (PM) brushless motors and tends to have lower harmonic content and armature reaction. High slot fill is achievable, particularly in larger motors.The typical slot fill ratio is around 40–55%

- **Concentrated Winding**: all turns are wound into a single coil per pole. These windings have shorter end turns, are simpler to manufacture, and are well-suited for automated production. Although they tend to produce more harmonics and higher armature reaction, they can improve efficiency by reducing copper volume and losses. The typical slot fill ratio is around 50-60%

- **Conductor Bars**: used in large motors and generators, conductor bars are bundles of insulated wires, often rectangular for better slot utilization. They are preformed, insulated (e.g., mica and epoxy), and connected at the ends. Care is required during compression and assembly to avoid insulation damage. Post-winding tests like hipot and surge are essential to ensure quality. The typical slot fill ratio is around 55-70%

2.4.4 Thermal Modelling: Lumped Parameter Thermal Network

Thermal analysis is a critical aspect of electric machine design due to coupling between thermal and electromagnetic phenomena. Temperature variations directly influence several key machine parameters. For instance, an increase in winding

temperature leads to higher copper resistance, resulting in greater Joule losses and a consequent drop in overall efficiency. Similarly, elevated temperatures in permanent magnets reduce their magnetic flux output, which in turn diminishes the machine's torque capability.

Several methodologies are commonly employed to assess thermal behavior in electrical machines. Among the most adopted are the Lumped-Parameter Thermal Network (LPTN), Finite Element Analysis (FEA), and Computational Fluid Dynamics (CFD). Each approach offers different levels of detail, complexity, and computational demand.

LPTN models, in particular, are widely recognized for their balance between simplicity and accuracy. These models approximate the thermal system using an analogy with electrical circuits, thermal resistances are represented as electrical resistors, and thermal masses as capacitors. This circuit-based approach enables an intuitive understanding of heat flow paths and facilitates efficient simulations, especially under transient conditions such as the one that can be encountered during drive cycle analysis.

One of the notable strengths of LPTN models lies in their computational efficiency, which allows for rapid simulations and makes them particularly suitable for iterative design processes and sensitivity studies. Moreover, their reduced-order nature makes them valuable tools for system-level thermal modelling, where a detailed full-order numerical model would be computationally excessive.

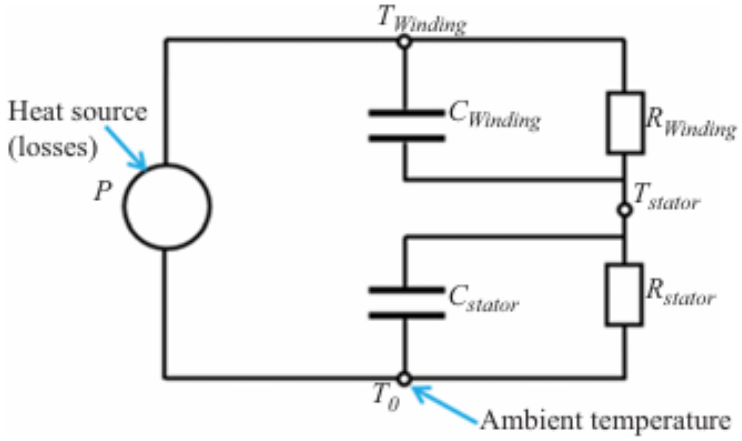

Figure 2.10: Equivalent thermal circuit.[6]

To illustrate the principle of LPTN modelling, an example of simplified thermal network is shown in Figure 2.10. In this model, thermal resistances represent the machine's heat dissipation paths and are estimated based on steady-state temperature differences and known power losses. The winding temperature rise

due to power dissipation P can be expressed as:

$$T_{\text{winding}} = T_0 + RP \tag{2.34}$$

Here, T_0 denotes the ambient temperature, and R is the equivalent thermal resistance.

By introducing thermal masses (capacitances) into the model, it becomes possible to capture the time-dependent heating and cooling behavior of the system. The temperature increase of the winding over time is described by:

$$T_{\text{winding}} - T_0 = (T_s - T_0)\left(1 - e^{-\frac{t}{\tau}}\right) \tag{2.35}$$

In this equation, T_s represents the steady-state winding temperature, while τ is the thermal time constant of the system, defined as:

$$\tau = RC \tag{2.36}$$

The thermal capacitance C can be calculated using the material's physical properties:

$$C = \rho V c \tag{2.37}$$

where ρ is the material density, V is the volume, and c is the specific heat capacity.

Figure 2.11 demonstrates a typical temperature profile of a loaded electric machine. Notably, the winding reaches its steady-state temperature more quickly than the stator yoke due to a smaller thermal time constant. This behavior is expected, as the yoke generally possesses greater thermal mass and higher thermal resistance.

It is important to note that the empirically derived equivalent resistance in the LPTN model encapsulates a variety of heat transfer mechanisms: conduction through laminated steel, windings, and bearings; thermal contact resistance at material interfaces; convection around the end windings and machine housing; and radiative heat exchange with the environment. Because these empirical resistances are influenced by the machine's materials, construction techniques, and geometry, they are only valid within a limited range of designs. Modifying any of these factors may significantly alter the thermal response, potentially reducing the accuracy of a single-resistance model in new configurations.

2.4.5 Thermal Modelling: Finite Elements Methods

Both FEA and CFD rely on a detailed representation of the machine's geometry, which is discretized into smaller mesh elements, control volumes, or cells. Within

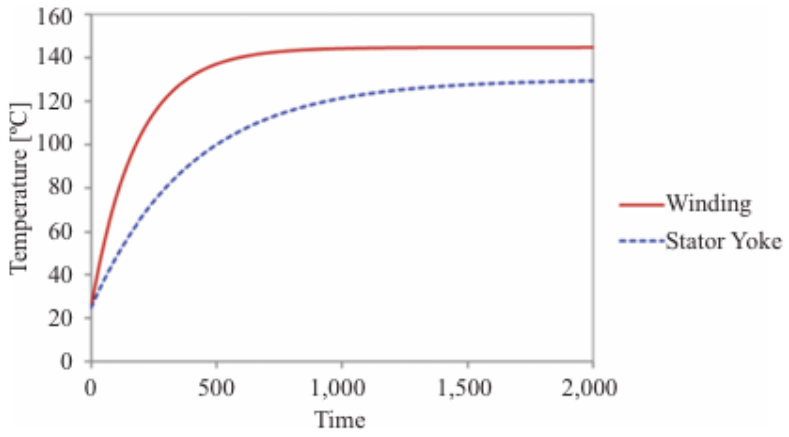

Figure 2.11: Influence of thermal time constant on winding and stator iron temperature rise.

each of these discrete regions, thermal or fluid flow variables are assumed to remain uniform. FEA is commonly employed to analyze individual components within an electrical machine where heat transfer occurs predominantly by conduction. In many cases, useful results can be obtained using two-dimensional models; however, three-dimensional simulations, while offering greater accuracy, are less frequently used due to the additional computational cost and complexity associated with their setup and solution.

CFD, on the other hand, is particularly suited for simulating fluid motion and convective heat transfer over component surfaces. These simulations are almost exclusively three-dimensional, and while they can be applied to isolated components or even the entire machine, full-system models tend to be significantly more complex and time-consuming to construct and solve. Some degree of conduction modeling may also be incorporated within CFD frameworks when the geometry and material properties are well defined.

Nonetheless, conduction modeling in certain machine regions presents some difficulties. A notable example is the stator slot, which includes a mix of materials such as copper windings, insulation layers, impregnation resins, slot liners, and potential air gaps, each with distinct thermal properties. Given this level of complexity, it is often impractical to achieve reliable results using a simplified lumped-parameter thermal network, particularly if detailed geometric and material data are unavailable.

In such cases, FEA serves as a powerful alternative, offering improved accuracy in predicting conduction heat transfer within geometrically complex regions. When coupled with electromagnetic models, thermal FEA can yield detailed temperature distributions. However, it is important to recognize that FEA alone is not capable

of resolving convective or interface heat transfer without additional input.

For convective boundary conditions, FEA typically requires pre-defined heat transfer coefficients. These are either obtained from empirical correlations or derived from CFD simulations. Despite its precision, applying FEA to the full thermal analysis of an electric machine remains computationally expensive. For this reason, FEA is often used as a calibration tool to fine-tune parameters, in an LPTN model, ensuring that the simplified network reproduces the same thermal response. Additionally, FEA can help identify localized hot spots, particularly within windings, which in turn informs more effective thermal management strategies such as targeted cooling at critical regions.

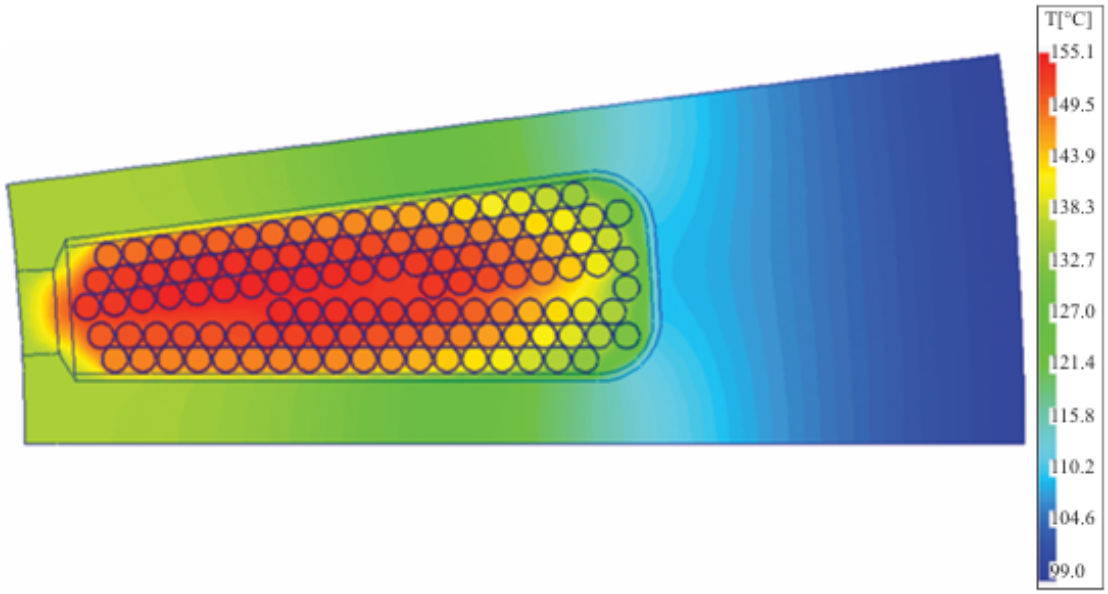

Figure 2.12: Thermal FEA solution for a stator slot with distributed winding.[6]

2.4.6 Thermal Modelling: Computational Fluid Dynamics

In the thermal management of electrical machines, both conduction and convection play essential roles. While heat conduction occurs within the machine components, a significant portion of the heat is dissipated through convection to a surrounding cooling medium. This convective heat transfer may occur passively, such as natural convection from the outer surface of the frame, or actively through engineered cooling systems like forced-air or liquid cooling circuits.

For relatively simple geometries, such as straight ducts under forced convection or external surfaces exposed to natural convection, heat transfer can be estimated analytically, as outlined in Section 2.3.2. However, in more complex configurations

commonly found in practical machine designs, a more detailed approach is required. The governing equations for fluid flow and heat transfer are the Navier-Stokes equations, which describe momentum and energy transport in fluids. These equations admit analytical solutions only for highly idealized cases, such as laminar flow over a flat plate or within a long, straight pipe, scenarios that are rarely encountered in actual machine geometries.

To address these complexities, computational fluid dynamics offers a numerical means of solving the Navier-Stokes equations in arbitrarily complex geometries. The CFD approach involves discretizing the fluid domain into a finite number of control volumes or cells. Within each cell, fluid properties such as pressure, velocity, and temperature are assumed to be spatially uniform. The partial differential equations governing fluid flow are then transformed into algebraic equations, which can be solved iteratively to obtain the distribution of the relevant variables throughout the domain.

CFD can be leveraged in several ways for the thermal modeling of electrical machines:

1. **Derivation of Convective Heat Transfer Coefficients for LPTNs**
   Lumped-parameter thermal networks require input parameters such as thermal resistances to represent heat transfer paths within the machine, as said previously (Section 2.4.4). While resistances associated with conduction can be calculated from geometric and material data, those associated with convection are less straightforward to determine, particularly in regions with complex geometries, such as end windings. In these cases, CFD can be used to simulate the local fluid flow and thermal behavior, providing accurate convective heat transfer coefficients. These values can then be used to refine LPTN models and improve their predictive accuracy.

2. **Comprehensive Thermal Modeling**
   Since CFD can handle both conduction in solids and convection in fluids, it is possible to construct a full thermal model of an electrical machine using CFD alone. Such models allow for detailed temperature and heat flux distributions to be captured throughout the machine, offering high-resolution insights not achievable with simplified approaches. However, this level of detail comes at the cost of significantly greater computational effort. The development, meshing, and solution of a full CFD model require substantial resources and time, both in terms of setup and computation.

3. **Estimation of Air Friction Losses**
   CFD is also a valuable tool for evaluating mechanical losses due to air friction (ventilation losses) in rotating machines. These losses can be estimated by integrating the shear stress and pressure distributions acting on the rotating

surfaces, allowing for the computation of torque losses associated with rotor surfaces and auxiliary components such as cooling fans.

Since its early adoption in the 1990s, CFD has become an established tool in the development and optimization of thermal models for electric machines. Its integration with LPTNs allows for a hybrid modeling approach that balances computational efficiency with physical accuracy, making it a widely accepted practice in contemporary machine design.

Chapter 3

Methodology

In this chapter, the methodology used to model and implement the entire vehicle is described. Each subsystem is analyzed both from the real-world and simulation perspective, with a detailed explanation of the engineering principles behind each modeling choice. These decisions are crucial, as they directly affect the final simulation accuracy and help to explain any potential deviation from real-world behavior.

To ensure consistency across the various physical domains and to maintain modularity and clarity, Simscape libraries from MATLAB & Simulink have been used extensively. This approach also supports future integration.

The chapter is structured to mirror the actual development process: beginning with mechanical modeling and vehicle dynamics, continuing with the implementation of the powertrain and thermal subsystems, and concluding with the overall integration of the complete model. Particular attention is paid to the trade-offs and assumptions adopted in each phase, which are critical to understanding the strengths and limitations of the final simulation environment.

3.1 Simscape Vehicle Model Overview

As said before, Simscape is used to design any subsystem inside Simulink environment, which is very useful because it is possible to model any physical component using block diagrams with physical linkage to each other. This is very powerful because there is no need to write a piece of code to describe the physical laws for a specific component; they are already implemented in the Simscape block.

The starting base for everything is the *Simscape Vehicle Templates* released in 2020 by Mathworks in which several vehicle models are already present with possible customization of their component such as: suspension, body, powertrain, etc. Typical automotive ISO maneuvers can be executed, or it is possible to create a new one with the open-loop driver and the right inputs, even important motorsport tracks are at disposal and everything is ready for simulations. Between all the vehicles, a Formula SAE is represented and this one in particular has been the starting point for the project.

The whole model (Figure 3.1) is composed by 3 main systems: driver, controller, and vehicle.

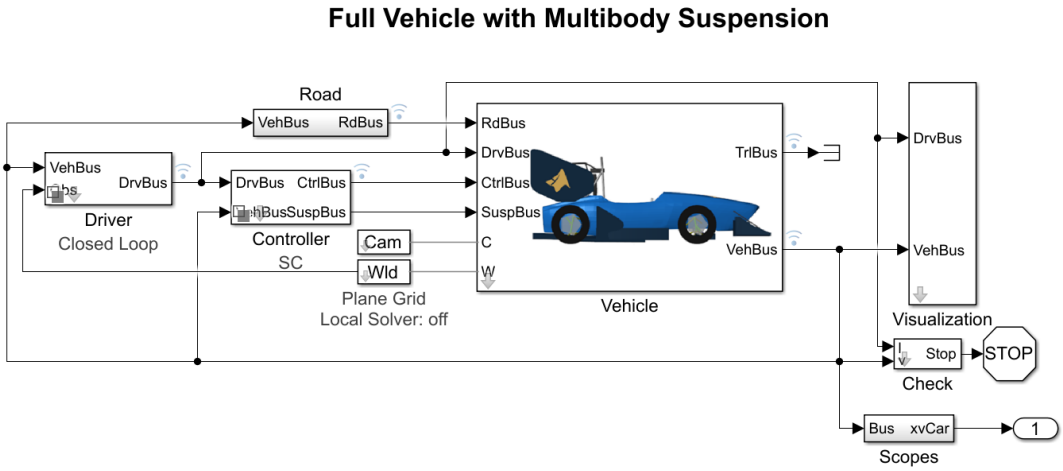

Figure 3.1: Full-vehicle model in Simscape

3.2 Controller

The controller is responsible for reading the driver's outputs, throttle pedal, brake pedal, and steering wheel, and for properly computing the torque request sent to the motors. Although the model also supports rear axle steering and automatic braking intervention, these features are not present in SC24.

Any control logic is written using Simulink, the model already includes two predefined control strategies: *Default* and *Torque Vectoring*. However, these will not be analyzed here, as they are not employed in SC24.

Two additional controller types have been integrated into the model: the *SC Controller* and the *Open-Loop Controller*. The former is the official controller used in SC24: a cascade controller composed of traction control, anti-lock braking system (ABS), launch control, torque vectoring, and the necessary estimators to determine the vehicle's state. It has been adapted to Simscape by removing low-voltage system checks and modifying the interface with the rest of the vehicle, since, clearly no CAN network is present in Simscape. The parameter interface has been kept unchanged, allowing for easy adjustment of control settings, such as maximum torque, maximum power, traction control activation, and more, as in the real SC24 system.

The second controller is used when an open-loop maneuver needs to be performed, replicating the exact same torque request with also reduced computational effort. In this mode, the driver's outputs are discarded by the control logic, while steering and brakes actuation remain under the driver's command.

Depending on simulation to be performed, one of the two can be chosen, also considering if controls need to be validated or not.

3.3 Driver

The model already contains two driver types, both described using Simulink and its libraries.

3.3.1 Open-Loop Driver

The *Open-Loop Driver* neglects any vehicle's outputs and will only receive three vectors as inputs: throttle, brake and steering. These inputs are directly linked to controls, brakes and steering wheel. These type of driver is used to simulate simple maneuvers as an acceleration event or to replicate exactly real-world maneuvers.

3.3.2 Closed-Loop Driver

The *Closed-Loop Driver* (Figure 3.2) on the contrary, is a control logic to maintain a certain vehicle trajectory at a defined speed. The observer of this driver compares the current vehicle pose and speed with the reference trajectory and speed of the imposed maneuver.

The driver is then composed by two controls, a lateral Stanley controller and a predictive longitudinal driver. The first is based on a kinematic or dynamic bicycle model, and computes the steering angle command to adjust the current pose to

match with the reference pose, using as input the current speed and direction. It is possible to modify a gain in order to manage its actuation and obtain the desired driver's behavior. The second uses the reference and current speed to generate throttle and brake commands. Citing Mathworks in [7]: "*the block implements an optimal single-point preview control model developed by C.C. MacAdam.[...] To implement the MacAdam model, the block represents the dynamics as a linear single track vehicle, minimizes the previewed error signal at a single point T* seconds ahead in time and accounts for the driver lag deriving from perceptual and neuromuscular mechanisms.*" It can be used to simulate complex maneuvers like Skidpad, Autocross and Endurance.

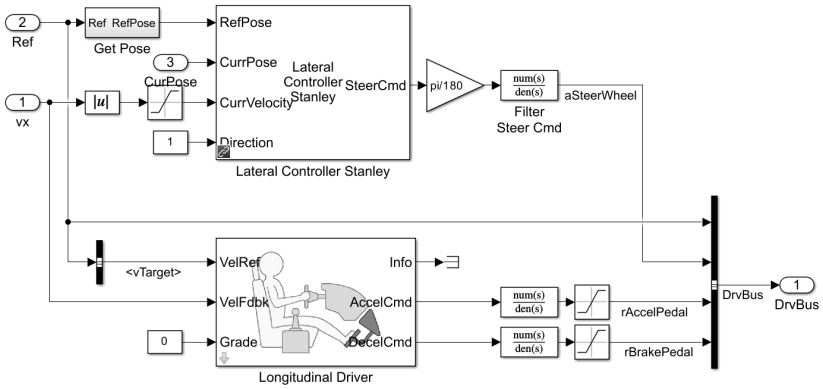

Figure 3.2: Closed-loop driver.

3.4 Vehicle

This subsystem represents the entire car, it reacts to inputs by controls and driver, every output is collected in the *Vehicle Bus*, it is possible to visualize also the car moving along its path using the vehicle outputs inside Unreal Engine ambient integrated in Simulink. It contains different subsystems with different Simscape physical domains.

3.4.1 Aerodynamics

The aerodynamics is modeled through a simple block that takes into account three parameters: the drag and lift coefficients multiplied by the reference area (CdA and ClA), and the position of the center of pressure. It is also possible to include the effect of wind, directly through a force, specified in the *Road Bus* input. The used aerodynamics parameters have been obtained through CFD, validated by wind tunnel testing in December 2023.

The vehicle speed, is then used in the computation of the longitudinal and vertical aerodynamic forces. In the end, forces are exchanged with the vehicle using the *External Force and Torque* Simscape block.

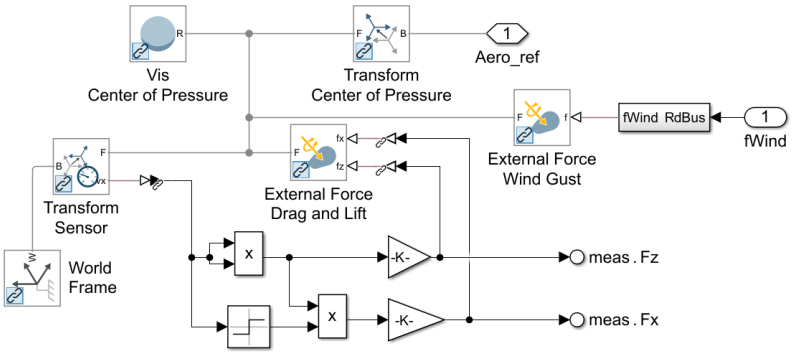

Figure 3.3: Aerodynamics block.

3.4.2 Brakes

The main block used is the *Disc Brake* from Simscape, which, as described in [8], models a brake consisting of a cylinder that applies pressure to one or more pads in contact with the shaft rotor. The *Disk Brake* block will apply the following formula:

$$T_{brake} = \frac{\mu_k p \pi D_b^2 R_m N}{4} \tag{3.1}$$

in which,

- T_{brake} is the brake torque.
- p is the applied brake pressure.
- N is the number of brake pads in disc brake assembly.
- μ_k is the disc pad-rotor coefficient of kinetic friction.
- D_b is the brake actuator bore diameter.
- R_m is the mean radius of brake pad force application on brake rotor.

Every coefficient is obtained by CAD and μ_k is obtained by brakes test bench.

As shown in Figure 3.4, the input signal, representing the brake pedal percentage, comes from the *Driver Bus*.

Since the front and rear brake pads and discs differ, the main challenge is to maintain the desired brake balance in terms of torque at the wheels. This requires converting the brake pedal percentage into the appropriate pressure ratio between front and rear circuits.

To achieve this, the maximum pressure corresponding to 100% pedal travel is defined for the front circuit.

Looking at logged data from SC24 race season, the maximum brake pressure applied is around 85 bar, this value will be used in the case of 100% percent brake pedal travel for both circuits.

Starting from Equation (3.2) in which *Brake Balance* is introduced, since it is an equation in two unknowns, the front pressure is fixed at 85 bar when 100% brake travel is occurring. Thus allowing to solve for rear pressure in combination with some mathematical passages in (3.3).

$$BrakeBalance = \frac{T_{brake,f}}{T_{brake,f} + T_{brake,r}} = \frac{a \cdot p_f}{a \cdot p_f + b \cdot p_r} \tag{3.2}$$

Where: a and b are the multiplication coefficients of the formula (3.1), without pressure p.

$$p_r = \frac{a \cdot 85 \cdot (1 - BrakeBalance)}{BrakeBalance \cdot b} \tag{3.3}$$

In the end, the brake pedal input is multiplied by the maximum pressure in the two different circuits, inside the *Actuator* block, obtaining in each braking the desired braking force and brake balance.

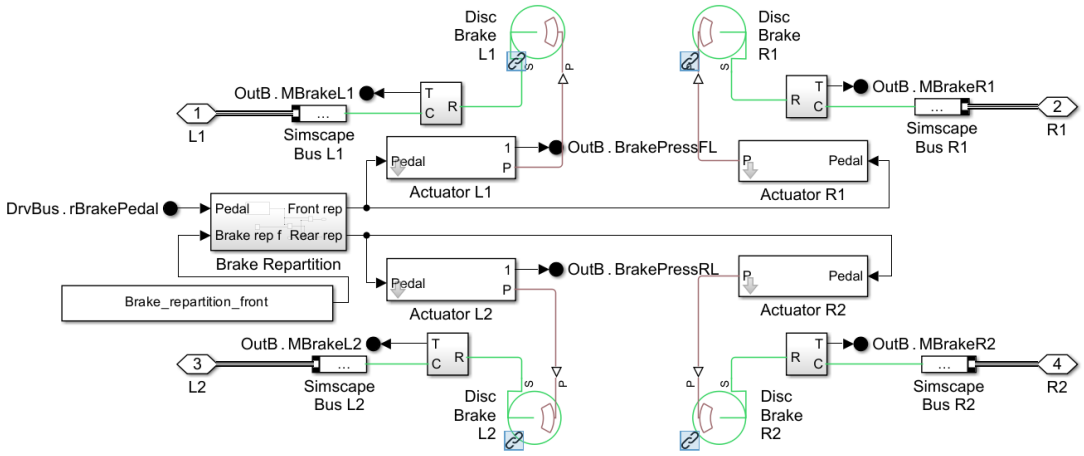

Figure 3.4: Brakes subsystem in Simscape.

3.4.3 Multi-body suspensions and steering

SC24, as previously mentioned, is equipped with double wishbone push-rod suspensions with on-board springs, dampers, and z-axis T-bar torsion bar as anti-roll bar. The push-rod arm is interposed between the upper wishbone and the rocker, which is positioned in the top part of the monocoque. Referring to Figures 3.5 and 3.6, the springs and dampers will then be positioned in a straight line aligned with the vehicle x-axis towards the rear of the car and, towards the front, it is possible to find the ARB droplink, the exact opposite construction is present at the rear.

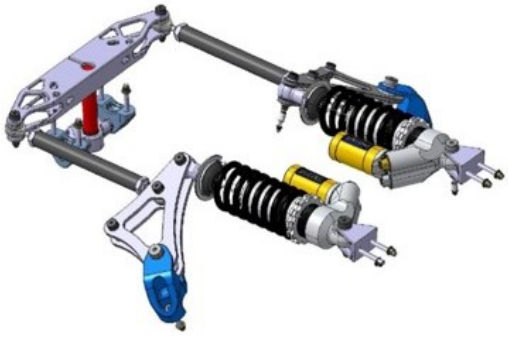

Figure 3.5: Front anti-roll bar and dampers.

Figure 3.6: Rear anti-roll bar and dampers.

Regarding the virtual reconstruction, also in this case, several suspension configurations for FSAE vehicle, are already at user disposal. Clearly, the choice is the *Double wishbone push-rod upper arm* (Figure 3.5) with steering in the front and no steering in the rear, since the possibility of rear steering is present, but that is not the SC24 case. The work done here is straight-forward since it is sufficient to change the hardpoints to adapt the suspension to the real one. Furthermore, for what concerns springs and dampers, their stiffness and damping have been inserted, with the only difference that now dampers are non-linear and the corresponding table has been added.

Regarding the anti-roll bar, the *Andromeda* layout, featuring a torsion bar along the z-axis, is not among the available options. Therefore, the *Droplink Rod* ARB has been chosen, even if it requires some modifications to match the rigidity and progressivity of the real system.

The *Droplink Rod* block models a U-bar ARB, where the torsion bar is horizontal and connects the left and right suspensions.

First of all, both the rockers attachment and the droplink length are kept the same as in the original design. However, the balancer now has double the length compared to the real one. This adjustment is necessary because, as shown in

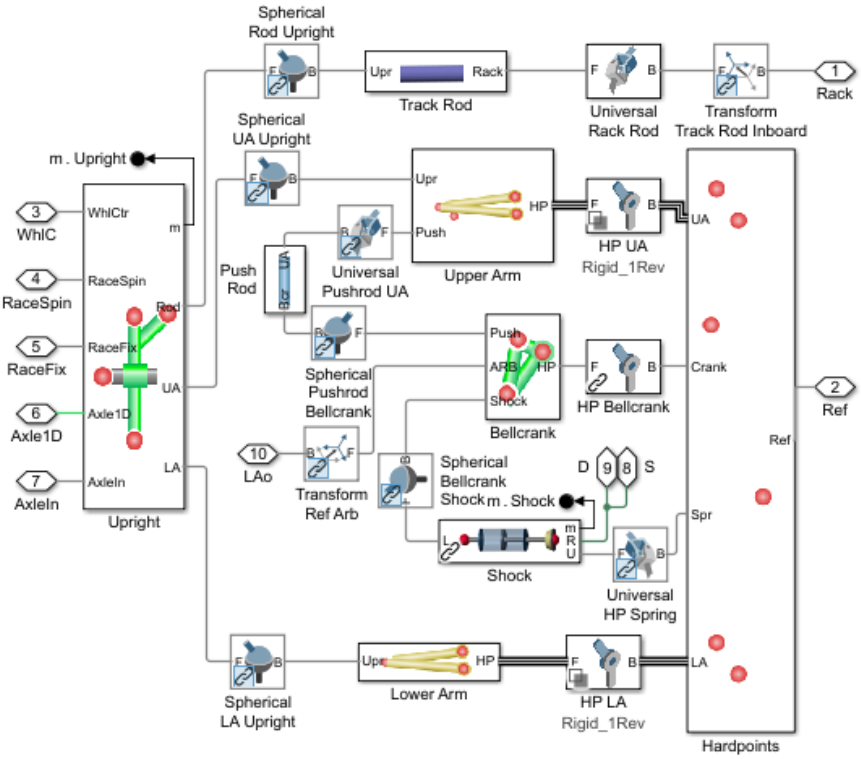

Figure 3.7: Simscape double wishbone push-rod upper arm subsystem.

Figure 3.9, in a T-bar layout one end is fixed to the chassis while the other twists by an angle α. In contrast, in a U-bar configuration, both ends twist by α in opposite directions, effectively resulting in a 2α torsion.

Following this reasoning, two strategies were considered: doubling the balancer length or halving the torsion bar stiffness. The first option has been adopted, as halving the stiffness would double the torsion angle progressivity compared to the original z-axis T-bar. The comparison of between T-bar modeled on Adams and U-bar modeled on Simscape are shown in Figure 3.10.

The results are shown in Figures 3.11 and 3.12, which display the graphical outputs of the Simscape Multi-body mechanical model.

With reference to steering instead, the *Wheel Driven Rack* subsystem has been used, it represents a double cardan joint steering with intermediate shaft. It is not originally present in the FSAE library, but it is accessible in other vehicles libraries. In Figure 3.13, the subsystem is represented.

In the end, since it is a multi-body model, it requires the mass of each component. An accurate CAD-based estimation has been performed, resulting in a Simscape input where each component is simplified as a cylinder, hollow cylinder, point mass,

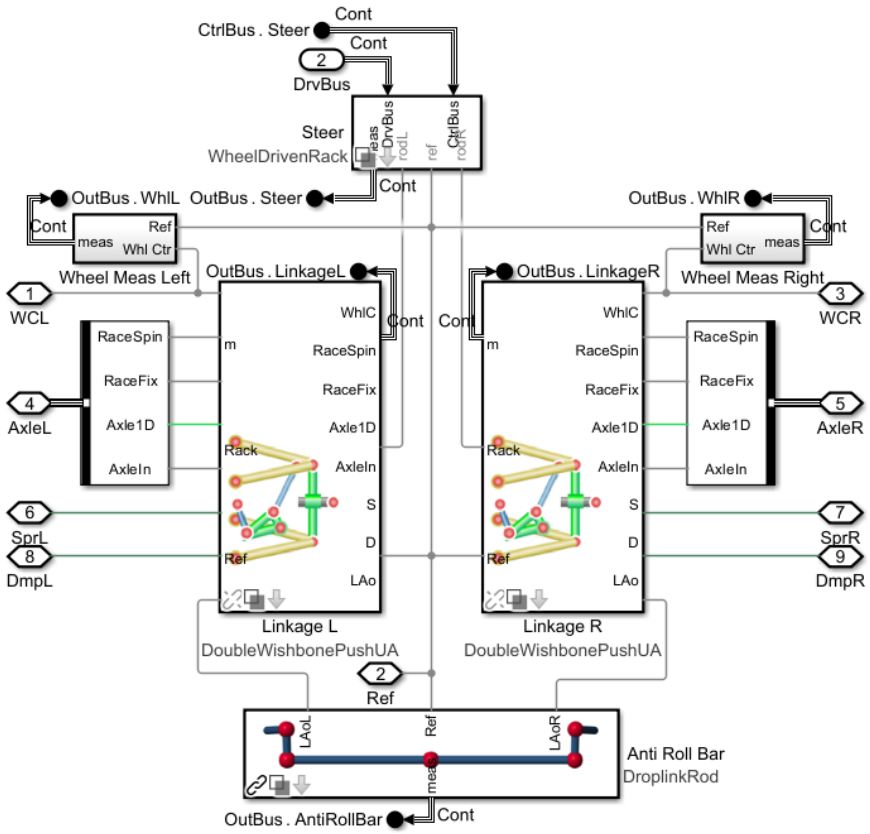

Figure 3.8: Simscape front suspensions subsystem.

etc., to estimate the inertia of each element.

As an example, the rocker schematization is shown in Figure 3.14: each arm is represented as a cylinder connecting the hardpoints. Each of them has the actual length and carries one third of the total bellcrank mass. Only the link to the droplink ARB has no assigned mass, as in reality it is located on the arm-pivot–shock absorber connection, and its mass is already accounted for.

For all components other than the suspension system, their mass has been included in the body, with inertia accurately estimated using CAD. Additionally, the body is assumed as completely rigid due to lack of test data and it links the four suspensions. The same process was applied to model the driver's mass and inertia.

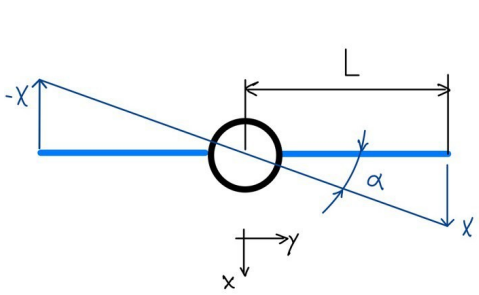

$$\alpha = \arctan\left(\frac{x}{L}\right)$$

(a) T-bar front view α angle calculation.

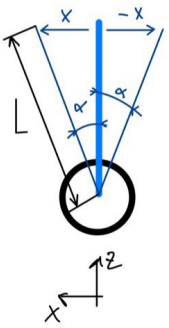

$$\alpha_{\text{tot}} = 2\alpha = 2\arctan\left(\frac{x}{L}\right)$$

(b) U-bar side view α angle calculation.

Figure 3.9: T-bar and U-bar demonstration, in black the torsion bar, in light blue the balancer in original position and in dark blue the balancer after an x movement.

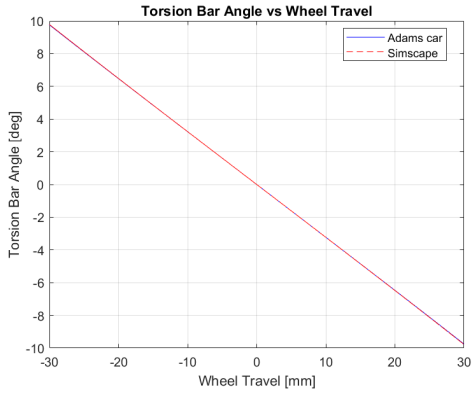

Torsion Bar Angle Front versus Wheel Travel.

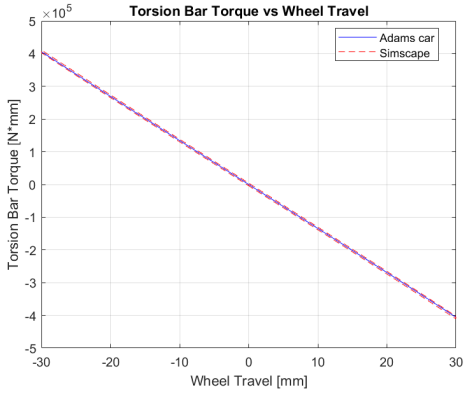

Torsion Bar Torque Front versus Wheel Travel.

Figure 3.10: T-bar Adams Car versus U-bar Simscape.

3.4.4 Tyres

The four tires are modeled using the Magic Formula Tire Force and Torque Simscape block (Figure 3.15), which, as described in [9], implements the steady-state combined slip Magic Formula model and can optionally take into consideration

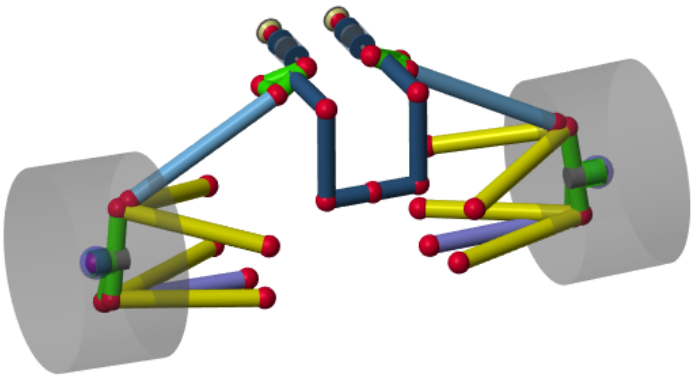

Figure 3.11: Simscape front suspensions.

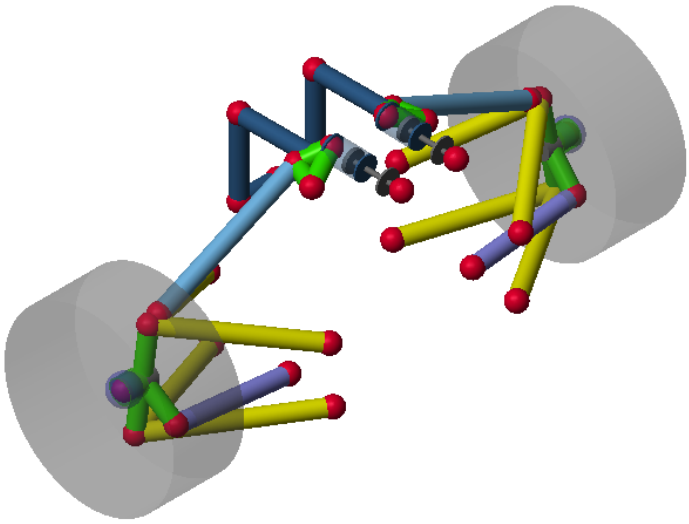

Figure 3.12: Simscape rear suspensions.

the turn slip effects. This block is responsible only for computing the tire forces and moments. As for suspension components, geometries, masses, and inertias, are instead modeled using Simscape solids.

The Magic Formula block receives input signals through port B, which is the connection with the road. Then, uses a .tir file, which has been properly scaled and validated with respect to the original data provided by the tire manufacturer,

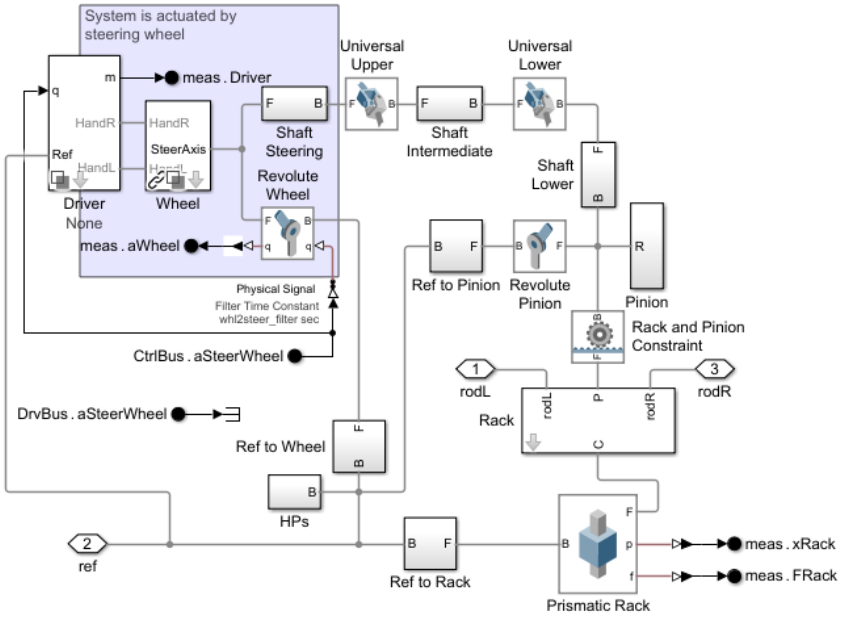

Figure 3.13: Steering subsystem in Simscape.

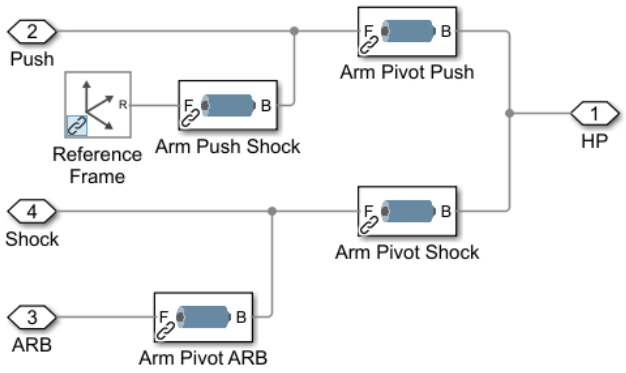

Figure 3.14: Rocker modelling on Simscape.

to output the corresponding forces and torques, in the port F which is linked to the wheel center. Moreover all the other ports on the right side are useful to log the data.

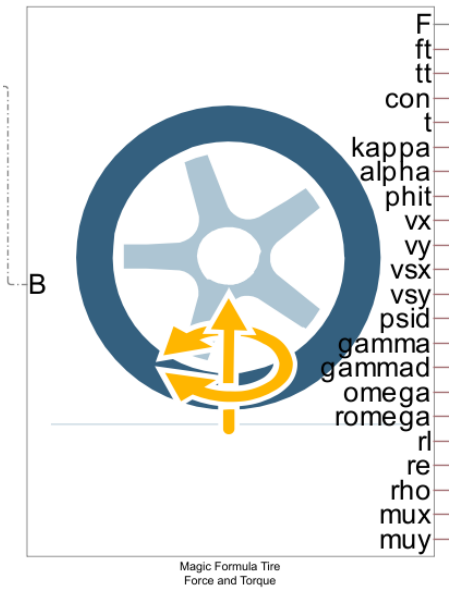

Figure 3.15: Magic formula Simscape block.

3.4.5 Battery

Passing to the powertrain side (Figure 3.16), the analysis begins with the battery pack (Figure 3.17). Since the real battery pack is composed of two parallel branches, this configuration has also been respected in the simulation environment by using two Simscape battery blocks.

The Simscape battery block, as described by MathWorks [10], is a high-fidelity model capable of calculating the open-circuit voltage as a function of the state of charge and, optionally, temperature, using lookup tables. It also provides several advanced modeling options to reflect the electrochemical behavior of the cells.

The cell parameters used in the model were obtained during summer 2024, thanks to dedicated testing performed by the Battery Pack Division of Squadra Corse, in collaboration with *Stellantis* and the *Battery Technology Center*. Two main tests were carried out to extract the required data. The first consisted of C-rate discharge tests at various temperatures, in order to characterize cell capacity as a function of discharge rate and temperature.

The second test aimed at generating an equivalent circuit model. It was based on pulse charge/discharge tests, which involve applying current pulses of known intensity and duration across a range of State-of-Charge (SoC) levels. This procedure allows calibration of the equivalent circuit elements at different SoC points, which are then interpolated using lookup tables. Since cell behavior is highly non-linear at high and low SoC levels, these regions are explored with shorter pulses and

a denser sampling of operating points. This test ultimately yields a state-space representation of the cell, enabling more accurate SoC estimation across its entire operating range.

In the simulation, the battery's positive and negative terminals are connected directly to the motors, differently from reality in which inverters are between battery and motors, while the thermal port is linked to the air-cooling system.

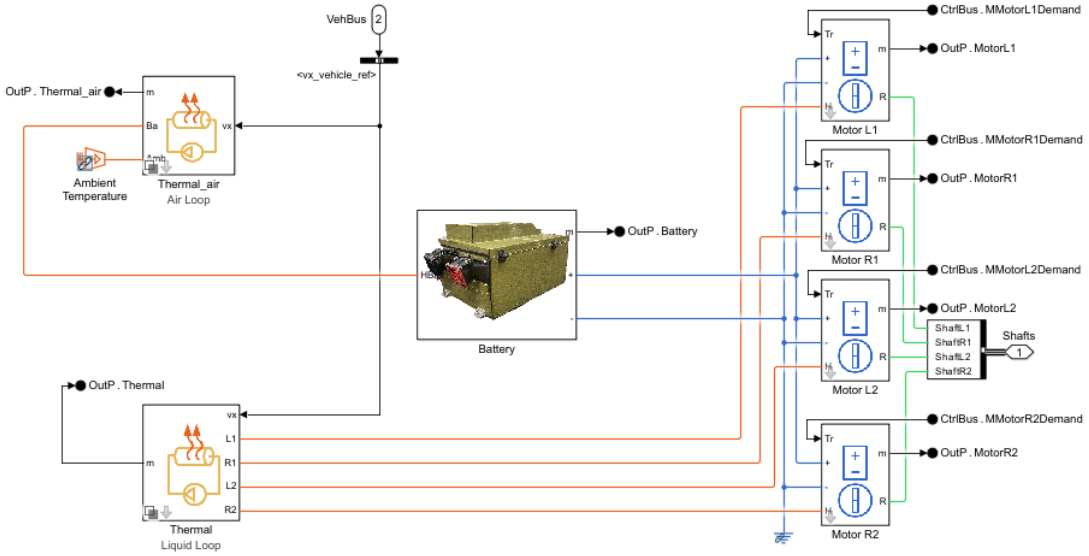

Figure 3.16: Simscape powertrain subsystem.

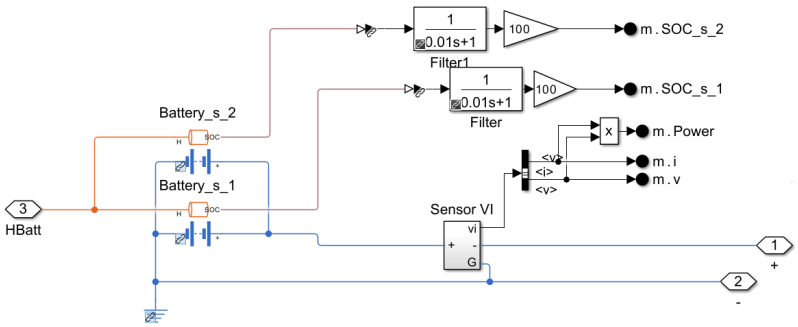

Figure 3.17: Simscape battery subsystem.

3.4.6 Motors

Four identical motor subsystems are present, each one using only the *Motor & Drive* block from Simscape. As described in [11], the *Motor & Drive* block represents a

generic motor and drive, or servomotor, with closed-loop torque control. Unlike in reality, inverters and the respective cooling plate are not included in the model. This is due both to the lack of available data for accurately modeling AMK inverters and to the limitations of the Simscape block, which does not support their inclusion.

Several connections are involved: the two battery poles, the thermal port (linked to the liquid cooling loop), the mechanical port (connected to the gearbox), and the main input, the torque request coming from the control system. Regarding the transmission, the Simscape block *Gearbox* has been used; the correct transmission ratio and meshing losses for the efficiency are the required parameters.

The motor maps are provided directly by the manufacturer, AMK. Three motor maps are available, corresponding to temperatures of 80 °C, 100 °C, and 120 °C.

To obtain the main torque map as a function of bus voltage and current, $T(V_{\mathrm{dc}}, i)$, the 80 °C map was used, as it reflects the most common operating temperature of the motor in SC24. For the temperature-efficiency map, instead, the one at 120 °C was selected, so that the Simscape block can interpolate efficiency data based on temperature.

3.4.7 Thermal management: liquid loop

Since, in the original model, even the battery was water-cooled, the entire cooling system has been completely redesigned. The liquid loop now cools only the motors, as the cold plate is not included, and the battery cooling system will be discussed in the next section.

Simscape Fluids offers a powerful and extensive library of useful components. Blocks such as heat exchangers, pumps, pipes, and others have been used extensively. Given the wide range of elements at disposal, Simulink modeling was practically not required.

Following the real-world configuration (Figure 3.18), the complete circuit is split into two parts, left and right, even the radiator is represented as two halves. The actual water routing sequence is: radiator, pump, quick disconnect, inverter cooling plate, front motor cooling jacket, rear motor cooling jacket, and finally back to the heat exchanger. The circuit is filled entirely with plain water.

In Simscape, the radiator is modeled using a *Heat Exchanger (G-TL)* block. On the gas side, the airflow produced by the fans is applied as a *Flow Rate Source (G)*, while on the liquid side, the water circuit connections are made. All parameters of the heat exchanger are given by the manufacturer. Following the circuit, a *Tank (TL)* block is included. Although no real tank exists in the physical system, it is necessary in the model to account for the approximately two liters of water in the loop. It also acts as the equivalent of a catch-can and is modeled as completely adiabatic. The pumps are modeled as ideal flow rate sources, capable of maintaining a constant mass flow rate (set by the input signal) regardless of pressure differential.

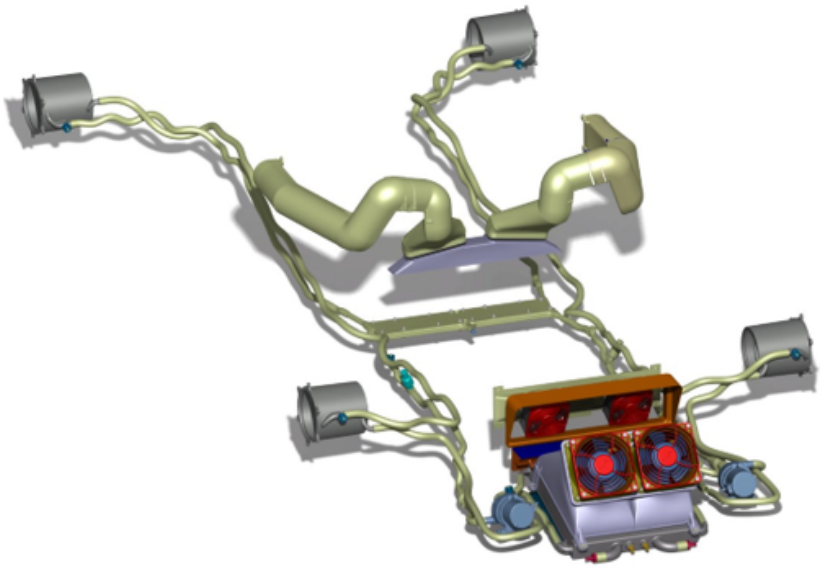

Figure 3.18: SC24 cooling system.

The block used is the *Flow Rate Source (TL)*. The quick disconnect, which is one of the elements with the highest pressure drop, is simply modeled as a flow restriction using the *Flow Resistance (TL)* block, with the pressure drop specified as a parameter. To model the motor cooling jackets, rectangular pipes are used to mimic the real water channels. The *Pipe (TL)* blocks model the pressure drops, while the heat exchange inside the motors is handled separately in the *Thermal Circuit Motor* subsystem.

The motor thermal model, illustrated in Figure 3.21, is quite detailed and includes windings, stator, and housing, with thermal conductances defined between these elements. The heat exchange between the motor case and the cooling fluid is modeled as a convective process. The corresponding convective heat transfer coefficient is determined as a function of the mass flow rate, based on CFD simulation results. In contrast, the other thermal conductances, due to the lack of specific manufacturer data, are estimated through the construction of a simplified thermal model.

Starting from an internal Squadra Corse study and thesis [12], which analyzes an AMK motor, the section view of the AMK motor (Figure 3.19) is used to extract the geometric dimensions as accurately as possible.

Assuming that the heat is primarily generated in the innermost part of the stator, a Lumped Parameter Thermal Network (LPTN) model is developed, following the approach described in Section 2.4.4. The model approximates three stages of radial conduction (Figure 3.20), with the outermost layer exchanging heat with

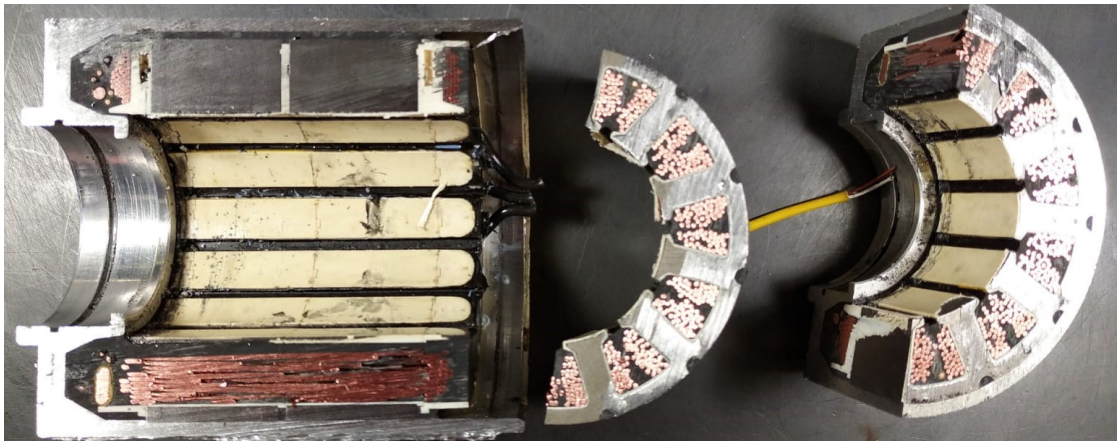

Figure 3.19: Section view of the AMK motor.

the coolant through convection.

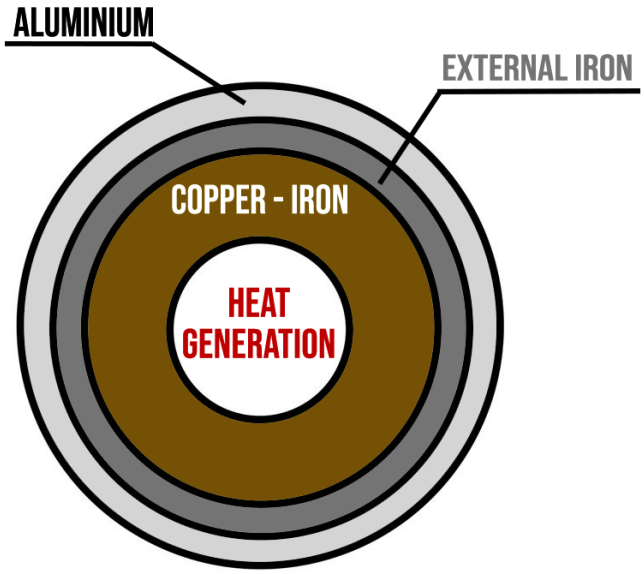

Figure 3.20: Thermal modeling concept: radial section of the motor.

The innermost region represents the windings. However, since the same radial section also includes iron, the effective thermal conductivity k and thermal mass are computed using a volume-weighted average. The relation for thermal conductivity is given by:

$$k = k_{\text{copper}} \frac{V_{\text{copper}}}{V_{\text{tot}}} + k_{\text{iron}} \frac{V_{\text{iron}}}{V_{\text{tot}}} \tag{3.4}$$

where V denotes the respective material volumes.

For the intermediate and outer regions, the modeling is more straight-forward, as each contains only one material: iron for the intermediate and aluminum alloy for the outermost layer. Their thermal properties, conductivity, mass, and geometry, are directly input into the Simscape components. The aluminum housing, finally, is in direct contact with the coolant and exchanges heat via convection using the CFD-derived coefficient.

Combining all these elements results in the complete thermal circuit shown in Figure 3.21.

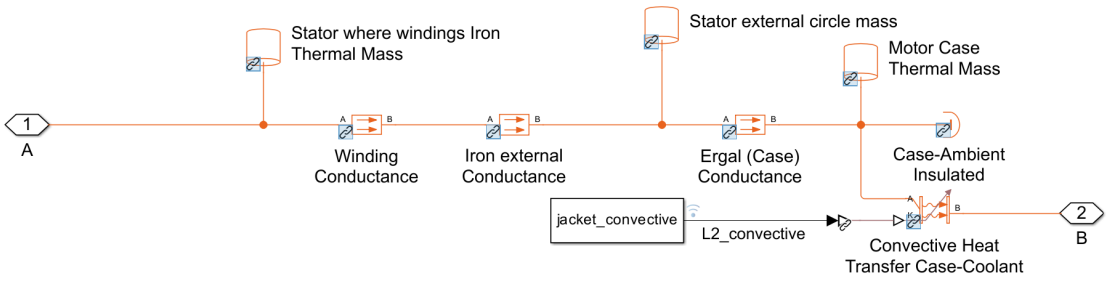

Figure 3.21: Thermal circuit motor subsystem.

Finally, the connecting pipes between components are also included. Since modeling the heat exchange of the long tubes running through the car would be excessively complex, they are assumed to be adiabatic.

3.4.8 Thermal management: air loop

This part is less complicated due to the simplicity of components involved. The air cooling (Figure 3.22) is made by two air channels, on both vehicle sides. While the car is running, they collect fresh air, which, through a dedicated channel, will invest the bus bars on top part of the battery pack.

Since there is no dedicated Simscape block for explicitly modeling the behavior of bus bars, the only block used is the *Convective Heat Transfer* block. The corresponding heat transfer coefficient is computed in a MATLAB function, based on the analytical correlations described in Section 2.3. The mathematical model, representing turbulent flow over a flat plate, implemented in Listing 3.1, is derived

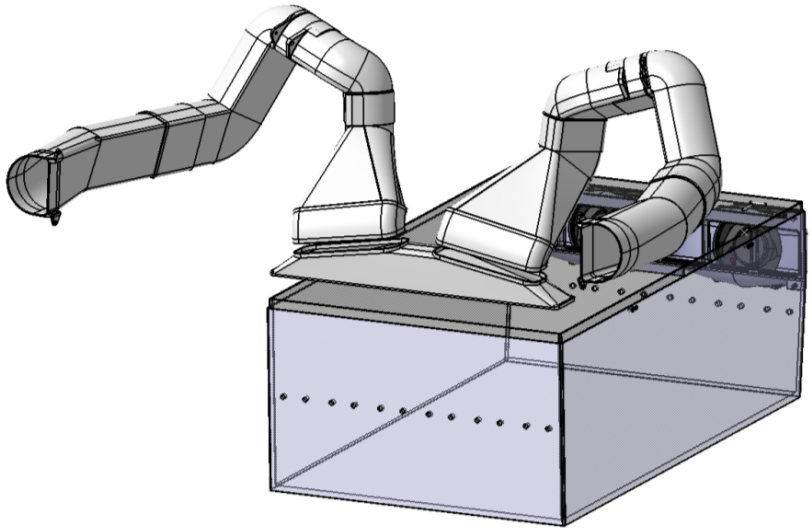

Figure 3.22: Battery pack cooling air conduits.

from the formulations proposed in [4], and accounts for two operating conditions. The former refers to running car, in which forced convection occurs due to the air flow generated by vehicle speed (represented in the code by: if vehicle speed >10 km/h). The latter refers to when the car is standstill and natural convection occurs with ambient temperature air (else condition in the code).

Listing 3.1: Convective heat transfer estimation

```
function h = fcn(T_batt, m_dot)

    rho = 1.185; % Air density
    A = 0.0495*0.0319*6; % Modulus air conduit section b*h*6
    (6 modulus)
    v = 15.5*10^-6; % Kinematic viscosity at 25 C
    alpha = 22.39*10^-6; % Thermal diffusivity at 25 C
    L = 568.7*10^-3; % Characteristic length battery pack
    k = 26.24*10^-3; % Thermal conductivity at 25 C

    if m_dot > 0.02 % Vehicle speed above 10 km/h
        u = m_dot/(rho*A);
        Re = u*L/v;
        Pr = v/alpha;
        C = 0.0296; % Turbolent flow over a flat plate
        m = 4/5;
        n = 1/3;
```

```
17          Nu = C*(Re^m)*(Pr^n);
18          h = Nu*k/L; % Convective heat transfer coefficient
19
20      else
21
22          T_film = (T_batt+300)/2; % 300K T ambient
23          beta = 1/T_film;
24          Ra = (9.81*beta*(T_batt-299)*(L^3))/(v*alpha);
25          Nu = 0.54*(Ra^(1/4));
26          h = Nu*k/L; % Convective heat transfer coefficient
27
28      end
29
30  end
```

Chapter 4

Validation

In this chapter, the thesis focus on the validation of the Simscape model comparing it with real-world logged data. Several standard maneuvers and Formula SAE events are taken into consideration to have the best possible comparison, analyzing all vehicle parameters and performances. Firstly, some subsystem validations are done for extra confidence and to exclude them from causes of mismatch with reality, other instruments different from logged data are used in this phase. Then, full-vehicle analysis will be conducted to evaluate the accuracy of the model.

4.1 Multi-body suspension kinematics validation

Suspension kinematics plays a crucial role in validating the overall vehicle model, serving as the foundation for proper suspension movement, vehicle handling, and correlation with real-world behavior.

The theoretical framework related to this part of the thesis is not directly presented in the previous sections, as the suspension theory developed in Daniel Carlino's master thesis [13] has been adopted as the main reference for the study of multi-body suspension systems.

MSC Software's Adams Car is a widely used multi-body dynamics software in the automotive industry, enabling the development of full-vehicle or subsystem models. It has been previously employed for modeling the SC24 front and rear suspension kinematics.

The validation approach consists of comparing the kinematic results obtained from Simscape with those from Adams Car. In Simscape, a half-car suspension model is implemented in a testrig configuration, where a vertical displacement is imposed on the wheel centers of the two tires. Simscape outputs are then logged and post-processed using MATLAB. A roll motion is selected for the half-car test to enable validation of the anti-roll bar (ARB) kinematics as well, as discussed in subsection 3.4.3, where the ARB model is further analyzed. All plots required for the validation of both front and rear suspension kinematics are available in Appendix A. Commenting on the results, all plots are very consistent with Adams Car, with only very small in scale differences; the only appreciable discrepancy is in the roll center vertical position. This behavior has been already noted by Carlino in his master thesis [13] and is due to different computation methods between Simscape and Adams Car. In Simscape, the roll center is defined as the intersection between the two *front view nLines*, which are the lines that link the contact patch and the center of the wheel *instant centers* of rotation.

Instead, in Adams Car, the roll center is calculated by introducing a unit vertical forces at the contact patch, oriented perpendicularly to the surface. These forces generate displacements at the tire-road contact points, which are observed both vertically and laterally from the front view. Subsequently, perpendicular lines are drawn from the displacement vectors at the left and right contact points. The intersection of these lines identifies the roll center. Conceptually, the roll center is represented as the location on the vehicle body where the suspension link forces, both lateral and vertical without creating any moment.

4.2 Steering validation

The steering kinematics, defined as the rotation angle of the tire with respect to the angle of the steering wheel, has been carried out differently. CAD kinematics is used as validated method and in Simscape a full-vehicle maneuver has been performed, the vehicle is still and the open loop driver is supposed to steer from -105 to 105 degrees.

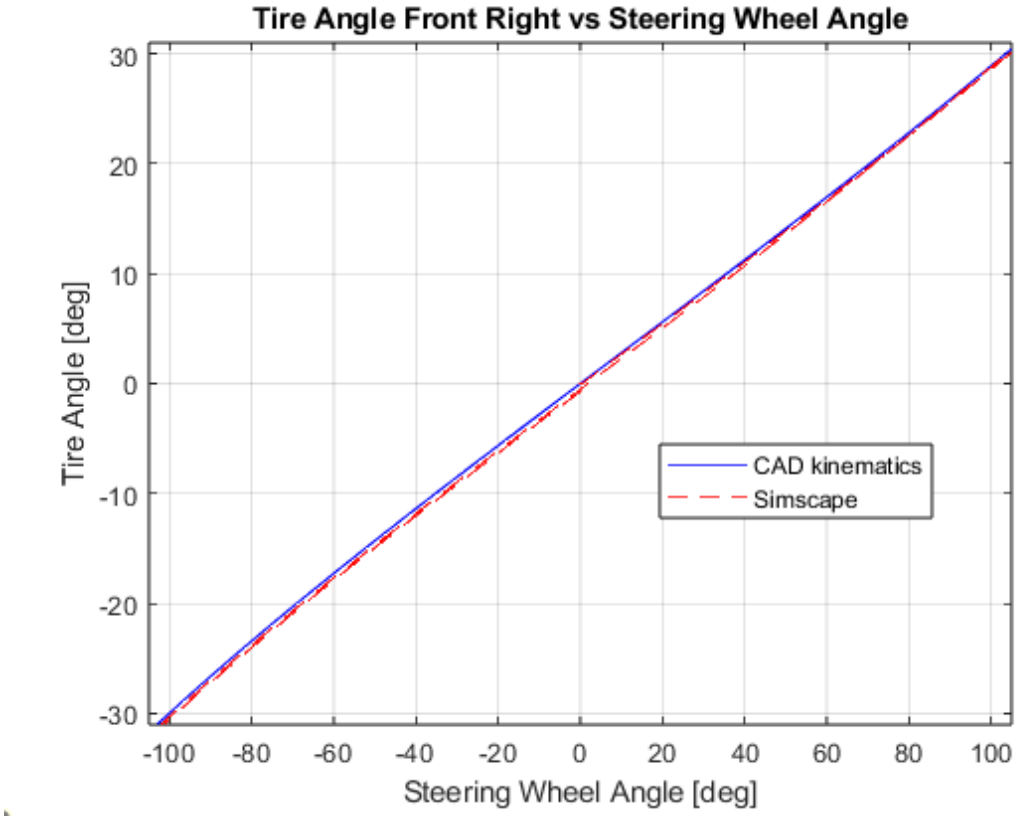

Figure 4.1: Tire angle front right vs steering wheel angle.

In this case, the discrepancies are more visible (Figure 4.1) , mainly because in CAD a single suspension is analyzed and without any load. As said, in Simscape a full-vehicle analysis is performed and it is important to consider, first of all the vehicle weight, and then, the load transfer caused by caster angle and kingpin inclination. In particular, these two suspension characteristics rise and fall the wheel with steer, rolling the car on the opposite direction with respect to steering and originate a diagonal weight shift. For example, in case of left steering, front left and rear right tires will receive higher loads, creating a tire compression that moves slightly the toe angle.

4.3 Acceleration

Regarding the acceleration event, in Simscape the *WOT braking* maneuver is chosen and its outputs are saved and compared in Matlab with logged data from one of the best acceleration test event during august 2024. To correctly compare the two maneuvers, since the simulation time is unknown, the open loop driver in Simscape is in charge of accelerate wide open throttle for four seconds, no steering nor braking are applied. The controls are set as in reality to have maximum fidelity; in particular, only launch control and power control are used.

Vehicle longitudinal performances and electrical validation are conducted, while, since the very short time, the thermal management part is not considered.

4.3.1 Results

The tested acceleration time is calculated by integrating the speed and obtaining a 75-meter distance, while in Simscape the precise distance is a simulation output, in that moment the time is registered. It is important to notice that this type of measurement is slightly different than real acceleration event, where the cars are positioned around 30 centimeters behind the point that starts registering the time. Since the objective is to make a comparison between logged data and Simscape, this factor is not taken into account, as it is only relevant for the absolute time.

	SC24	**Simscape**	**%Diff**
Time [s]	4.24	4.31	+1.6%
Maximum Speed [km/h]	106.29	107.64	+1.2%

Table 4.1: Acceleration SC24 vs Simscape.

As can be seen from Figure 4.2 and Table 4.1, the differences are quite small and totally in an accepted range for validation. Looking at torque and electric power, other considerations contribute to validate the model.

In particular, in Figure 4.3 shows that, in reality, the torque delivered by the rear motors is quite different from the request. This is because, in the control version utilized during august 2024, motor overloads are not considered and prevented. As reported in the AMK datasheet [14], the duration of maximum current operation is 1.24 s, but it is not reported how long the overload power reduction will last. Assuming a realistic window of 1.5/2 s, this acceleration phase is highlighted in yellow in Figure 4.3 and power part of Figure 4.4. Unfortunately, this behavior is not foreseeable, since no data are at Squadra Corse disposal and the overload procedure is entirely reserved by AMK low level control logic.

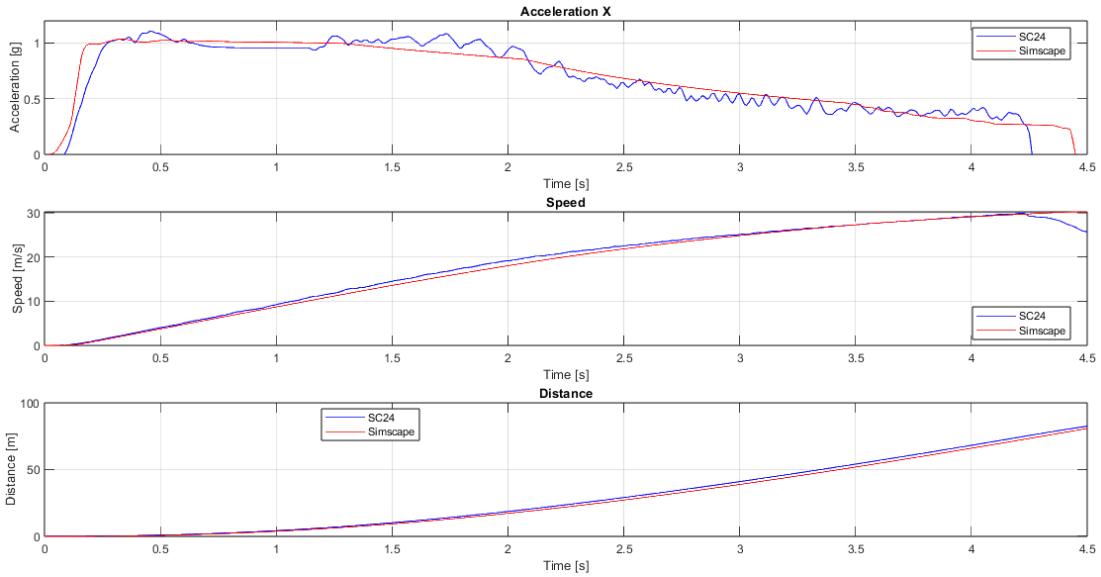

Figure 4.2: Acceleration longitudinal performances.

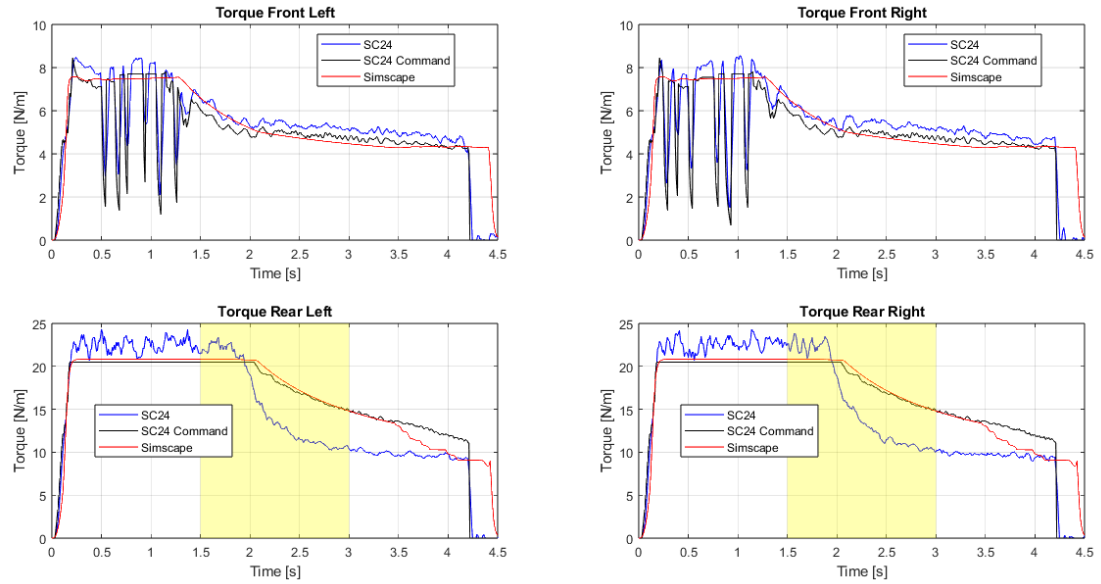

Figure 4.3: Motor torques during acceleration.

Furthermore, it is observable as SC24 delivers slightly more torque at rear tires than Simscape and despite launch control intermittent torque limiting it, can achieve slightly more acceleration and speed in the first acceleration half. While in the second half, SC24 front motors not affected by overload, produce more torque

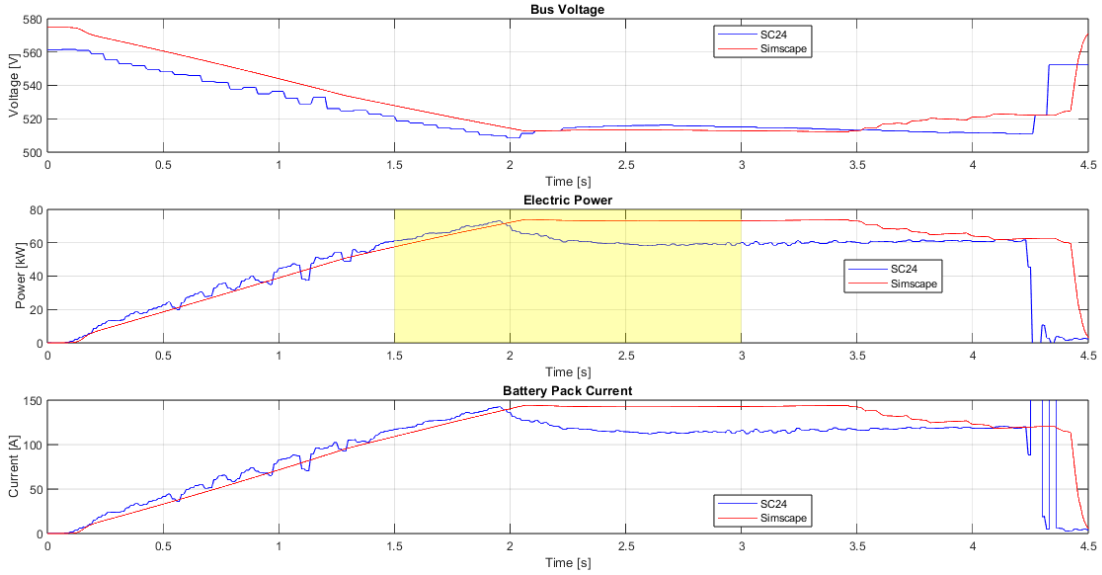

Figure 4.4: Battery behavior during acceleration.

than Simscape.

This summation of effects drives the two accelerations to have a very similar result despite some visible differences.

Finally, looking at Figure 4.4, some considerations at electric level can be done. Because of previous considerations, it is correct to see slightly more current and power during the first part of the acceleration.

4.4 Double-Lane Change

The double lane change (DLC) is a commonly used maneuver to evaluate a vehicle's handling and stability in sudden steering scenarios. Although ISO 3888-1:2018 defines the procedure and layout for passenger vehicles, applying the standard dimensions to SC24 test case would result in excessive entry speeds, increasing the likelihood of losing control. And so, during late season 2024 testing, due to constraints in track width and safety considerations, a modified, non-standard, course configuration was adopted to ensure the vehicle could perform the maneuver without exposing the driver to undue risk. The objective of this comparison is to validate lateral vehicle dynamics.

To reproduce the same exact maneuver in Simscape, an open-loop driver maneuver is performed taking driver inputs by SC24 logged data. Same setup as SC24 has been employed is Simscape. These tests were originally imprinted to evaluate how torque vectoring influences car performance, that is why the driver will always

apply 100% throttle and the speed is limited by power imposed at 10 kW. This will results in leaving out the driver from speed control. Since the aim of this thesis is to validate the vehicle model, in chosen maneuver, torque vectoring was not activated.

An important validation aspect of this maneuver is given by the presence of a vehicle side slip angle sensor mounted on the car for this particular test. Clearly, this makes vehicle side slip angle validation extremely reliable.

Also in this case, due to short time maneuver, the thermal management part is not analyzed, at the same time, since the power is limited, the electrical aspect is also neglected.

4.4.1 Results

Looking at absolute vehicle speed (Figure 4.5), knowing that the electric power is fixed, it is clear that in the case of slow accelerating maneuvers, the vehicle speed is different. In particular, the higher speed in Simscape case is probably affected by an underestimation of one or more friction factors. To further investigate this aspect, future coast-down maneuvers would be useful.

Instead, in terms of lateral acceleration (Figure 4.5), the model is quite consistent and gives good results, with slightly less acceleration after the first lane change.

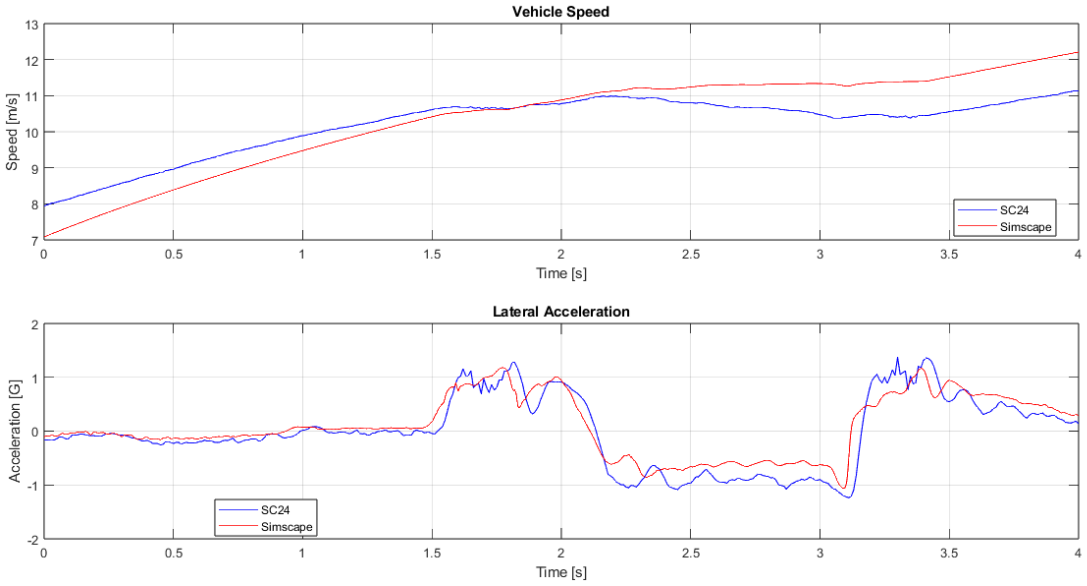

Figure 4.5: Vehicle speed and lateral acceleration in DLC.

The comparison of the vehicle side slip angle, shown in Figure 4.6, demonstrates

a satisfactory agreement between simulation and experimental data. The approximation is good overall, with only a minor offset observed. This discrepancy is likely attributable to not perfectly straight steering wheel in real life tests and the presence of sensor noise.

The understeer angle proves to be particularly valuable for validation purposes, as it provides a meaningful indication of differences in vehicle behavior during the maneuver. The understeer angle trends are closely aligned between the simulation and experimental results. Nevertheless, a small deviation is present, where the simulation exhibits slightly more understeer or, conversely, reduced oversteer. As discussed in Section 2.2.1, this parameter should not be interpreted as an absolute measure of understeer, but rather as a comparative indicator for dynamic behavior.

Finally, the yaw rate comparison also reveals a generally good correlation between the SC24 and Simscape models. A moderate discrepancy emerges in the latter part of the double-lane change maneuver, primarily due to the velocity gradient between the two datasets.

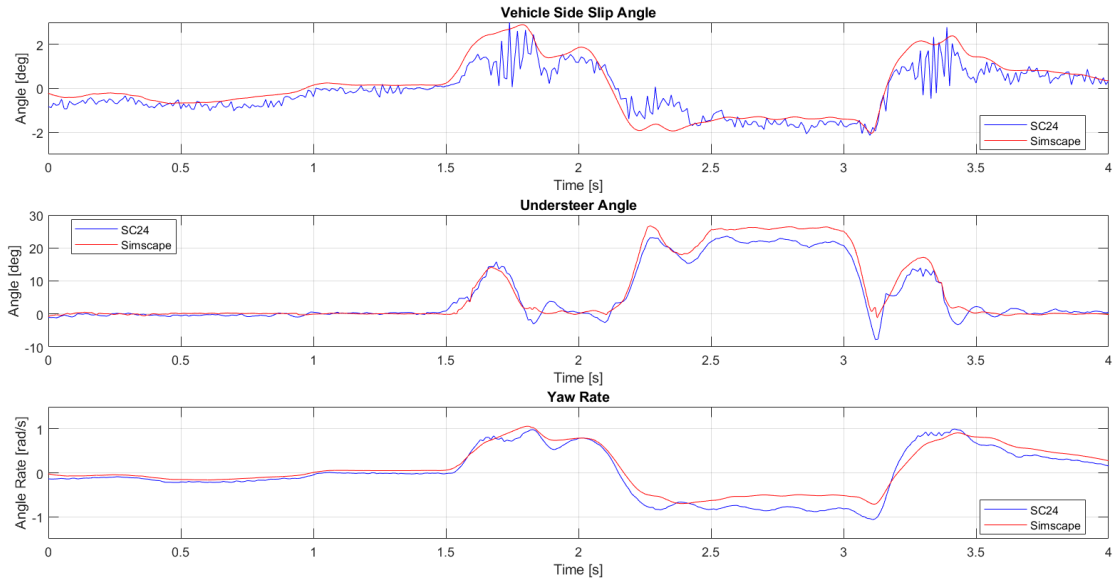

Figure 4.6: Vehicle side slip angle, understeer angle and yaw rate in DLC.

In the final Figure 4.7, a noticeable discrepancy in the vehicle trajectory is observed, particularly in the concluding phase of the maneuver. This deviation can be attributed to a combination of factors, including differences in vehicle speed, which also contribute to the mismatch in yaw rate, and the inaccuracy of the GPS measurements in SC24.

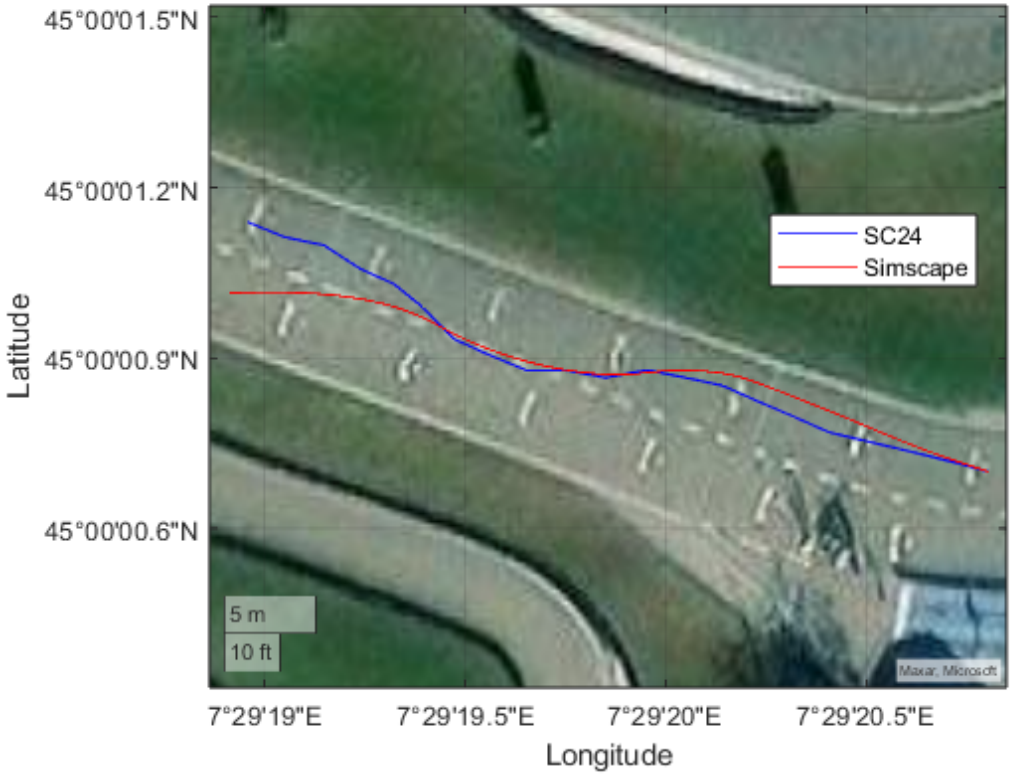

Figure 4.7: DLC trajectory.

4.5 Skidpad

The skidpad is the first closed-loop driver-controlled maneuver analyzed. As introduced in Section 1.1.3, the vehicle must follow a figure-eight shaped path, designed to evaluate lateral acceleration capabilities and overall vehicle balance. The SC24 reference maneuver corresponds to the best skidpad performance achieved by the SC24 car at Formula SAE Italy 2024, held in Varano de' Melegari.

In Simscape, the skidpad layout is already present and the closed-loop driver will try to follow a certain speed and trajectory imposed. The setup is the same as in reality and the same for controls that are setted as for the FSAE Italy skidpad. In this case, the driver adds a level of discrepancy and so, also its performance will be evaluated, in combination with controls analysis, especially torque vectoring. For the skidpad maneuver, thermal management can not be analyzed and the same for electrical part since only with the same speed profile it is significant.

It is important to remember that the controls are always remaining setted as in SC24, while the driver longitudinal and lateral coefficients are manipulated in order

to minimize the skidpad time. A parameters investigation has been conducted to find the driver's parameters to reach the objective.

4.5.1 Results

First of all, by examining the lap-time and lateral acceleration in Table 4.2, it can be inferred that the Simscape model exhibits approximately less lateral grip, or alternatively, that the simulated driver performance is inferior. Furthermore, it is important to note that the .tir file used for the tires (Section 3.4.4) was obtained during testing in October 2024, when the asphalt temperature was lower than that of the FSAE Italy skidpad. As a result, a slight reduction in grip is expected.

	SC24	**Simscape**	**%Diff**
Time right circle [s]	N/A	5.005	N/A
Time left circle [s]	N/A	5.008	N/A
Time [s]	4.868	5.007	+2.8%
Maximum lateral acceleration [G]	1.795	1.588	-11.5%

Table 4.2: Skidpad SC24 vs Simscape.

By analyzing the vehicle's overall performance, it can be observed in Figure 4.8 that the simulated behavior is quite close to the real one, reaching a good level of validation.

The behavior of the Simscape driver differs from that of the real-world driver, as shown in Figure 4.9. Throughout the simulated maneuver, the SC24 driver exhibits noticeable instability in throttle and steering control, which affects both longitudinal and lateral vehicle dynamics. In contrast, the Simscape driver, once it identifies a stable point, maintains consistent throttle and steering inputs throughout the entire maneuver.

This behavior is expected. The skidpad test is a demanding task, performed in a confined space and requiring high precision in steering. Once a controller reaches a point of equilibrium, it can outperform a human by applying consistent, optimized inputs. In this case, the Simscape driver behaves as an ideal controller, aiming to achieve steady-state lateral acceleration and constant speed. It reaches a stable condition that allows the control system to operate without significant transients.

Finally, the simulated driver uses a lower average steering angle compared to the real-world driver. Further analysis will be carried out using the understeer angle metric.

While the SC24 vehicle shows some torque fluctuations, particularly on the rear motors, the Simscape simulation presents similar oscillations, mainly due to torque vectoring actuation.

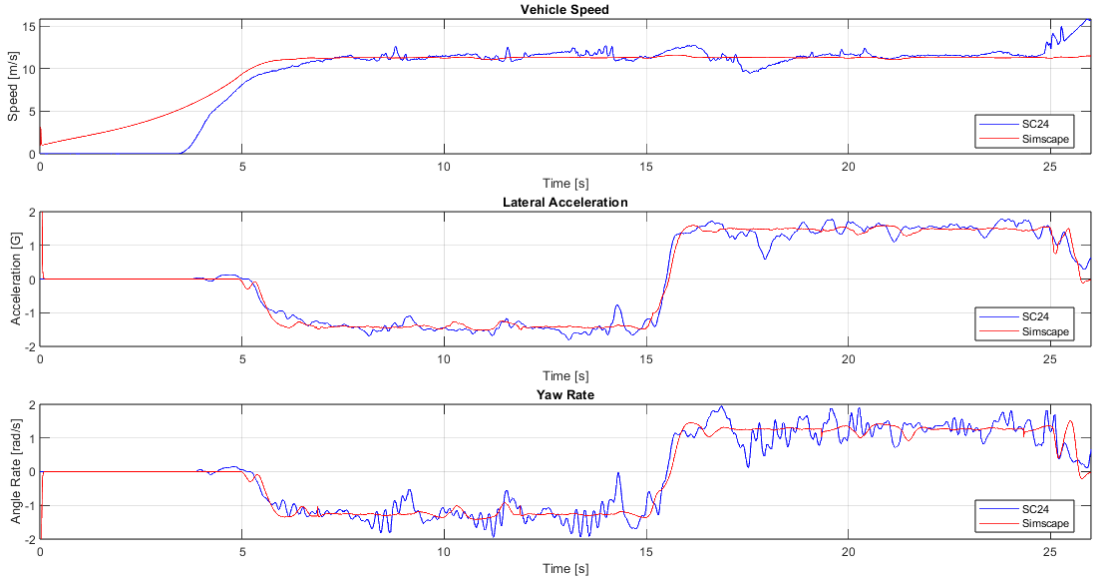

Figure 4.8: Skidpad Vehicle speed, lateral acceleration and yaw rate.

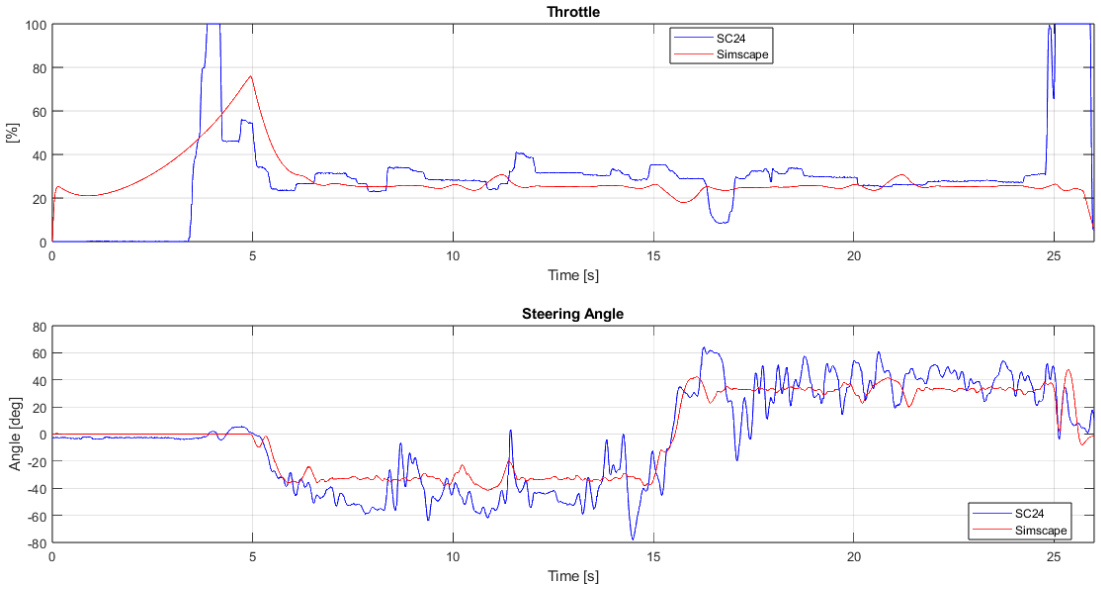

Figure 4.9: Skidpad driver outputs.

Concerning the understeer angle, it is evident that both vehicles exhibit some oscillations, greater in SC24 case. However, the mean value, calculated by averaging the data between 5 and 25 seconds, differs by approximately two degrees, showing good validation. This indicates a more oversteering behavior of the simulated vehicle, which helps explain why the Simscape driver applies less steering input

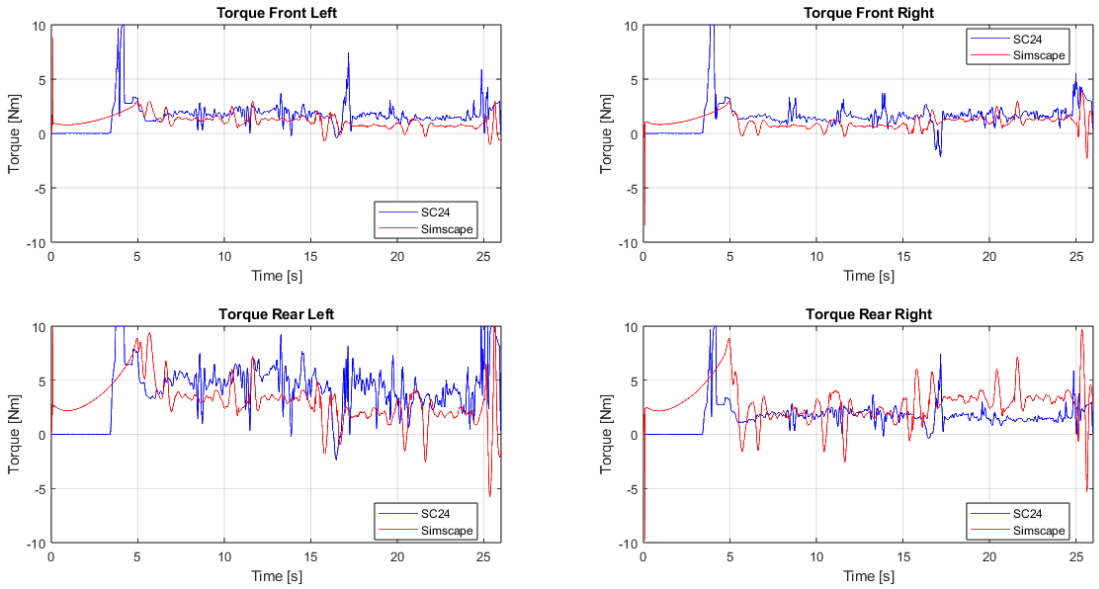

Figure 4.10: Skidpad torque request.

during the maneuver.

This result contrasts with what is observed during the DLC test (Figure 4.6), where the Simscape model shows a more understeering tendency. Nonetheless, this difference is entirely reasonable for two main reasons. Firstly, as already mentioned, the .tir file used for the Simscape model was generated at a different track temperature compared to the 2024 skidpad session. Secondly, torque vectoring was deactivated during the double lane change test, while it was enabled during the skidpad maneuver. Torque vectoring significantly influences vehicle rotation by applying a moment around the vertical (Z) axis. Ultimately, these two factors can strongly affect the overall vehicle balance and explain the differing behavior between the two tests.

Considering the vehicle's roll behavior (Figure 4.12), SC24 exhibits higher lateral acceleration, as previously mentioned, and a greater roll gradient compared to Simscape. The latter result is fully expected, since, as discussed earlier, the Simscape model does not account for chassis or suspension compliance. As a consequence, SC24 displays a larger roll angle per unit of lateral acceleration.

At the same time, SC24 data presents greater point dispersion, which is entirely reasonable when taking sensor noise into account. In contrast, Simscape appears more consistent, with minimal data spread.

Finally, the overall trend, obtained through linear interpolation of the data, suggests a slight asymmetry and an offset at zero lateral acceleration for SC24. However, this effect is mainly due to a few outliers and does not represent a

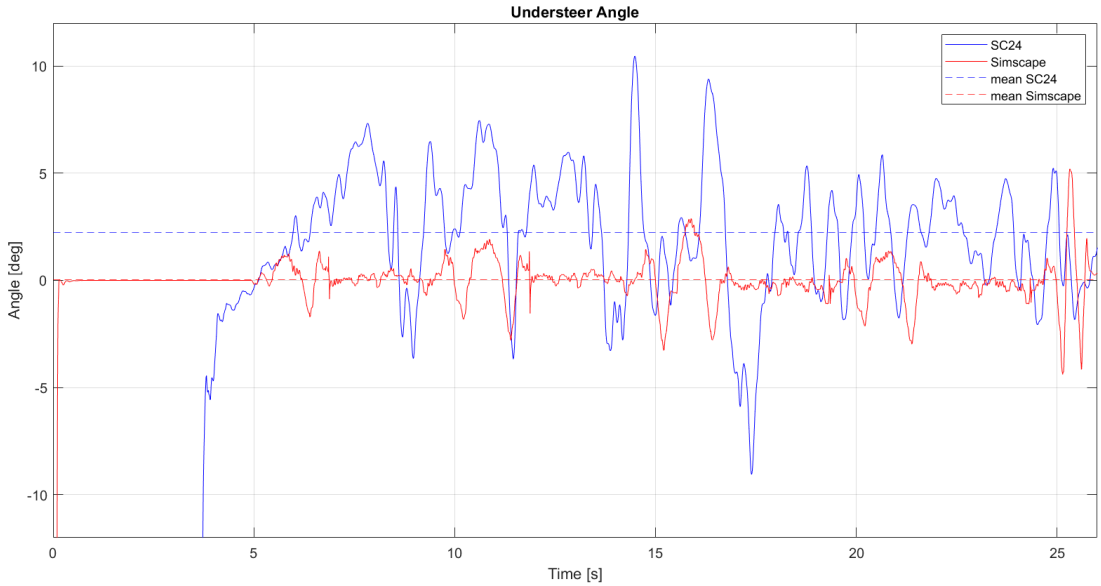

Figure 4.11: Understeer angle during skidpad.

systematic error.

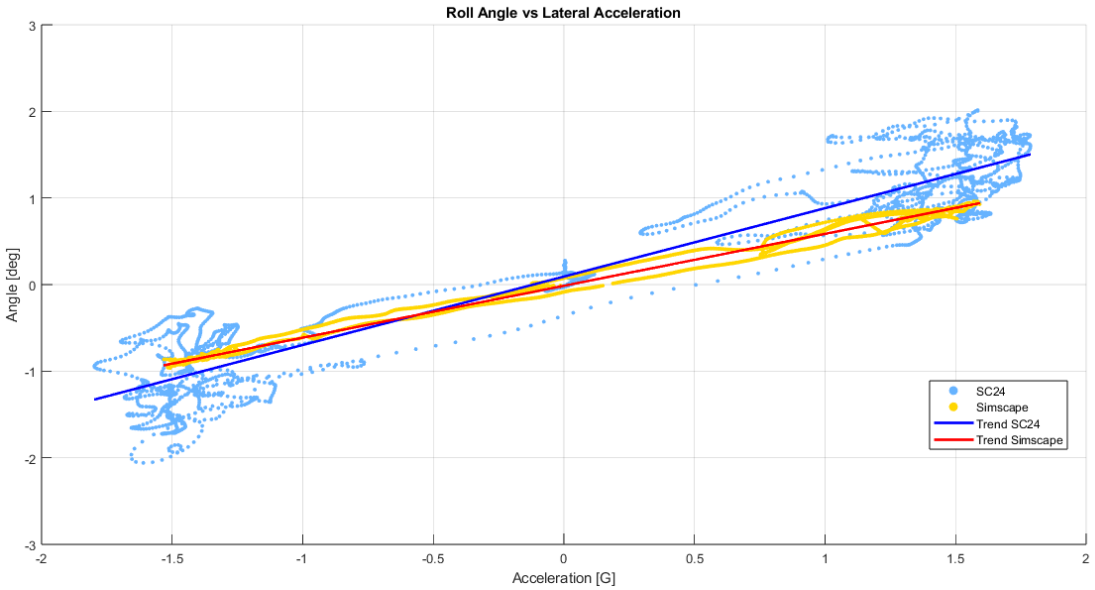

Figure 4.12: Roll angle vs lateral acceleration during skidpad.

4.6 Autocross

The autocross is the most challenging event for the driver, it is the qualify, and the lap must be completed as fast as possible with all the power available, having for great part of the lap cold tyres. This difficulty is reflected on Simscape driver, which has to drive in a very strict layout with fast changes in direction and speed.

The reference maneuver is the FSG 2024 autocross, the track has been completely replicated in Simscape, thanks to a MATLAB script that converts a track centerline into a reference trajectory, speed and yaw for the Simscape driver. This event will be driven by the closed-loop driver and an investigation regarding its parameters for lap time minimization will be performed. Car setup and controls parameters are exactly the same as in reality to have the best replication possible.

4.6.1 Results

In studying autocross results, the first aspect to highlight is that, even with the best possible closed-loop driver, after careful tuning of driver parameters, results in lap-time remains several seconds slower than the real vehicle. This implies that, while vehicle performance has proven to be fully comparable between simulation and reality, the same cannot be said for the drivers' performance. The SC24 driver is precise and able to adapt its behavior to each specific corner. This is not the case for the Simscape driver, which, despite occasionally leaving the track, is considerably slower. Several combinations of target speed and curvature parameters were tested, but none were able to replicate the real driver's behavior with acceptable accuracy and the obtained lap time is 109 seconds, compared to 88 seconds achieved by Andromeda at Hockenheim.

Looking at Figure 4.13, where various signals have been synchronized using the traveled distance to ensure alignment between simulation and experiment, it becomes evident that the Simscape driver lacks of top speed. This is due to the fact that higher target speeds imply higher speeds through corners, something the Simscape driver struggles to manage. This represents the first key source of discrepancy.

A more detailed view of a track sector is shown in Figure 4.14. Here, it appears that the Simscape driver tends to brake later and more aggressively. This is a consequence of the logic behind the driver model: if the vehicle is too far from the track centerline, the system reduces the target speed to the minimum value in an attempt to regain control. As a result, late braking leads to wider trajectories, requiring harder deceleration to bring the car back within track limits. The current driver model lacks anticipation in the braking zone, since the target speed is derived solely from curvature, thus preventing correct deceleration during straight segments. Although smoothing the target speed profile could help anticipate braking, it would

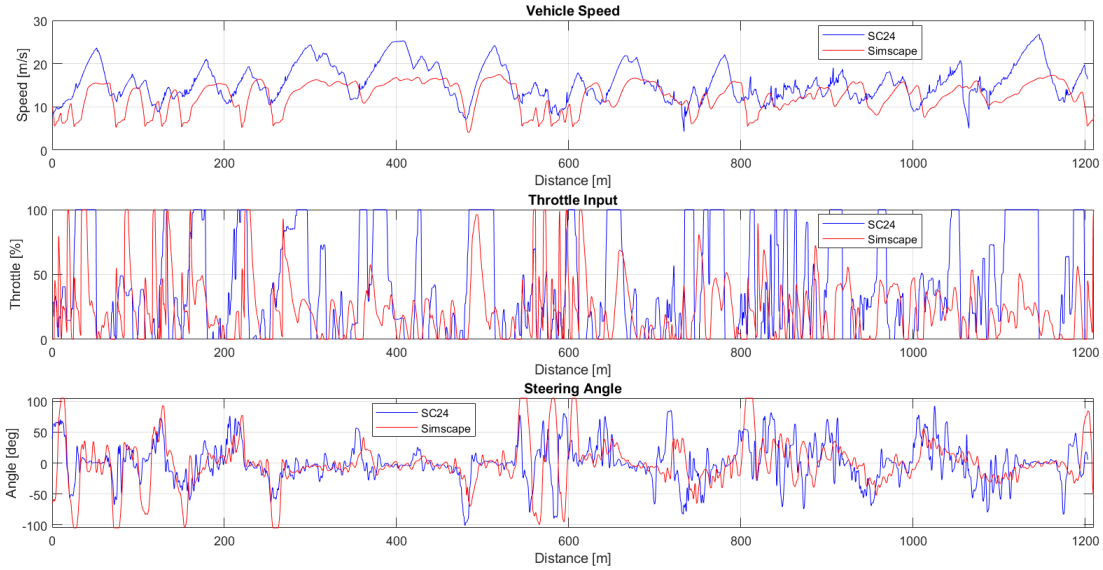

Figure 4.13: Vehicle speed, driver throttle and steering during autocross.

come at the cost of lost acceleration opportunities and excessive speed in tight corners, which would again result in increased lap times, especially on a stop-and-go layout typical of Formula Student circuits.

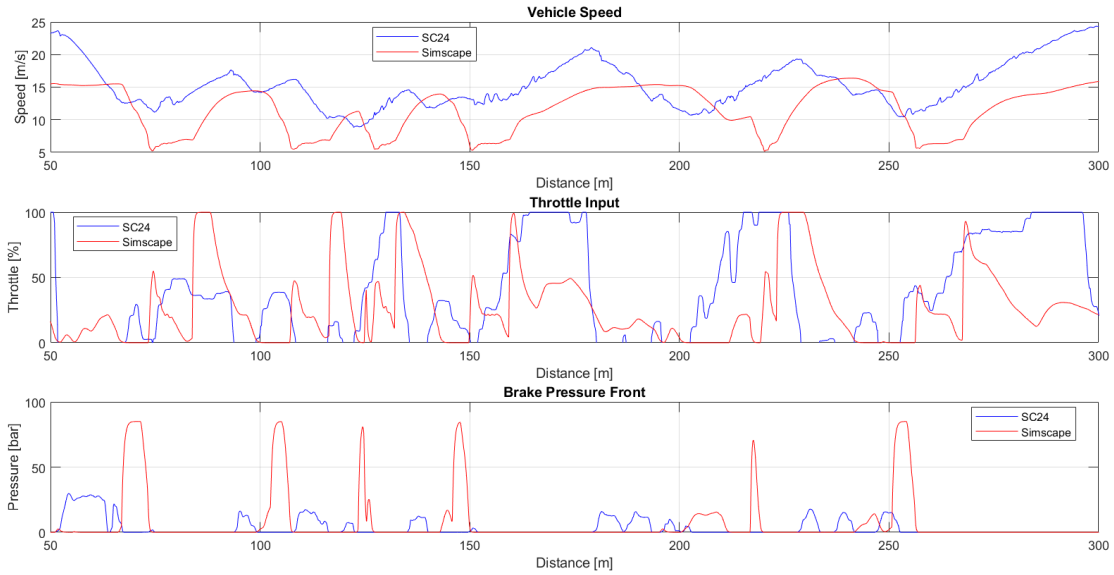

Figure 4.14: Vehicle speed, throttle and brake during a sector of the autocross track.

To further investigate the driving behavior, both GGV and GG plots are analyzed in Figures 4.15 and 4.16. From these plots, it is evident that the Simscape car is capable of achieving the same peak longitudinal and lateral accelerations. However, the density of combined acceleration points, both during braking and acceleration, is significantly lower than that of the SC24 driver. Additionally, the speed difference is clearly visible and directly comes from the previously discussed limitations of the closed-loop driver model.

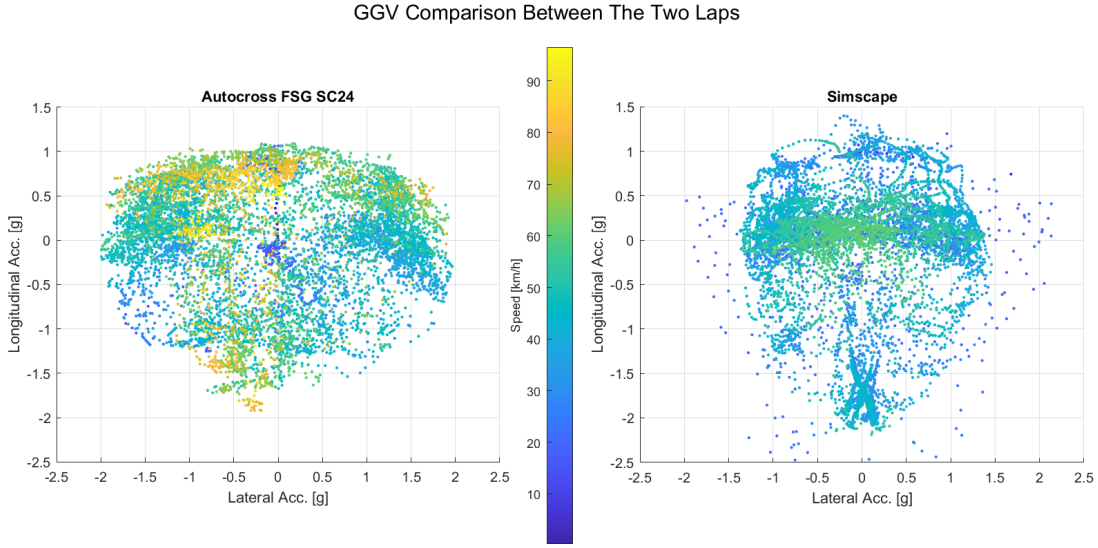

Figure 4.15: GGV plot during autocross.

In the end, it becomes evident that the current driver model is not suitable for handling a demanding driving cycle such as Formula Student's autocross. This part of the model clearly presents wide margins for improvement.

Following the analysis of vehicle dynamics and driver behavior, it is clear that powertrain and cooling results will not be directly comparable to real-world data. Nonetheless, these aspects are still reported and briefly discussed to assess the model's overall coherence.

Concerning the electrical subsystem, both power and current reach similar peak values (Figure 4.17); however, average values are consistently lower, as expected due to the reduced dynamic load. Voltage follows a similar trend: although the initial value differs, the voltage drops remain comparable whenever current levels between the two vehicles align.

Regarding thermal behavior (Figure 4.18), direct comparison with experimental data is particularly challenging due to the significant difference in energy consumption. However, using the *Thermal Load Index* introduced in Section 4.7.1, the

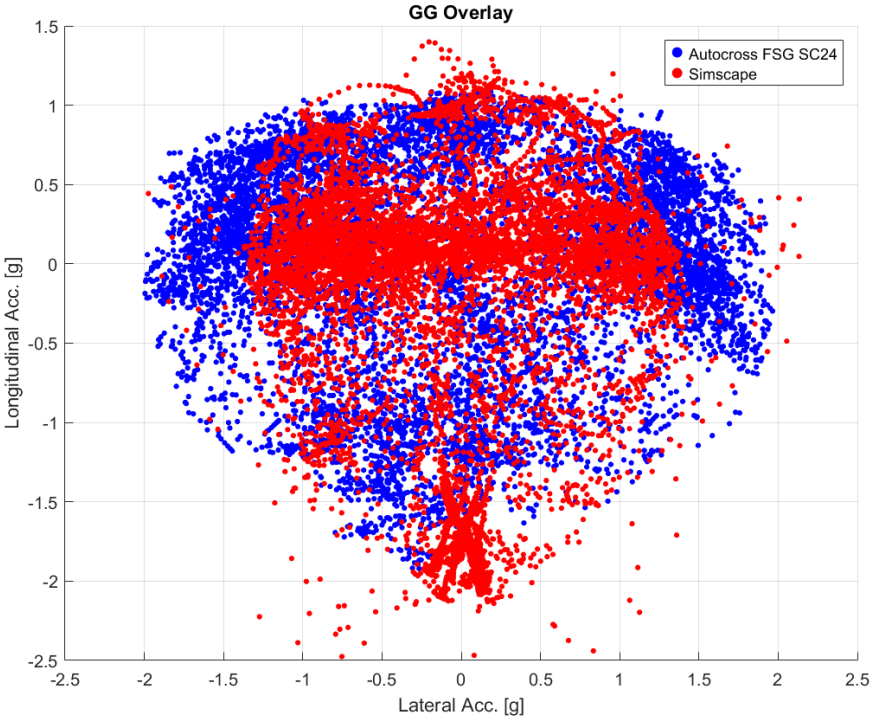

Figure 4.16: GG plot during autocross.

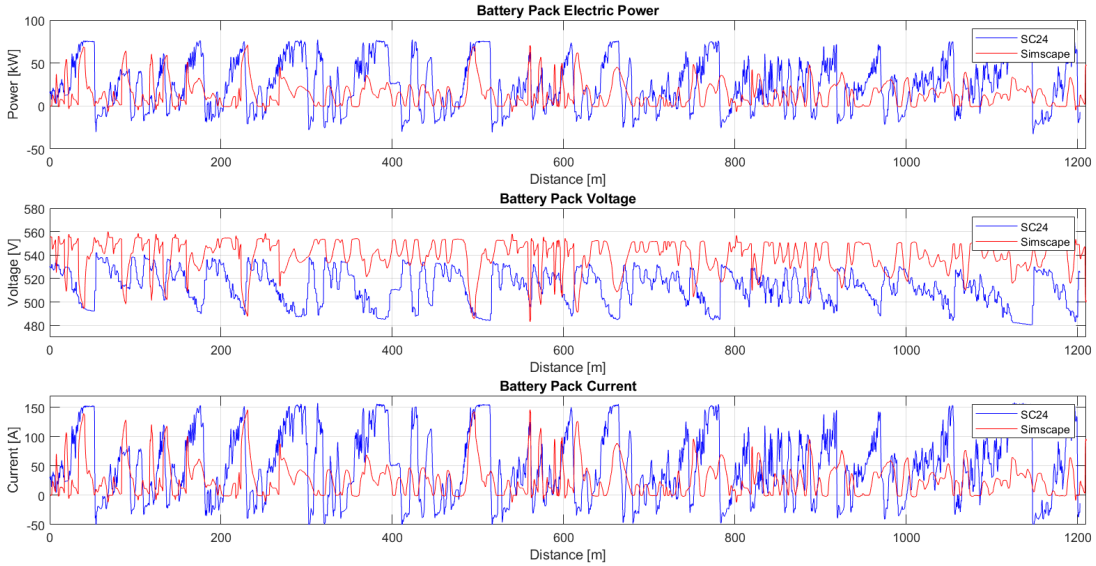

Figure 4.17: Battery pack behavior during autocross.

difference in TLI for motor temperature is quantified as 56.4%, while the deviation in TLI for average cell temperature is –15.4%. Although these differences are considerable, as expected given the lower energy usage, the results remain within a coherent range, in particular for what concerns battery pack, demonstrating the robustness and scalability of the thermal model.

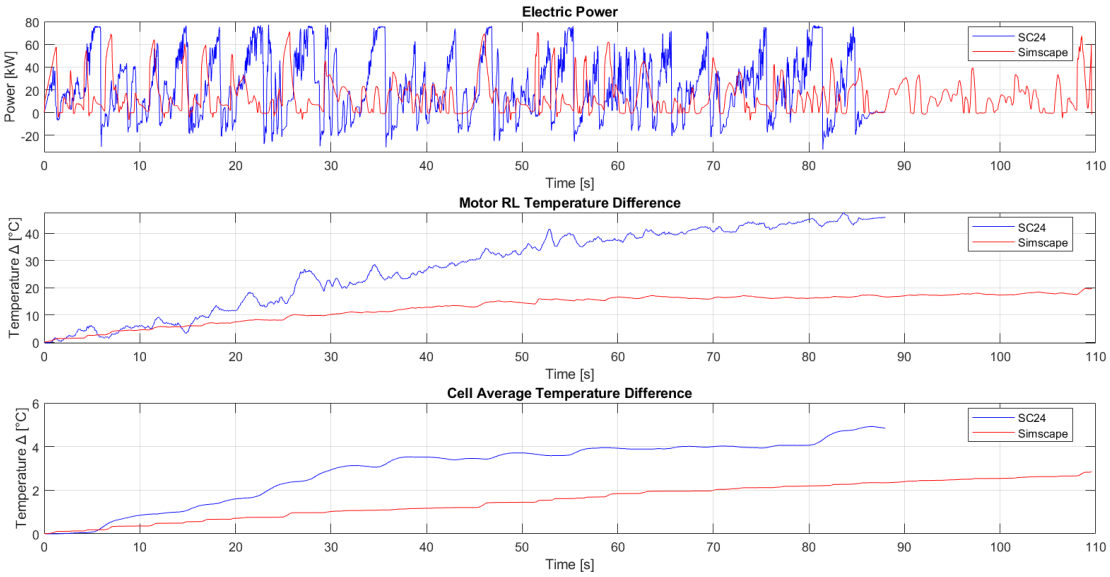

Figure 4.18: Thermal behavior during autocross.

4.7 Endurance

The endurance event is the most stressful for the vehicle and in particular for the powertrain, since 22 km are driven, challenging the energy, power and cooling dimensioning of the vehicle. Also the driver has to adapt his/her driving style, since, as said, the efficiency covers a great amount of points.

Since the driver behavior is not suitable to represent an entire endurance without risk of getting totally discordant results, and in order to obtain a very similar profile of speed and power, an open-loop driver with the same torque request as in reality is adopted. The objective is to validate everything apart from driver model and controls.

The reference maneuver for validation is an endurance simulation performed during the summer of 2024. Although the endurance event was not completed, due to a control system failure on lap 43 out of 48 that stopped the car, and regenerative braking exhibited some issues resulting in very limited energy recovery, the test remains representative of a typical endurance scenario. This is due to the

substantial driving distance covered at a consistent pace under realistic ambient temperature conditions.

Vehicle dynamics, powertrain, and thermal management analyses are carried out with the objective of validating these subsystems and achieving the thesis goal: developing a simulation tool capable of accurately modeling the entire vehicle under demanding operating conditions.

4.7.1 Vehicle Dynamics & Powertrain Results

In this section, vehicle dynamics and powertrain results are analyzed. These aspects are coupled in the following, as longitudinal performance is strongly linked to powertrain behavior.

The first aspect to observe in the power-time profile (Figure 4.19) is a clear discrepancy in the power demand, despite both vehicles requesting identical torques, as shown in the bottom row of Figure 4.19, and exhibiting similar speeds. This phenomenon had already been noticed during the DLC tests, and here it is further confirmed. Additionally, there is a persistent offset in vehicle speed throughout the simulation.

To better understand this discrepancy, an analysis of the efficiency from the battery pack output to the motor output has been conducted. Since the SC24 logs do not directly provide individual motor powers, the output power of all four motors was summed and then divided by the total battery pack power to estimate the average powertrain efficiency. The same method was applied to the Simscape simulation data. The resulting efficiency is defined as:

$$\eta = \frac{P_{\text{out}}}{P_{\text{in}}} = \frac{\sum_{i=1}^{4} T_i \cdot \omega_i}{P_{\text{batt}}} \tag{4.1}$$

However, the outcome is not fully satisfactory: as seen in Figure 4.19, the efficiency differs significantly between the two vehicles, probably due to conditions of low torque and temperature.

To address this issue, a constant scaling factor was introduced to account for unmodeled non-idealities and better align the simulated behavior with the experimental data. This correction allows for a more accurate representation of the observed differences. Specifically, the average efficiency values in the range $0.6 < \eta < 0.9$ during the first 150 seconds of the endurance test were computed for both SC24 and the Simscape model. The Simscape efficiency was then scaled to match the SC24 average, resulting in a correction factor of 0.88. The entire motor efficiency map was multiplied by this value.

After 600 seconds, the factor was recalculated and showed a slight improvement in the SC24 motors efficiency, showing a new scaling coefficient of 1.02. Nevertheless,

the original factor of 0.88 was retained, as it provides a satisfactory level of reliability over the entire endurance duration.

The resulting battery power output, shown in Figure 4.19, exhibits a much closer correlation with the measured data, demonstrating the effectiveness of the applied correction.

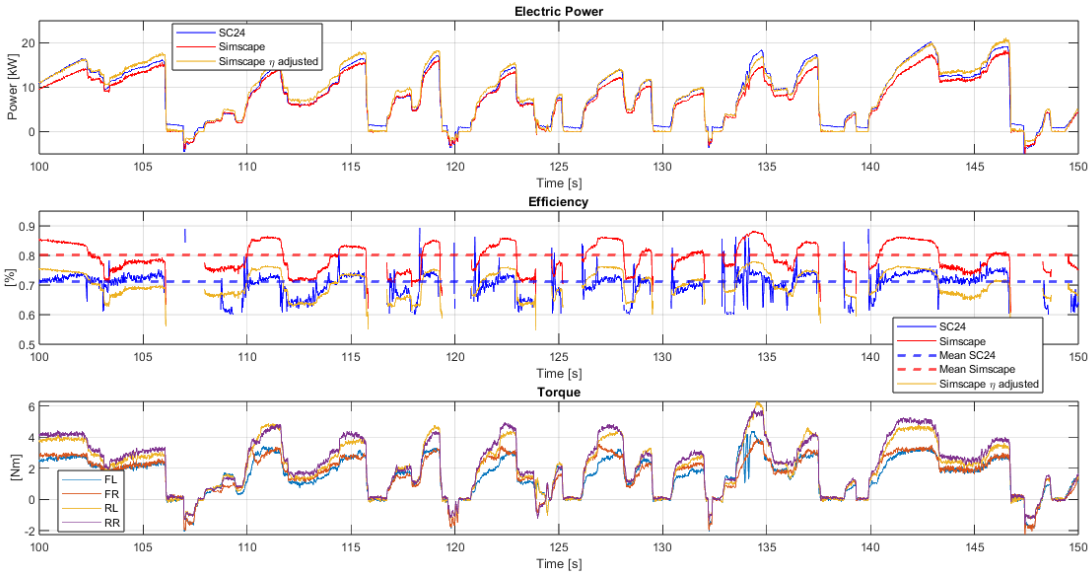

Figure 4.19: Power, efficiency and torques from both SC24 and Simscape.

Another significant observation concerns braking behavior. Despite applying the same brake pressure, the vehicle does not decelerate in the same manner as in the real case. This discrepancy becomes particularly evident when analyzing the vehicle's longitudinal acceleration in Figure 4.20. While some of the variation could be attributed to uncertainties in the coast-down phase, it is also apparent that the braking effectiveness in the simulation is lower than in the SC24 vehicle.

Given that the discrepancy is not pronounced during throttle lift-off (Figure 4.20), the attention is focused on the only tunable parameter that is likely to influence this behavior: the friction coefficient between the brake pads and the disc. An increment of 0.1 with respect to bench tested parameter is applied to perform an investigation.

This adjustment results in a more realistic braking response, with longitudinal acceleration more closely matching that of the SC24. However, due to the stronger deceleration, vehicle speed drops more rapidly, leading to a reduction in subsequent electric power demand. Based on the trend observed, a further increase of 0.1 in the friction coefficient would likely lead to an ideal match in braking behavior.

Nonetheless, to maintain a reasonable compromise with respect to power consumption, the friction coefficient is kept at the current level, i.e., +0.1 relative to the original value.

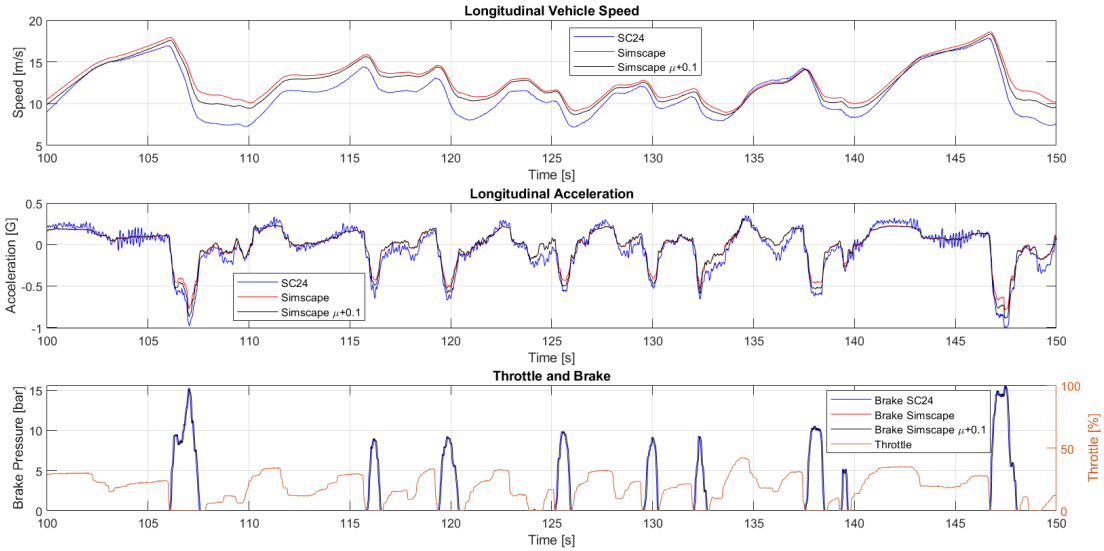

Figure 4.20: Vehicle speed, acceleration and driver pedals, original friction coefficient and adjusted.

In Figure 4.21, the AMK motor efficiency map is shown, with the working points of the rear left motor during the first 150 seconds of the endurance event plotted over it. Only this limited time frame was considered in order to avoid excessive data point density and preserve plot readability.

The map displays only the first quadrant, as no data are available for the others. The Simscape motor block reflects this top part onto the lower quadrants by changing the sign of current and torque. This representation allows for identifying the motor's operating region and evaluating energy performance, enabling a direct comparison between simulation and experimental data.

First, it can be observed that both SC24 and Simscape operate in the same region of the efficiency map. This is expected, given that the torque request is identical in both cases. Minor discrepancies may be attributed to differences in sampling frequency and slight variations in vehicle speed, as discussed previously.

Second, the most frequently used operating area does not correspond to regions of high efficiency. Moreover, significant efficiency variations are observed for small changes in torque. This sensitivity can contribute to noticeable differences between simulated and real-world energy consumption, as small errors in operating point estimation can lead to large deviations in efficiency evaluation. Additionally, it is

evident that at low torque levels, the motor operates with relatively low efficiency. This aspect should be considered in future energy optimization strategies, possibly by shifting operation toward higher torque values where the motor performs more efficiently.

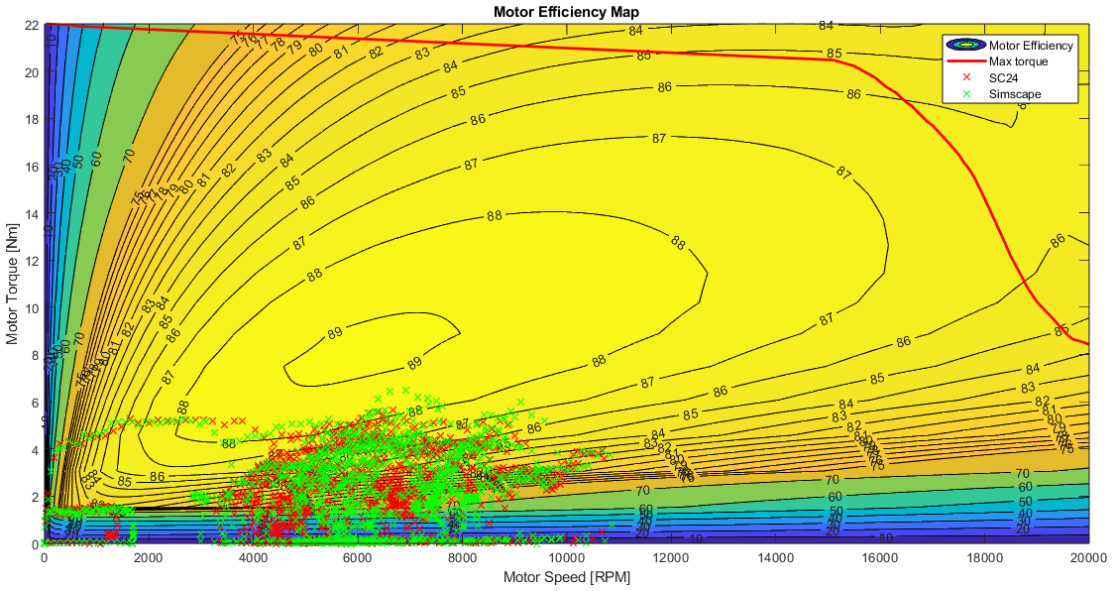

Figure 4.21: Motor efficiency with working points for rear left motor for the first 150 seconds of endurance.

Proceeding with the powertrain validation, energy consumption is now analyzed. Figure 4.22 illustrates that the simulated vehicle speed aligns well with the real-world data. However, there are brief moments in which the vehicle spins, causing the speed to drop to zero. These moments highlight the limitations of the vehicle dynamics model, which may not remain accurate under all driving conditions or styles.

This behavior does not appear to be strictly related to driving at the performance limit. For example, during the first stint, several spins occur repeatedly at the same point on the track, suggesting that the first driver executes a specific maneuver that the simulation is unable to replicate accurately. Conversely, in the second stint, the driver reaches higher speeds and spins the car in less predictable and less frequent ways, which are not confined to a single track location.

Despite these differences, the overall energy consumption remains consistent with the real vehicle, with noticeable discrepancies only during spin events. The same applies to regenerated energy: correlation errors occur primarily when there is a divergence in vehicle speed. As reported in Table 4.3, both energy consumption and regeneration differ by less than 6%, demonstrating a high level of accuracy

given the length of the driving mission and the fact that the simulated speed does not always perfectly match reality.

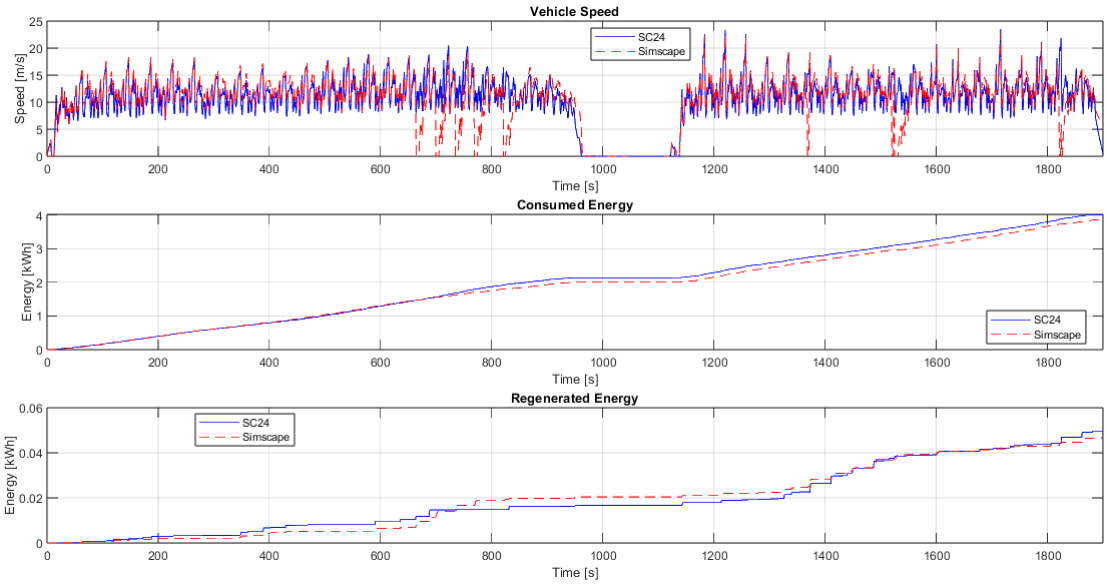

Figure 4.22: Vehicle speed, energy consumption and regeneration during endurance event.

	SC24	Simscape	%Diff
Consumed Energy [kWh]	4.022	3.858	-4.85%
Regenerated Energy [kWh]	0.046	0.049	-5.62%

Table 4.3: Endurance energy consumption SC24 vs Simscape.

The final aspect to analyze is the battery pack behavior. In Figure 4.23, the battery pack power, voltage, and current are presented. All simulation signals show good agreement with the SC24 experimental data, without significant discrepancies. The only notable difference concerns the voltage: in the experimental data, it is initially higher due to the simulation's initial conditions. However, both trends converge and follow a similar behavior throughout the mission, with SC24 exhibiting a slightly greater voltage drop. This can be attributed to two main factors. First, the Simscape model consumes slightly less energy, as previously discussed. Second, the state of health of the cells in the SC24 battery pack was reduced at the end of the 2024 season, resulting in lower available capacity. Both effects contribute to a more rapid voltage decrease in the experimental data.

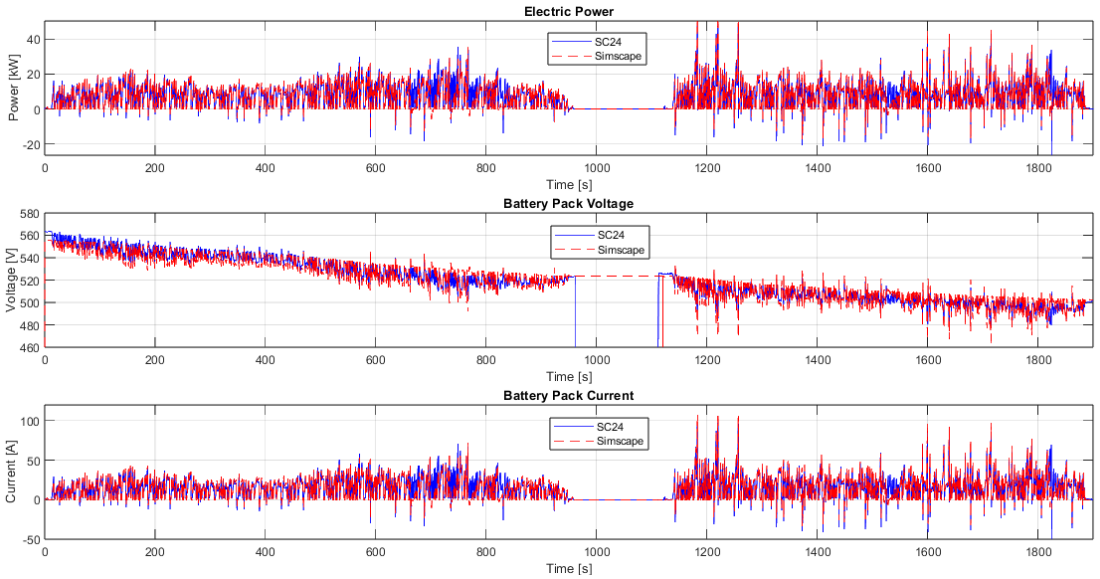

Figure 4.23: Battery pack power, voltage and current during the endurance.

4.7.2 Thermal Management Results

Moving on to the thermal management results, starting with the water-cooled circuit, motor temperature was compared between the two vehicles. The first iteration of the model validation reported unsatisfactory results and failed to meet expected values. Several possible causes for this discrepancy were considered. The most likely hypotheses include: the absence of an inverter cooling plate, missing pressure drop components in the circuit, an overestimated radiator efficiency, or an excessively high convective heat transfer coefficient in the motor's cooling jacket.

Since no experimental data are available for temperature inside the radiator, at other points of the cooling system, or regarding pressure losses, the analysis can only focus on motor temperature. The most significant parameter available for investigation is the convective heat transfer coefficient between the water circuit and the outer motor surface.

A sensitivity analysis was performed on this coefficient using a single motor temperature, the rear left, over the first 350 seconds of the endurance test (Figure 4.24), with the goal of improving system validation. This means that the selected coefficient is not necessarily the most accurate in absolute terms or the closest to reality, but rather the one that best reproduces the observed motor temperature behavior. This chosen value effectively accounts for all the non-idealities and simplifications that are not modeled within Simscape. The starting value is obtained by Computational Fluid Dynamics (CFD).

To account for the fact that the power delivered in simulation does not exactly

match the real endurance conditions, a normalization coefficient is introduced, referred to as the *Thermal Load Index* (TLI). It is defined as follows:

$$TLI = \frac{T_{final} - T_{start}}{mean(|Power|)} = \frac{\Delta T}{mean(|Power|)} \tag{4.2}$$

This coefficient, along with its percentage difference in simulation compared to the SC24 endurance case, is analyzed in Table 4.4 to evaluate the most appropriate convective heat transfer coefficient (CC).

In the first column, the CFD-derived CC values is scaled by various factors. These factors were not chosen according to a predefined sequence; rather, each value was selected iteratively based on the outcome of the previous simulation.

CC	ΔT **[K] @150s**	**TLI @150s**	**%Diff @150s**	ΔT **[K] @350s**	**TLI @350s**	**%Diff @350s**
SC24	17.62	0.0027	0	26.44	0.0036	0
CFD	6.29	0.0013	-49.18	N/A	N/A	N/A
CFD · 0.50	17.15	0.0027	+5.52	18.08	0.0025	-23.07
CFD · 0.45	18.08	0.0029	+11.18	19.78	0.0027	-23.07
CFD · 0.35	20.45	0.0033	+25.81	23.66	0.0033	-7.91
CFD · 0.30	21.98	0.0035	+35.23	26.51	0.0037	+3.14
CFD · 0.25	23.81	0.0038	+46.33	30.42	0.0042	+18.22

Table 4.4: Sensibility analysis of motor cooling jacket heat transfer coefficient.

In order to better understand the effect of this coefficient, two points are analyzed, after the first 150 and 350 seconds of endurance. In fact, the most accurate result for 150 seconds seems to be CFD · 0.50, but it is clear that is not reliable at 350 seconds. Instead, CFD · 0.30 is the best one after 350 seconds, but it does not represent correctly the situation after the first seconds in which a transient is present.

The found coefficient is quite unrealistic considering the starting CFD-derived value, but as said, it encloses all the other not considered non-idealities not only inside the cooling jacket but in the whole circuit.

At this stage, the motor temperature behavior over the entire endurance event can be analyzed, using as convective coefficient the one previously derived, scaled by a factor of 0.30 by CFD.

Figure 4.25 shows that the temperature evolution is generally consistent with experimental data, and the model reliably captures the thermal dynamics, except for the previously discussed time intervals where vehicle speed shows significant discrepancies (Figure 4.22).

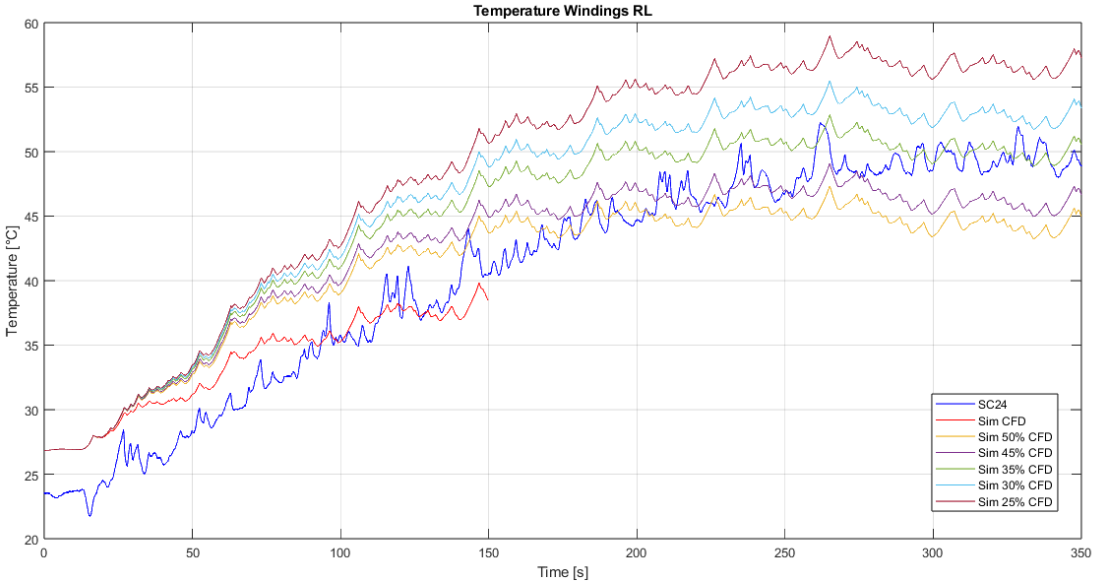

Figure 4.24: Temperature behavior during the first 350 seconds of endurance, convective coefficient sensitivity analysis.

Additionally, the error between the simulated and experimental temperature rise (ΔT) is plotted. The root mean square (RMS) error is calculated to be 6.23 °C, and the coefficient of determination (R^2) is 0.68. These two metrics indicate a high level of accuracy, especially considering the assumptions made, the model inputs, and the local mismatches in vehicle speed.

A similar analysis has been performed for all four motors, as shown in Figure 4.26. The thermal behavior is consistent across all motors, confirming the reliability of the model, even for the front motors, which generally operate at lower torque and thus lower power levels compared to the rear ones. The main noticeable difference is the initial temperature offset among the motors in the SC24 data, which is likely due to sensor offset errors rather than actual thermal divergence.

The final aspect to analyze is the battery pack temperature. The temperature rise relative to the starting point is computed and compared between SC24 and Simscape, as shown in Figure 4.27. The main discrepancies appear during the second stint. At the beginning of this phase, the experimental data show a sudden drop in temperature, which stabilizes to a realistic value after a few seconds. This behavior may be attributed to sudden car movement and consequent fresh air over temperature sensors.

A second, more relevant difference is observed throughout much of the second stint, where the simulated temperature increases more rapidly than the experimental one. This mismatch may rise from three primary factors: (i) local discrepancies in

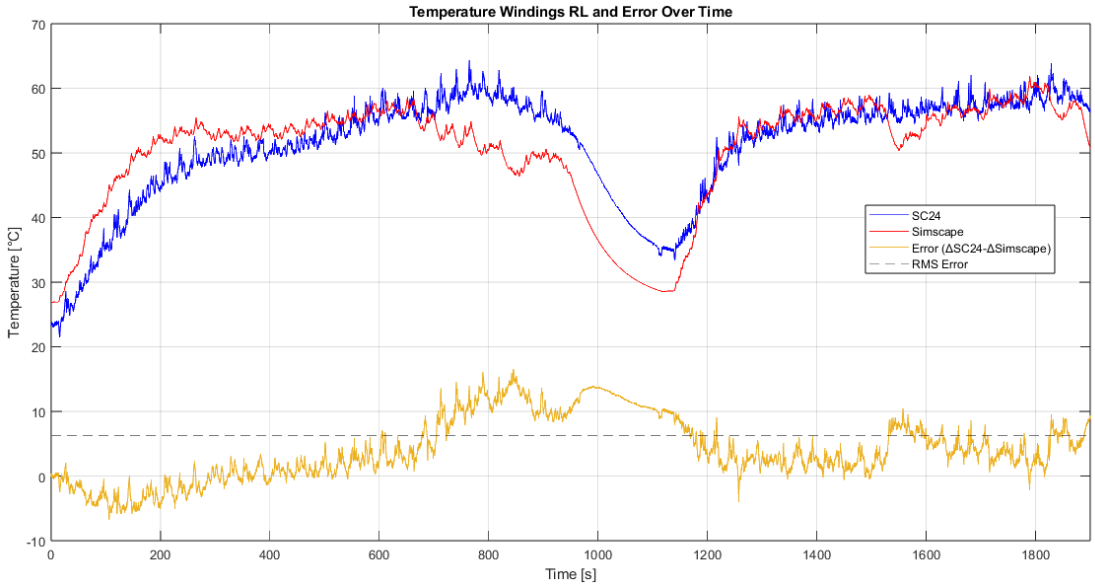

Figure 4.25: Rear left motor temperature during endurance.

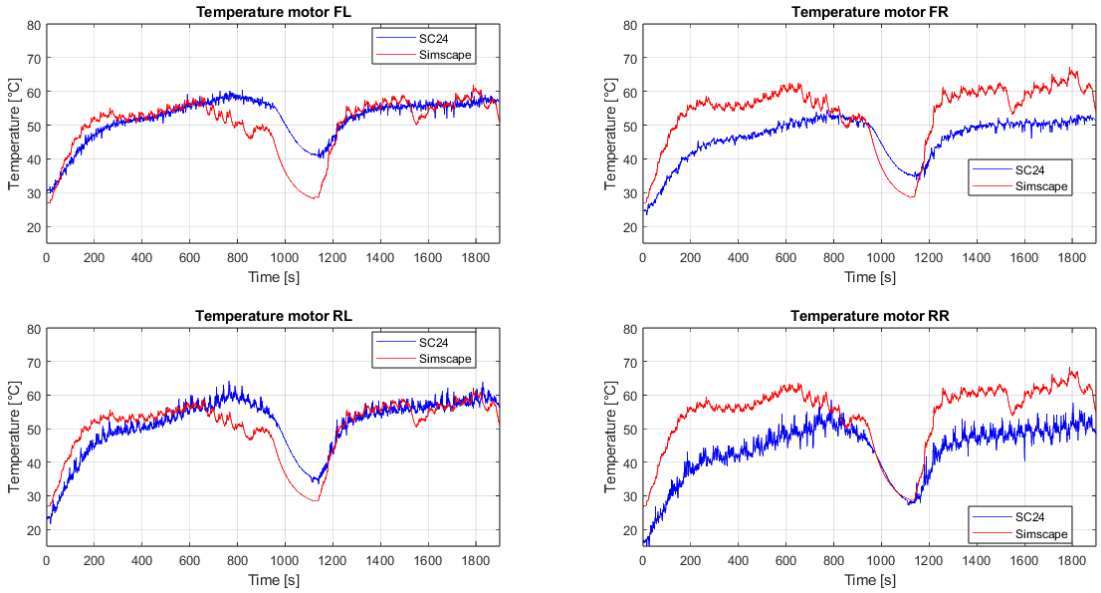

Figure 4.26: Motor temperatures during endurance.

vehicle speed, which affect the calculation of the convective heat transfer coefficient; (ii) an inaccurate estimation of the battery pack's thermal mass; and (iii) an incorrect modeling of the convective cooling behavior.

Despite these differences, the temperature prediction remains within an acceptable margin of error (less than 3 °C at last time instant), indicating that the thermal model is reasonably accurate. However, improvements could be made in future work, particularly by acquiring more experimental data, such as a CFD-derived convective coefficient, to better calibrate the thermal model.

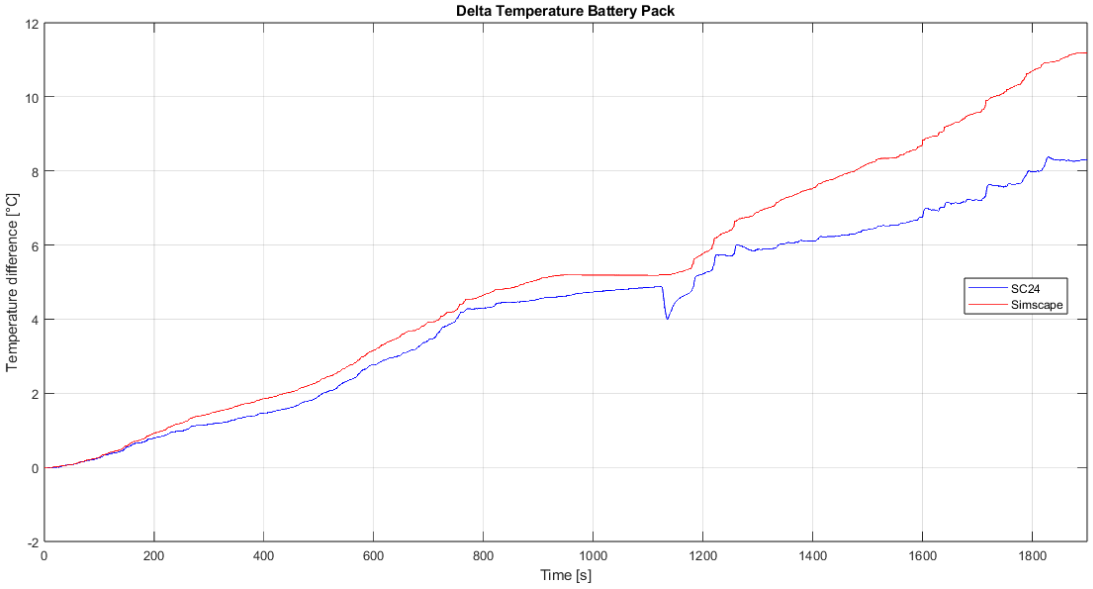

Figure 4.27: Delta temperature battery pack during endurance.

Chapter 5

Conclusions

The work presented throughout this thesis aimed to develop and validate a comprehensive simulation model capable of replicating the real-world behavior of a Formula Student vehicle across multiple subsystems and maneuvers. After an extensive validation process, key insights have been drawn, and several conclusions can now be outlined to assess the reliability, limitations, and potential future developments of the model.

In summary, the vehicle model has been constructed using all available data, from CAD geometries to experimental measurements such as wind tunnel results. Different sources, each with varying levels of accuracy, have been combined to build the most accurate model possible. The validation process ranged from single subsystems, such as suspension and steering, up to full-vehicle endurance simulations.

The results are more than encouraging: suspension and steering behavior perfectly match CAD outputs and other multibody platforms; acceleration and skidpad events show lap time differences below 3%, and the Double Lane Change test is reproduced with high fidelity. The endurance simulation demonstrates high accuracy, with energy consumption deviating by less than 5% and motor temperature exhibiting an RMS error of only 6.23 °C. However, the driver model shows clear limitations in replicating real-world behavior in demanding scenarios such as the autocross event. Similarly, the battery pack cooling model, although within an acceptable error range, does not perfectly align with experimental data.

The simulation tool developed here proves to be extremely valuable during the intermediate stages of vehicle design. It allows for early simulation of endurance runs, assisting in proper battery sizing and thermal management. At the same time, it offers highly accurate performance estimations in events like acceleration and skidpad. This enables engineers to start from a known suspension geometry and correctly dimension not only the suspension itself, but a wide range of mechanical components.

During race preparation, this model becomes a crucial tool for defining race strategy and target pace, without adding kilometers to real car. It allows testing of a large number of scenarios, generating a vast dataset that can provide valuable insights to drivers and race engineers on how to complete an endurance event while minimizing energy consumption and thermal stress on the powertrain, and maximizing competition points.

Regarding future improvements, the model is versatile and offers numerous development opportunities. To become a fully comprehensive tool, it must be capable of simulating both endurance and autocross events at realistic paces, while more accurately replicating real-world driver behavior. Moreover, since one of the goals of this thesis was to establish a foundation for powertrain thermal management, the collection of additional experimental data, particularly on motor and inverter efficiency, as well as battery pack cooling, would allow for significant enhancements in the corresponding subsystems modeling, improving both model validation and predictive accuracy.

It is also worth exploring the addition of compliance in suspension elements and the chassis. This would enable more complete kinematic analysis and allow for the prediction of forces and stresses in suspension components, which could be validated with strain gauge data from the real car and correlated with finite element analysis.

Finally, with the integration of real-time inputs from a steering wheel and pedal set, the model could evolve into a Driver-in-the-Loop (DiL) simulator. It is important to note, however, that the current simulation is not real-time capable. This implies that significant efforts in optimization, and, if necessary, simplification of specific subsystems, would be required to make the model suitable for real-time use by a human driver. Such a development would enable effective driver training and allow for even more accurate insights into energy consumption and power delivery, as the same driver would operate both the simulated and the real vehicle.

Appendix A

Suspension Kinematics Validation Plots

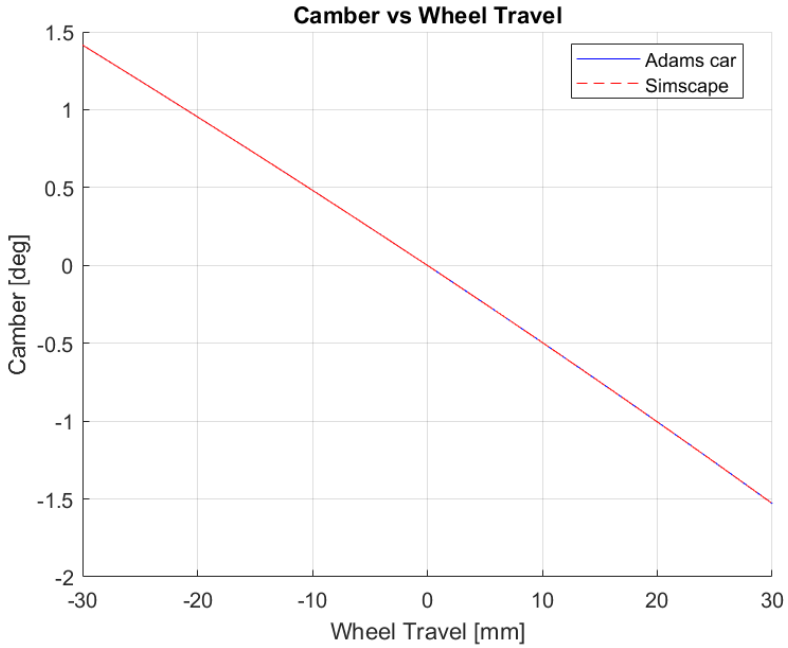

Figure A.1: Validation of camber front suspension.

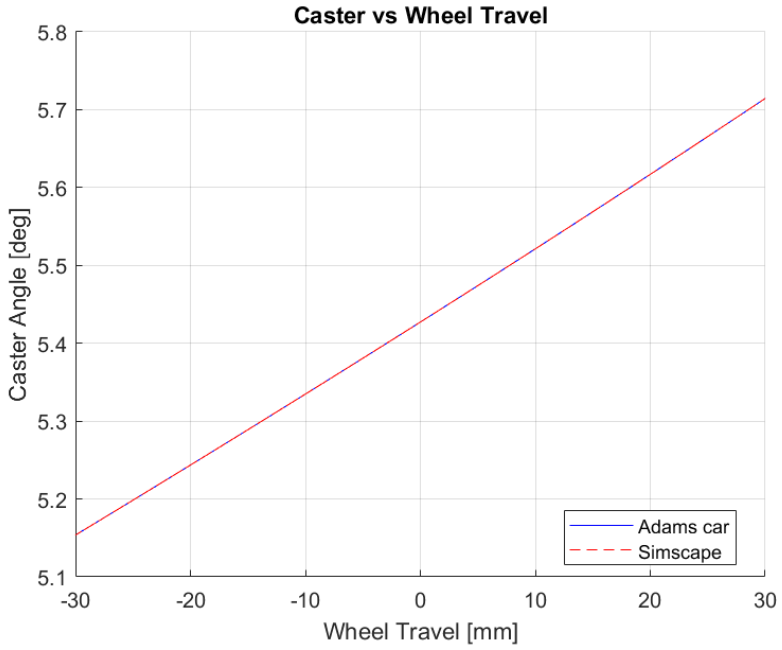

Figure A.2: Validation of caster front suspension.

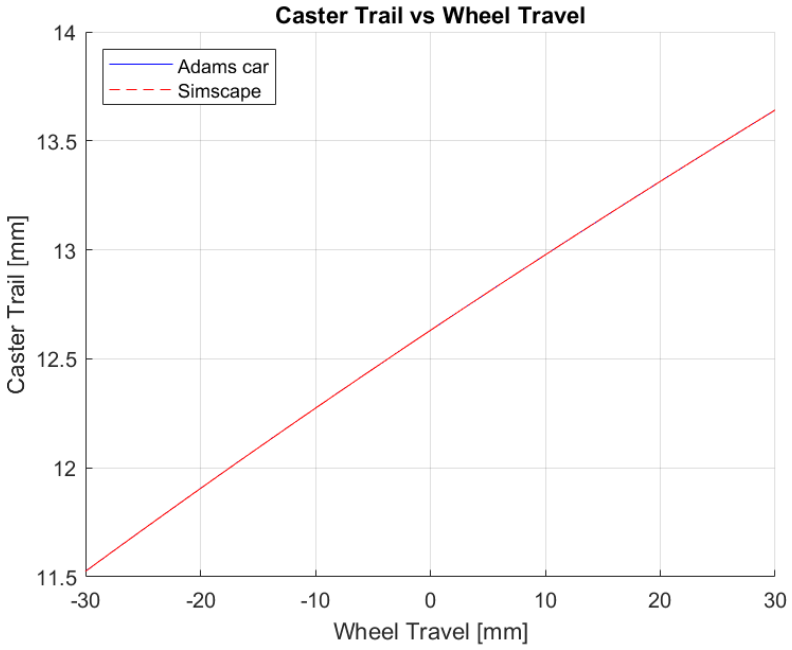

Figure A.3: Validation of caster trail front suspension.

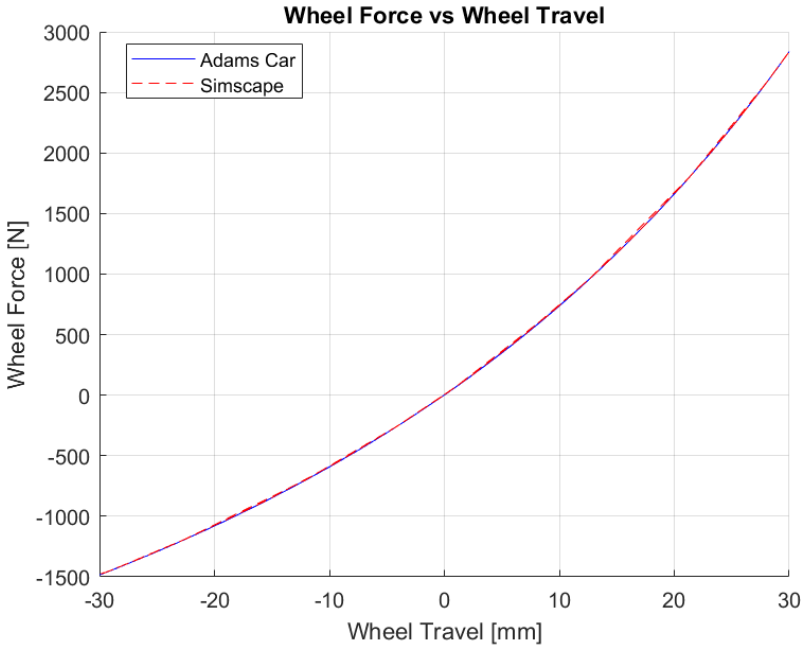

Figure A.4: Validation of force front suspension.

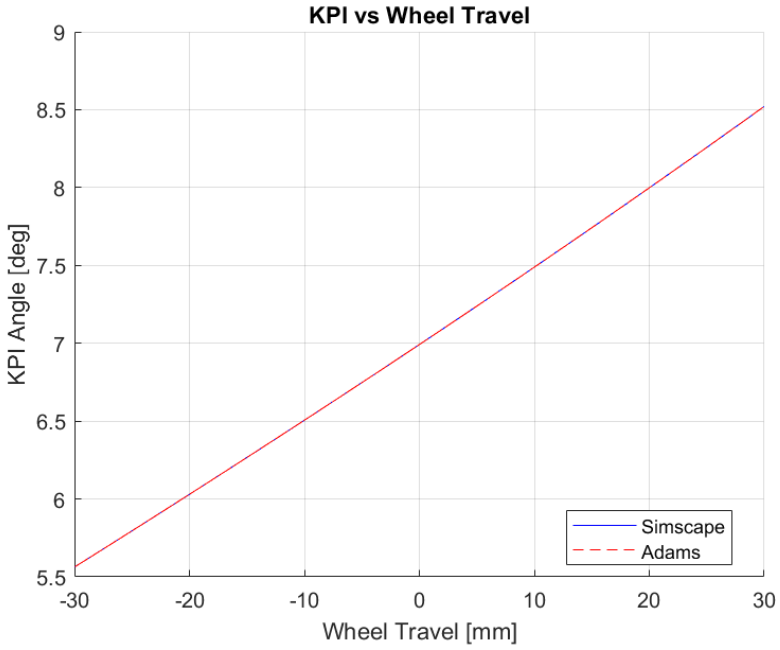

Figure A.5: Validation of KPI front suspension.

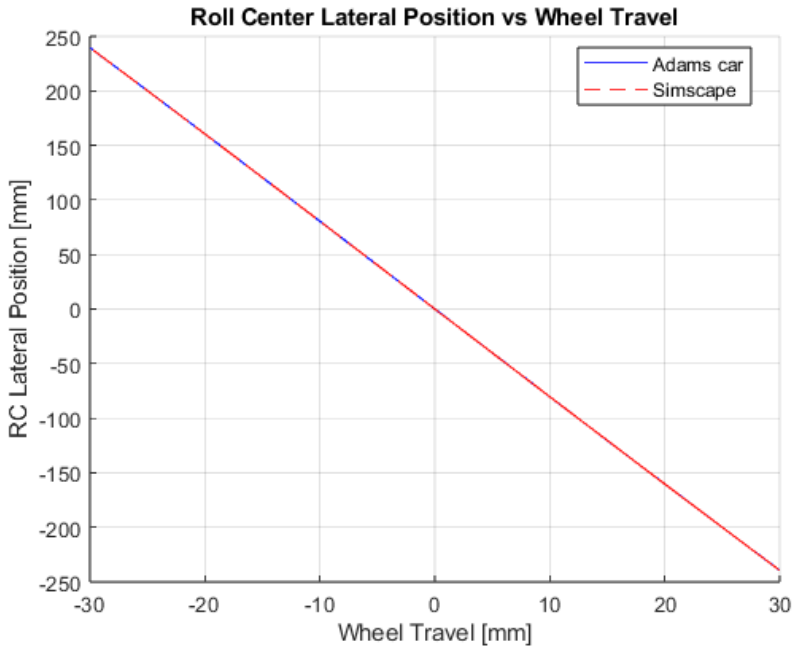

Figure A.6: Validation of lateral roll center front suspension.

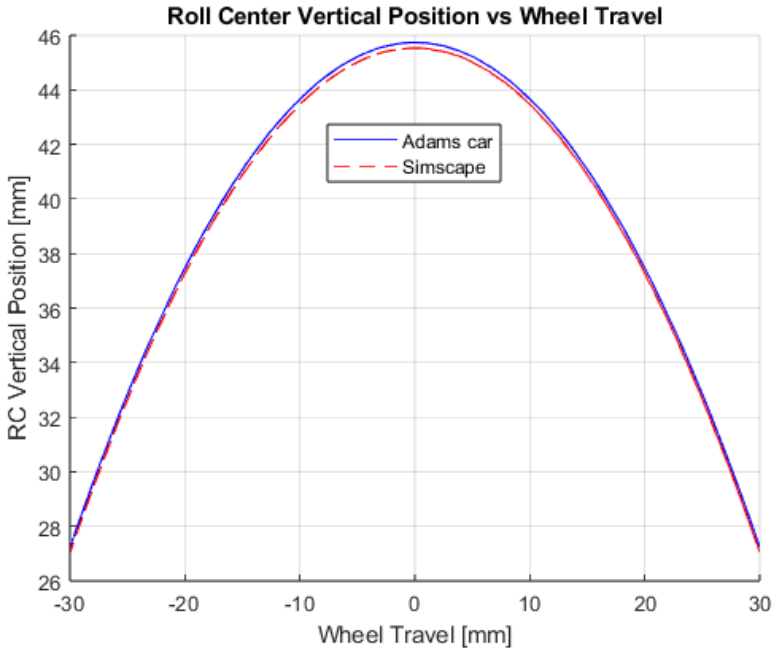

Figure A.7: Validation of vertical roll center front suspension.

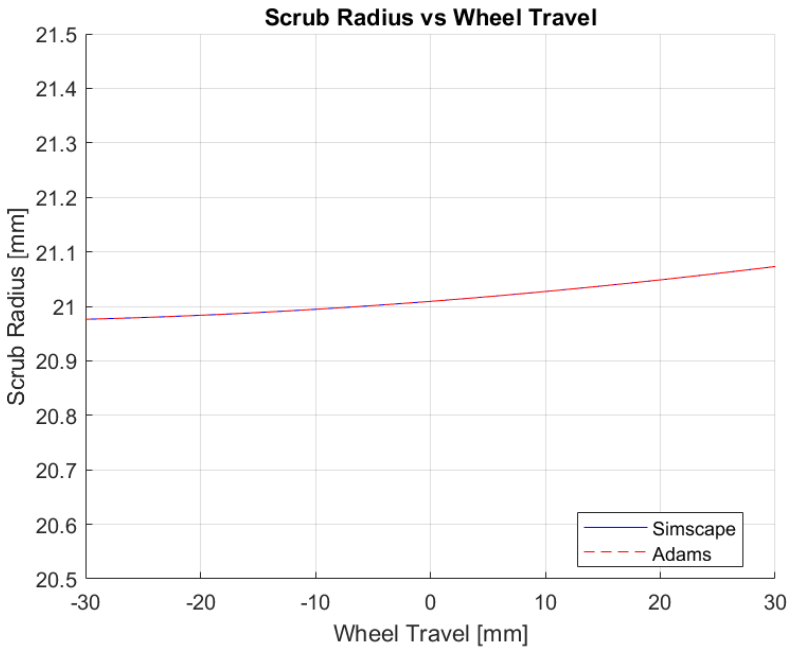

Figure A.8: Validation of scrub radius front suspension.

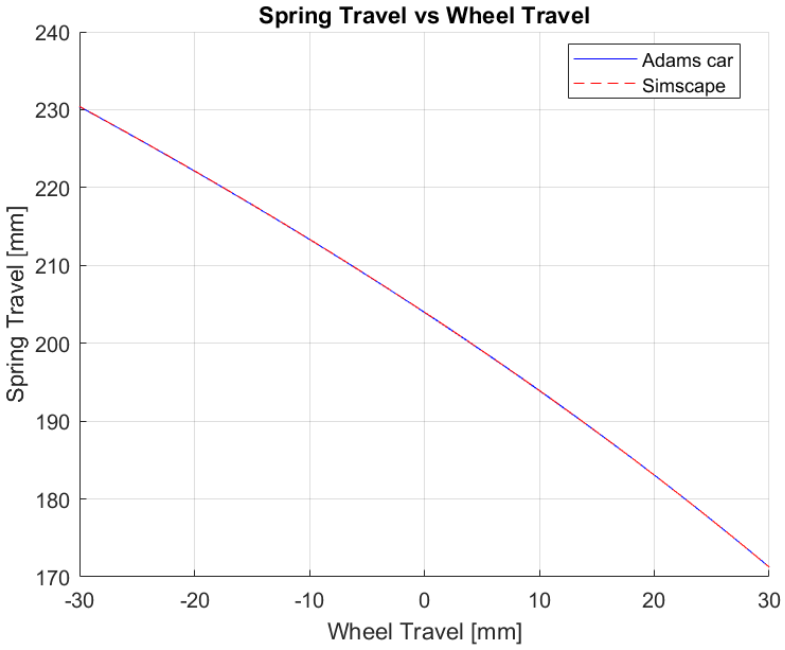

Figure A.9: Validation of spring travel front suspension.

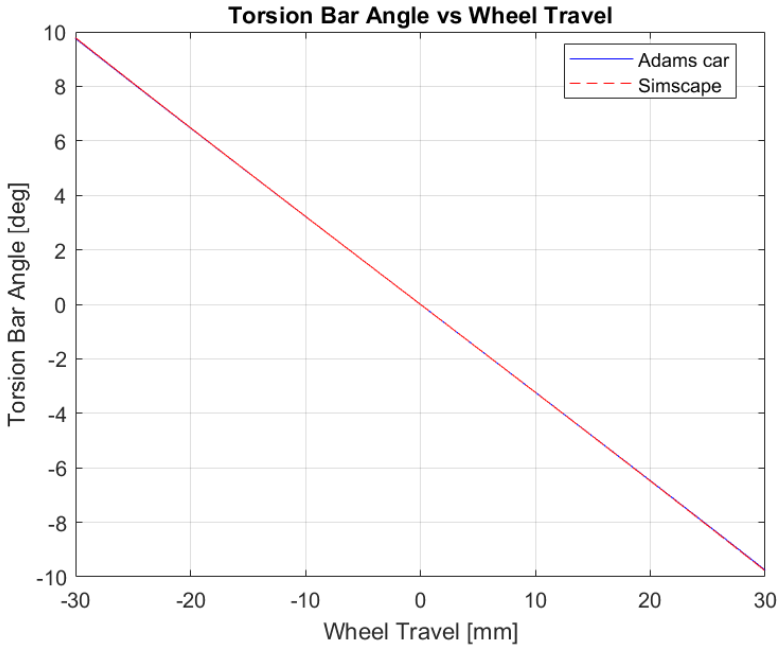

Figure A.10: Validation of T-bar rotation front suspension.

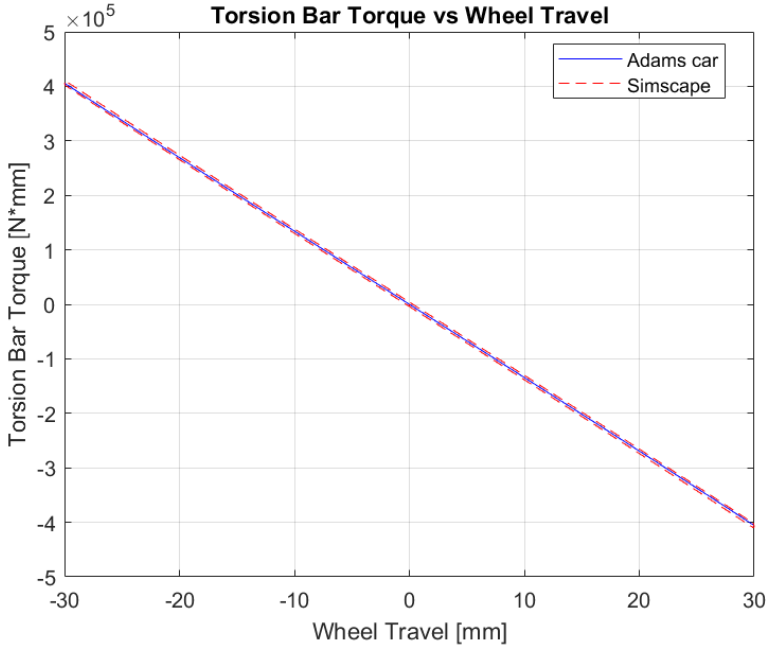

Figure A.11: Validation of T-bar torque front suspension.

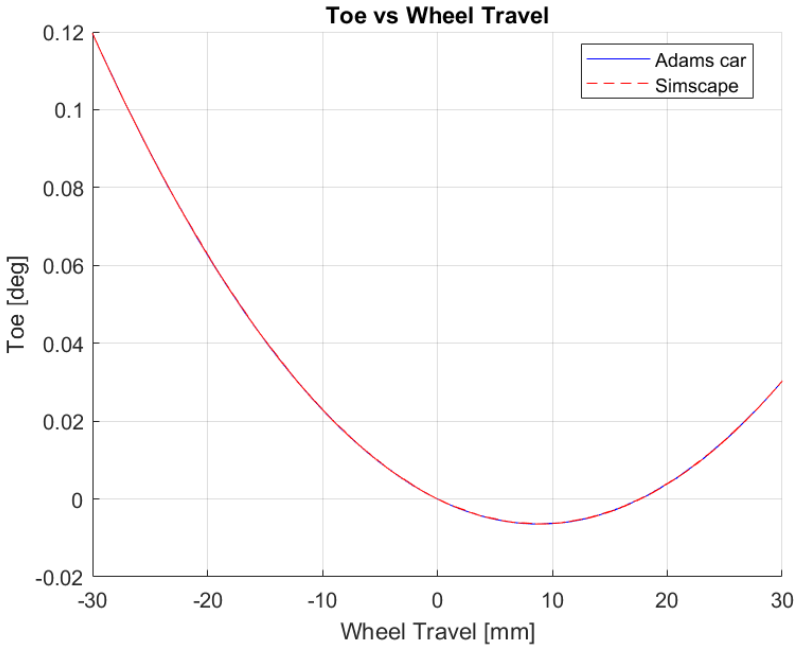

Figure A.12: Validation of toe front suspension.

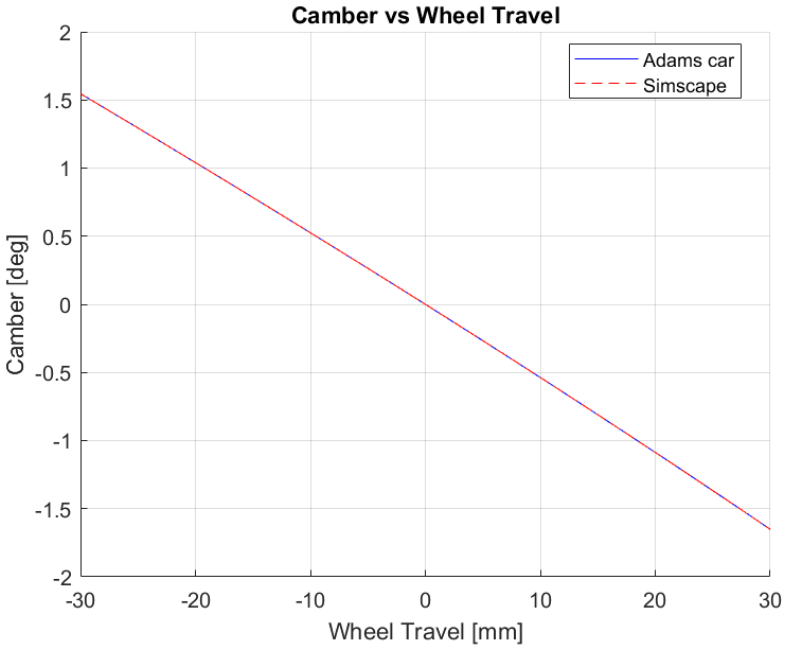

Figure A.13: Validation of camber rear suspension.

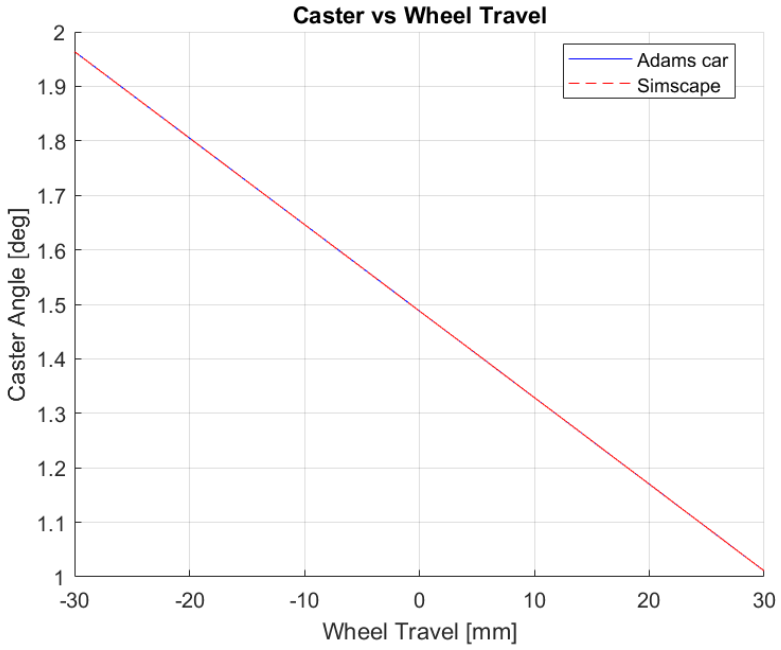

Figure A.14: Validation of caster rear suspension.

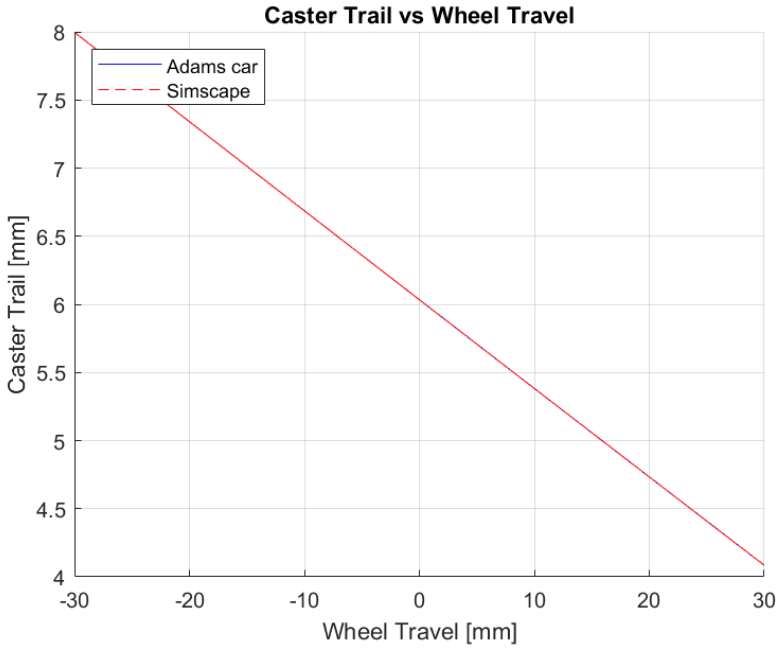

Figure A.15: Validation of caster trail rear suspension.

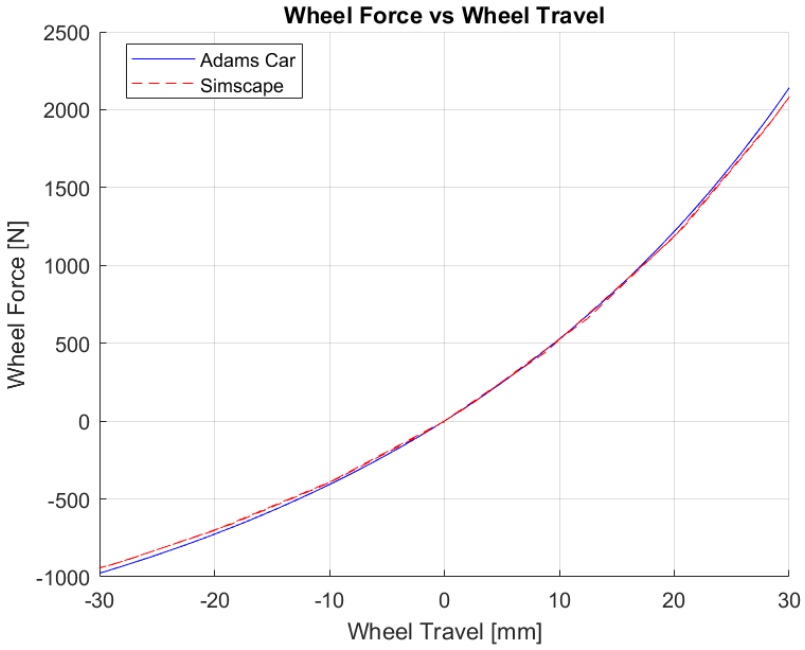

Figure A.16: Validation of force rear suspension.

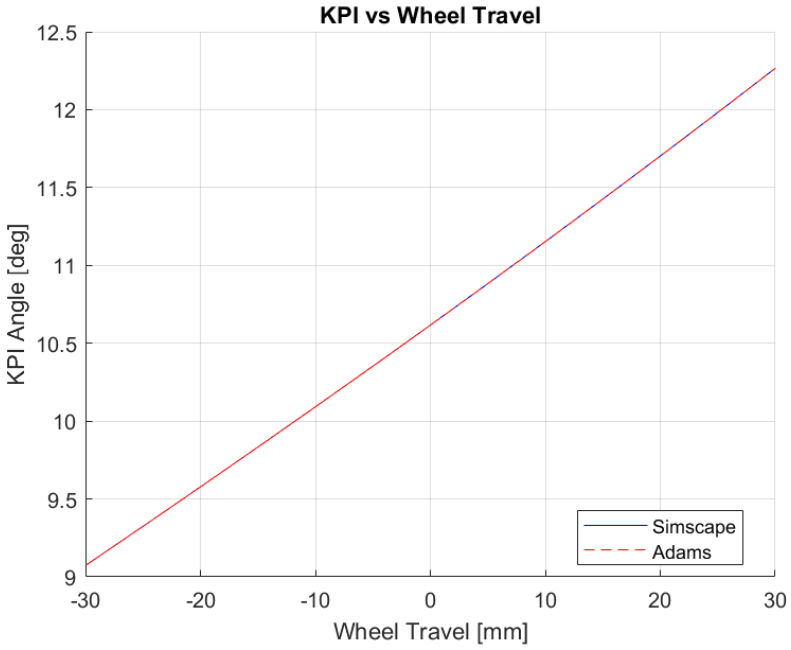

Figure A.17: Validation of KPI rear suspension.

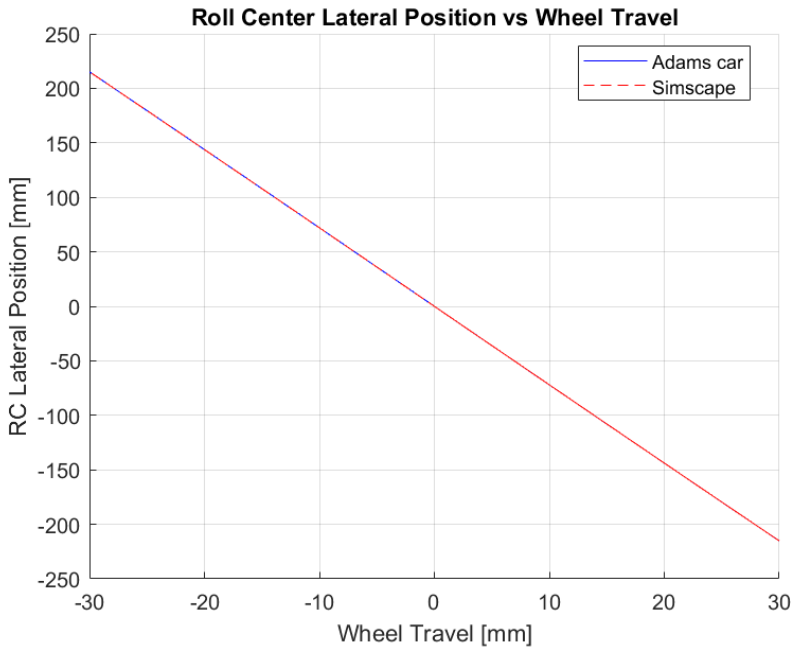

Figure A.18: Validation of lateral roll center rear suspension.

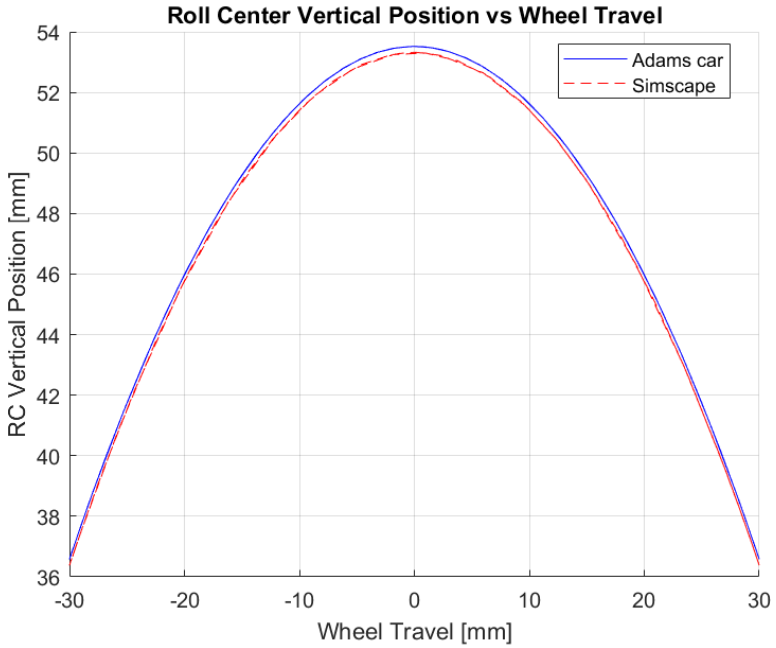

Figure A.19: Validation of vertical roll center rear suspension.

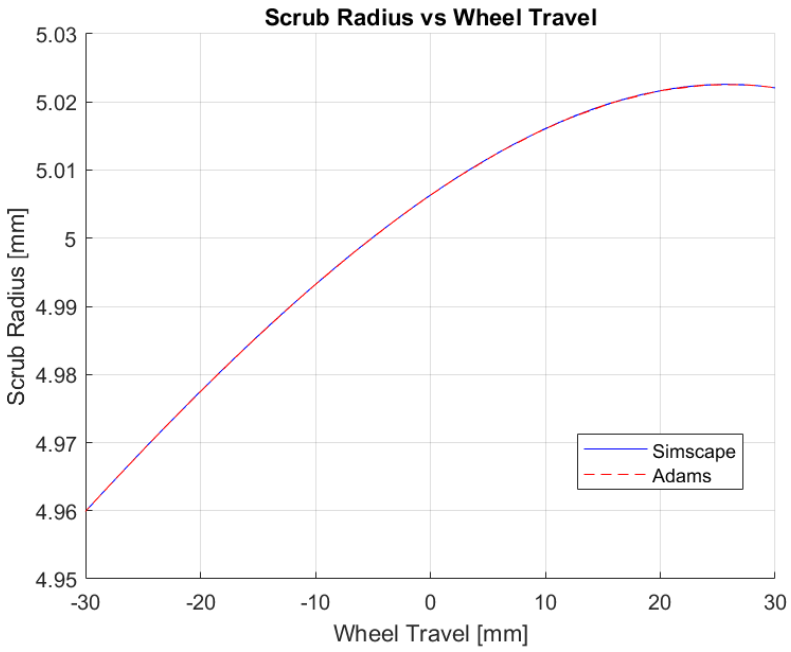

Figure A.20: Validation of scrub radius rear suspension.

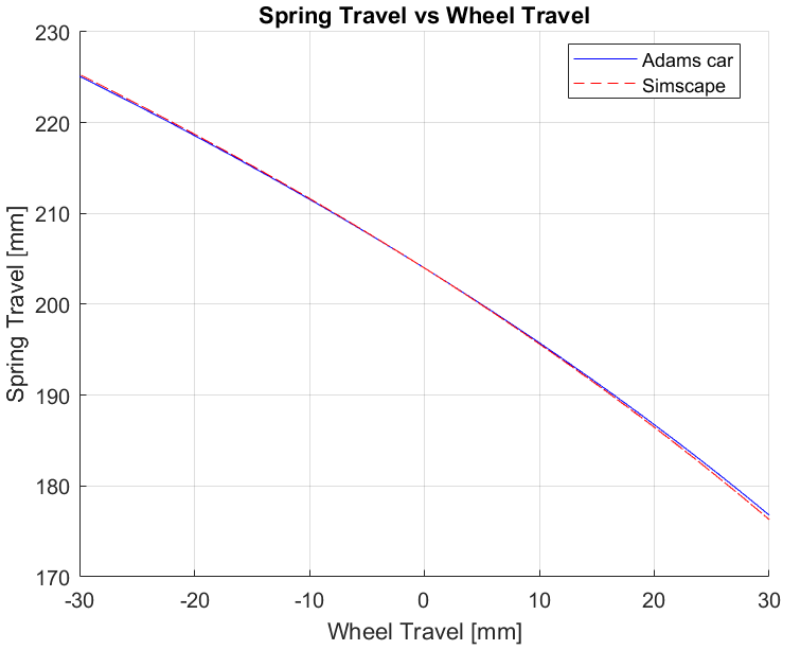

Figure A.21: Validation of spring travel rear suspension.

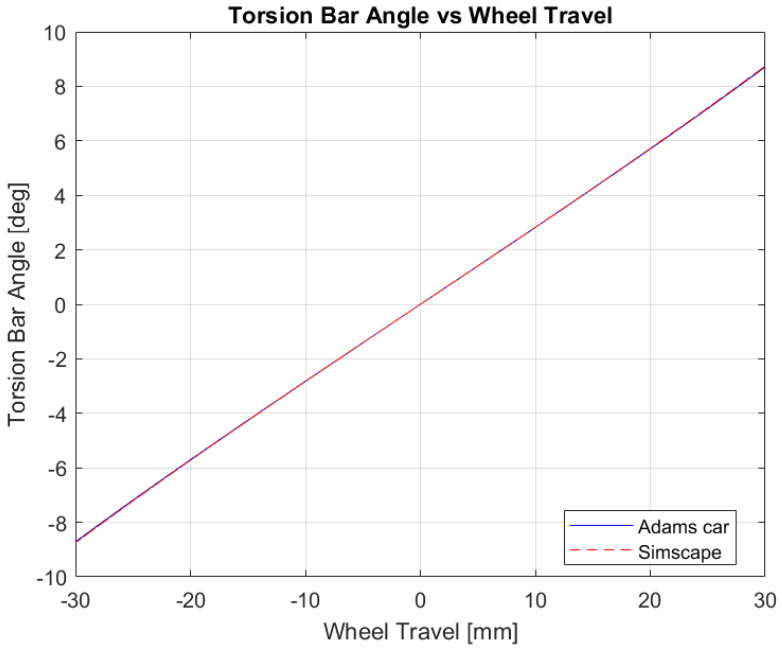

Figure A.22: Validation of T-bar rotation rear suspension.

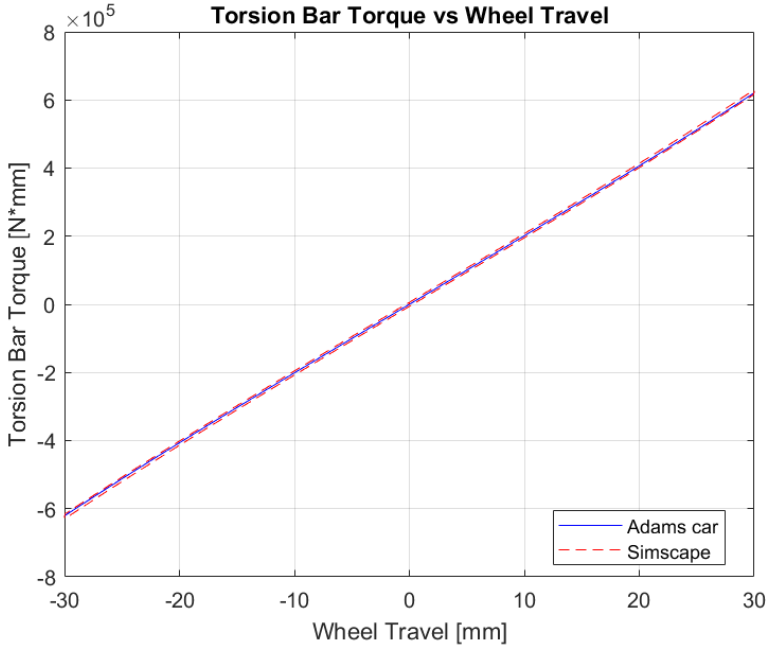

Figure A.23: Validation of T-bar torque rear suspension.

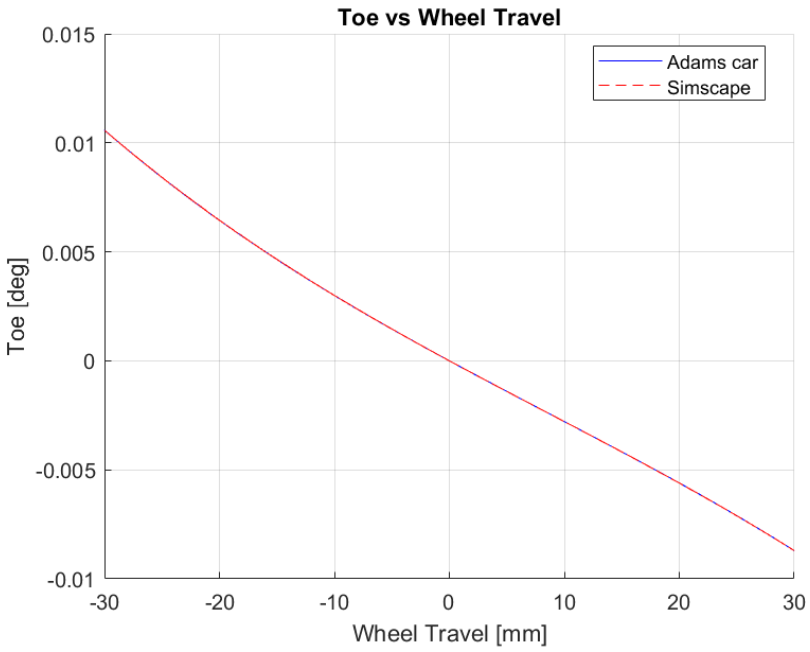

Figure A.24: Validation of toe rear suspension.

Bibliography

[1] Formula Student Germany. *Formula Student Rules 2024*. https://www.formulastudent.de/fileadmin/user_upload/all/2025/rules/FS-Rules_2025_v1.1.pdf. 2023 (cit. on p. 5).

[2] Giancarlo Genta and Lorenzo Morello. *The Automotive Chassis*. Turin: Springer, 2009 (cit. on pp. 9, 11–13, 15).

[3] William F. Milliken and Douglas L. Milliken. *Race Car Vehicle Dynamics*. SAE International, 1995 (cit. on p. 17).

[4] Bruce R. Munson Michael J. Moran Howard N. Shapiro and David P. DeWitt. *Introduction to Thermal Systems Engineering: Thermodynamics, Fluid Mechanics, and Heat Transfer*. New York: John Wiley & Sons, 2003 (cit. on pp. 20, 51).

[5] *URL*. https://it.enmotor.com/what-is-the-difference-between-ipm-and-spm-motor/. Enneng (cit. on p. 25).

[6] Steve Pickering Dave Staton Eddie Chong and Aldo Boglietti. *Cooling of Rotating Electrical Machines*. London: The Institution of Engineering and Technology, 2022 (cit. on pp. 27, 30).

[7] Mathworks. *Longitudinal Driver*. https://it.mathworks.com/help/autoblks/ref/longitudinaldriver.html. 2024 (cit. on p. 36).

[8] Mathworks. *Disc Brake*. https://it.mathworks.com/help/sdl/ref/discbrake.html. 2024 (cit. on p. 37).

[9] Mathworks. *Magic Formula Tire Force and Torque*. https://it.mathworks.com/help/releases/R2024b/sm/ref/magicformulatireforceandtorque.html?searchPort=49961. 2024 (cit. on p. 42).

[10] Mathworks. *Battery (Table-Based)*. https://it.mathworks.com/help/sps/ref/batterytablebased.html. 2024 (cit. on p. 45).

[11] Mathworks. *Motor & Drive*. https://it.mathworks.com/help/sps/ref/motordrivesystemlevel.html. 2024 (cit. on p. 46).

[12] Giovanni Principato Trosso. «Analisi e confronto prestazionale tra un inverter custom ed uno commerciale per la Formula SAE Electric.» MA thesis. Turin: Politecnico di Torino, 2020 (cit. on p. 48).

[13] Daniel Carlino. «Suspension Kinematics Design and Simulation for a Formula Student Race Car.» MA thesis. Turin: Politecnico di Torino, 2022 (cit. on p. 54).

[14] *DD5-14-10-POW (AMK motor datasheet)*. `https://www.amk-motion.com/amk-dokucd/dokucd/en/content/resources/pdf-dateien/fse/motor_data_sheet_a2370dd_dd5.pdf`. Kirchheim, Germany: AMK (cit. on p. 56).